Superadiabatic Forces in the Dynamics of the Hard Sphere Fluid

Von der Universität Bayreuth zur Erlangung des Grades eines Doktors der Naturwissenschaften (Dr. rer. nat.) genehmigte Abhandlung

von

Lucas L. Treffenstädt

aus Frankfurt am Main

1. Gutachter: Prof. Dr. Matthias Schmidt
2. Gutachter: Prof. Dr. Matthias Fuchs

Tag der Einreichung: 22.03.2022
Tag des Kolloquiums: 08.07.2022

Zusammenfassung

In dieser Dissertation wird die Brown'sche Dynamik von monodispersen harten Kugeln untersucht. Harte Kugeln bilden eine sehr einfache Modellflüssigkeit, bei der die Paarwechselwirkung lediglich einen Überlapp der Kugeln verhindert. Das Paarpotential der Kugeln ist daher durch den Kugeldurchmesser vollständig charakterisiert. Trotz dieser scheinbaren Einfachheit hat diese Flüssigkeit interessante Eigenschaften und bietet die Möglichkeit, fundamentale Eigenschaften der flüssigen Phase zu untersuchen.

Die Brown'sche Dynamik ist ein Modell zur Beschreibung der Bewegung von kolloidalen Partikeln, hier Kugeln, in einem flüssigen Medium. Die mikroskopischen Interaktionen der Kugeln mit dem Medium werden dabei als externe Zufallskräfte modelliert; das Medium selbst wird nicht modelliert. Zudem wird die Trägheit der Kugeln vernachlässigt. Die resultierende stochastische Bewegungsgleichung für das Vielteilchensystem kann numerisch integriert werden und liefert so eine leistungsfähige Simulationsmethode. Im speziellen Fall harter Kugeln müssen Kollisionen der Kugeln gesondert behandelt werden. Eine Möglichkeit dieser Behandlung ist ereignisgetriebene Brown'sche Dynamik (event-driven Brownian dynamics), welche hier als Ausgangspunkt einer Studie der Dynamik harter Kugeln verwendet wird.

Von zentralem Interesse ist die statistischen Beschreibung eines thermodynamischen Systems im Einteilchenbild, in dem gemittelte Größen wie die Teilchendichte und der Teilchenstrom betrachtet werden, die aus Teilchenpositionen und -geschwindigkeiten im Vielteilchenbild durch Mittelung bestimmt werden können, wobei noch die Abhängigkeit von einer (dreidimensionalen) Ortskoordinate und der Zeit bleibt. Da die Simulation der Vielteilchendynamik, gerade bei sehr großen und/oder dichten Systemen, erheblichen Rechenaufwand bedeutet, ist eine direkte Beschreibung der Dynamik von Einteilchengrößen wünschenswert. Darüber hinaus ermöglicht die Beschreibung im Einteilchenbild Verständnis von kollektiven Phänomenen, die in der Vielteilchenbeschreibung verborgen bleiben. Eine Möglichkeit einer solchen Einteilchenbeschreibung liefert die Powerfunktionaltheorie. Diese Methode ermöglicht eine formal exakte Beschreibung der klassischen (und Quanten-) Dynamik von Nichtgleichgewichtssystemen. Im Rahmen dieser Theorie können die internen Kräfte des Systems in adiabatische und superadiabatische Kräfte zerlegt werden. Die adiabatischen Kräfte sind dabei diejenigen, die ausschließlich vom momentanen Dichteprofil des Systems abhängen. Sie können aus dem Freie-Energie-Funktional der klassischen Dichtefunktionaltheorie

abgeleitet werden. Superadiabatische Kräfte sind dagegen echte Nichtgleichgewichtskräfte und hängen von Dichte- und Stromprofil im Lauf der Zeit ab. Dieses *Gedächtnis* kann zudem räumlich nichtlokal sein.

Das Ziel dieser Dissertation ist die Entwicklung eines universalen Funktionales zur Berechnung von superadiabatischen Kräften in der Dynamik von harten Kugeln. Die Entwicklung dieses Funktional geschieht anhand von Simulationen einer inhomogen gescherten Hartkugelflüssigkeit [1] sowie der Zeitentwicklung der van Hove-Funktion einer homogenen Flüssigkeit harter Kugeln im Gleichgewicht [2, 3]. Die van Hove-Funktion $G(r, t)$ gibt die Korrelation zwischen einem Teilchen am Ursprung zur Zeit 0 und einem Teilchen mit Abstand r zum Ursprung zur Zeit t. Durch den dynamischen Testteilchenlimes kann diese Funktion auf die Zeitentwicklung einer binären Flüssigkeit abgebildet werden, die mit einem speziellen Anfangszustand präpariert wird. In diesem Anfangszustand entspricht die Dichte der ersten Flüssigkeitskomponente, der *Selbstkomponente*, der eines einzelnen Teilchens, welches im Ursprung des Systems fixiert ist. Die zweite Komponente, die *Distinktkomponente*, ist entsprechend der radialen Verteilungsfunktion im Gleichgewicht verteilt.

Superadiabatische Kräfte spielen sowohl in der gescherten Flüssigkeit als auch im Testteilchenlimes eine wichtige Rolle. Die vorgeschlagene Approximation beschreibt diese Kräfte mit hoher Genauigkeit. Die Konstruktion dieser Approximation erlaubt die Zerlegung der superadiabatischen Kräfte in mehrere unterschiedliche Beiträge. Dies sind im Einzelnen eine viskoelastische Kraft, eine Reibungskraft, und eine strukturbildende Kraft. Die Studie der gescherten Flüssigkeit zeigt, dass die viskoelastische Kraft unter Berücksichtigung nichtlokaler Gedächtniseffekte beschrieben werden muss, um eine Approximation mit hoher Genauigkeit zu erreichen. Die Studien der van Hove-Funktion führen zu der Erkenntnis, dass die Approximation, die zunächst für Nichtgleichgewichtssysteme entwickelt wurde, auch die Gleichgewichtsdynamik gut beschreibt. Dies erlaubt den Schluss, dass es sich bei den beschriebenen Kräften um universelle Effekte in Flüssigkeiten handelt.

Abstract

In this thesis we investigate the Brownian dynamics of the monodisperse hard sphere fluid. The hard sphere fluid is a very simple model fluid, in which the interparticle interactions prevent particle overlap. The pair potential of the spheres is therefore characterised entirely by the diameter of the spheres. Despite its simplicity, the hard sphere fluid has many interesting properties and provides opportunities to study many fundamental properties of the fluid state.

Brownian dynamics is a model for the time evolution of colloidal particles suspended in a solvent. The microscopic interactions between particles and solvent are modelled via stochastic external forces. The solvent itself is not modelled, and inertia of the particles is neglected. This results in a stochastic equation of motion for the many-body system, which can be integrated in time to obtain a powerful simulation method. For hard sphere interactions, special care must be given to particle collisions. One possible method is event-driven Brownian dynamics. We use event-driven Brownian dynamics simulations as a reference for a study of hard sphere dynamics.

We are interested in a statistical description of a thermodynamic system in the one-body picture, where we consider one-body correlation functions such as the particle density profile and particle current profile. These quantities can be obtained via averages of many-body observables like particle positions and velocities. A one-body description is desirable, as the computational cost of many-body simulations can be prohibitive for large and/or dense systems. Additionally, a one-body description enables the understanding of collective phenomena which may be hidden in the many-body picture. One such description is given by power functional theory, which is a formally exact theoretical framework for one-body dynamics of classical (and quantum) nonequilibrium systems. This framework allows for a splitting of the internal force density, which acts on the current profile into an adiabatic and a superadiabatic contribution. Adiabatic forces depend on the instantaneous density profile of the system and can be derived from the free energy functional known from classical density functional theory. Superadiabatic forces are true nonequilibrium forces and depend on density and current as a function of time. This memory of previous density and current can be spatially nonlocal.

One central aim of this thesis is to establish a universal functional for the calculation

of superadiabatic forces in the dynamics of the hard sphere fluid. The development of this functional is based on simulations of an inhomogeneously sheared hard sphere fluid [1], and of the time evolution of the van Hove function [2, 3]. The van Hove correlation function $G(r, t)$ gives the correlation of a particle at the origin at time 0 with particles at distance r from the origin at time t. This function is related via the dynamical test particle limit to the time evolution of a binary fluid with a special initial condition. In this initial condition, the density of one fluid component, the *self component*, corresponds to a single particle fixed at the origin. The other component, the *distinct component*, is distributed according to the equilibrium radial distribution function.

We find that superadiabatic forces play a major role both in sheared fluids and in the test particle limit and we propose an approximation which accurately describes these forces. The bottom-up construction of this approximation allows for a splitting of the superadiabatic force field into several distinct forces. These are the viscoelastic force, the drag force, and the structural force. In our study of the sheared fluid, we show that an accurate description of the viscoelastic force requires nonlocal memory. We demonstrate the quantitative accuracy of our corresponding approximation of this force by comparing with simulation data. In our studies of the van Hove function we arrive at the insight that our power functional approximation, which was first developed for the description of nonequilibrium systems, is equally applicable for equilibrium dynamics. We conclude that the described forces represent universal effects in fluids.

Contents

1. Introduction

In this thesis, we try to further the understanding of liquids by studying hard spheres, one of the prototypical model fluids [4]. A liquid consists of many particles, which are unordered and close together, such that they interact strongly. This poses a problem for us as theorists: how can we reduce the many degrees of freedom in such a system – in order to find a simpler mathematical description – without loosing all the information that is needed to represent the interactions between particles accurately?

A first step is to abstract away those interactions which we deem irrelevant to the problem at hand. If we examine a collection of particles suspended in a solvent – e.g. colloidal particles – the behaviour of every molecule making up the solvent itself does not have to be described in detail, given that the suspended particles are much larger than the solvent molecules. Instead, we model the interactions between solvent and suspended particles as a series of random jolts. If the statistical properties of these random jolts are sufficiently close to those of the real solvent, we have successfully simplified our description – and obtained the model of Brownian motion [5].

We still have all the degrees of freedom of the suspended particles themselves, though. Again, a statistical description can reduce the amount of information needed to capture the overall behaviour of the system. Instead of the positions of many particles, we can examine the density profile – a scalar field that gives the average number of particles per volume at each position in space. A density profile with sufficient spatial resolution contains the information where particles are strongly packed, and where they are more dilute, on a microscopic scale. Using particle-based computer simulations, the density profile of a system can be calculated via averaging. However, there are also methods which determine the density profile of a liquid in equilibrium directly, given only the interparticle potential of the suspended particles, and an external potential. One such method is classical density functional theory (DFT). Figure 1.1 shows a rather early example of a comparison between density profiles resulting from Monte Carlo simulation and theoretical results using DFT. We see there not only that

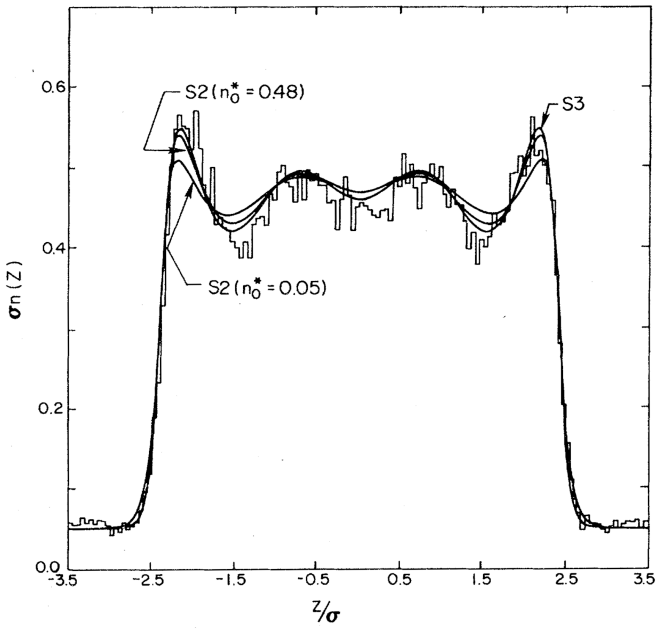

Figure 1.1.: Early result for the density profile of a Lennard-Jones liquid trapped in a potential well, calculated with classical density functional theory using different approximations (strong lines) and Monte Carlo simulation (thin lines) by Ebner, Lee and Saam [6]. Notably, the simulation results are quite noisy even at a much coarser resolution than the respective DFT results, due to the computational constraints of the day.

DFT can produce results which are quite close to particle simulations, but also that computational constraints can severely limit the amount and quality of information accessible via simulation.

Out of equilibrium (e.g. if the system is exposed to a shear force), things become a good deal more complicated, since the time evolution of a density profile depends not only on the instantaneous external potential, but also on how the system behaved previous to this point in time. By switching from a many-body description (particle positions) to a one-body description (the density profile), we have turned a system whose current behaviour does not depend on previous behaviour, into one whose does [5]. However, using dynamic density functional theory or power functional theory, we can also describe the time evolution of the density profile.

The density profile is a one-body correlation function, meaning it tells us where any particle might be in space. However, it does not tell us where particles are in relation

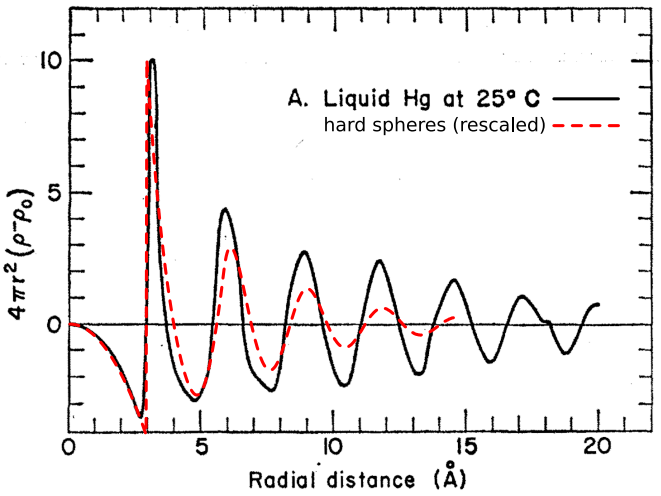

Figure 1.2.: Classic result for the radial distribution function, multiplied by r^2, of liquid mercury at 25 °C (black solid line), by Kaplow et al. [7]. The distribution is qualitatively quite similar to that of the hard sphere liquid at volume fraction $\eta = 0.38$ (red dashed line). The data for the hard sphere radial distribution function has been rescaled to allow a qualitative comparison.

to each other, and we loose information about the microscopic dynamics that are present even if the liquid is at equilibrium and the density profile does not change. For that, we need to examine two-body correlations, for example the radial distribution function. This function tells us, given a particle at a certain position, where other particles are dense or dilute in relation to that first particle. Figure 1.2 shows, as an example, the radial distribution function of liquid mercury. The radial distribution function only considers these correlations at one point in time, and thus also does not capture dynamics. If, instead, we calculate the correlations between one particle now, at a fixed point in space, with other particles at a later time, we obtain the van Hove function. Using the dynamic test particle limit, it is possible to use DDFT or PFT to calculate the van Hove function.

This thesis is organised as follows: Chapter 1 gives an overview of the theoretical concepts used in the thesis, as well as a bit of context with other research. We cover the importance of the hard sphere model in section 1.1, and present simulation methods in sections 1.2 and 1.3. The relevant one- and two-body correlation functions are presented in section 1.4 and section 1.5, respectively. In section 1.6, briefly introduce the concept of shear as one of the prototypical out-of-equilibrium situations for a liquid.

Sections 1.7, 1.8 and 1.9 give an overview of DFT, DDFT and PFT, in this order. Finally, section 1.10 shows the application of DDFT and PFT in the dynamic test particle limit. In our publications [1–3], summarised in chapter 2, we present a a set of superadiabatic functionals which approximate viscoelastic, structural, and drag forces in the hard sphere liquid (see section 2.1). We examine the dynamics of the hard sphere liquid, both in non-equilibrium under the influence of an external force (section 2.2), as well as in equilibrium, where we examine the dynamics of the van Hove function (section 2.3). Even though these situations might seem very different, we show that the forces acting in both cases are captured by the same description. We summarise our findings and suggest possible future directions of research in chapter 3.

1.1. Hard spheres as a model system

The hard sphere system is arguably the simplest model for liquids [4]. The hard sphere pair interaction potential $\phi(r)$ as given by

$$\beta\phi(r) = \begin{cases} 0 & \text{for } r > \sigma \\ \infty & \text{for } r \leq \sigma, \end{cases} \tag{1.1}$$

where β is the inverse temperature $1/\mathrm{k_B}T$ (with absolute temperature T and Boltzmann's constant $\mathrm{k_B}$), depends only on the sphere diameter σ. The infinite interparticle interaction potential for $r \leq \sigma$ means that overlap between spheres is physically forbidden.

This apparently simple model, which neglects many aspects of real molecular interactions, exhibits nevertheless a rich phenomenology that is everything but simple. Understanding these phenomena requires a substantial theoretical apparatus[1].

Perhaps surprisingly, the static and dynamic properties of the hard sphere model are universal for a wide range of liquid systems [4, 8]. To give some examples: Calculation due to Smith and Alder demonstrated that the hard sphere interaction potential is a good basis for a perturbation approach to describe different gases [9]. The equation of state of liquid metals, as well as some other properties, were successfully calculated with a hard-sphere model [10, 11]. Colloidal dispersions, e.g. of silica spheres, are very well described by a hard sphere model [12].

[1] As Robert Evans put it in a workshop on density functional theory, referring to the well-known book by Hansen and McDonald [4]: „It's theory of *simple liquids*, not *simple theory* of liquids".

It comes as no surprise that a great deal of work has gone into understanding the hard sphere model in depth. Kirkwood developed statistical methods for the description of dense fluids with a hard sphere model [13]. An approximate equation of state was proposed by Percus and Yewick [14] and improved by Carnahan and Starling [15]. Classical density functional theory (DFT) [16, 17], which we will cover in more detail below (section 1.7), has proven to be an excellent tool for the study of hard spheres in equilibrium [18, 19]. As early as 1976, Percus derived the exact Euler-Lagrange equation for the equilibrium density profile of hard rods in one dimension [20], which was later re-formulated as a variational principle by Robledo and Varea [21]. About a decade later, Rosenfeld presented a first version of fundamental measure theory [18], which is based, similar to Percus' previous result, on the idea of expressing the free energy functional as a function of weighted densities, which are linked to the geometric measures (volume, surface, mean radius of curvature and Euler-Poincaré characteristic) of the sphere. His approach was later refined in his joint work with Schmidt, Löwen and Tarazona to describe the freezing transition of the hard sphere liquid [22]. There followed further developments by Tarazona [23] and Roth and coworkers [24], resulting in free energy functionals which are accurate up to very high densities. Progress is being made towards achieving a similar degree of accuracy in describing the nonequilibrium behaviour. Dynamic density functional theory (DDFT) [17, 25–27] was developed as a phenomenological extension of DFT to nonequilibrium systems. Power functional theory (PFT) is the formally exact treatment of the nonequilibrium dynamics of fluids [28] on the one-body level. The process of finding suitable descriptions of forces in different model systems in PFT is ongoing. Schmidt and Brader proposed some simple approximation for fluids with pairwise interactions in their presentation of PFT [28]. Bernreuther and Schmidt demonstrated in 2016 for a system of one-dimensional Gaussian core particles that superadiabatic forces, which are neglected in DDFT, can be qualitatively distinct from adiabatic forces [29]. In 2018, de las Heras and Schmidt showed a superadiabatic functional for viscoelastic forces in Brownian dynamics [30]. The same year, Stuhlmüller et al. found a superadiabatic functional describing structural forces, which cause inhomogeneities in driven Brownian fluids orthogonal to the direction of the driving [31]. A systematic description of structural superadiabatic forces was published by de las Heras and Schmidt [32]. Krinninger and Schmidt presented PFT for active Brownian particles [33], work which was promptly used by Hermann et al. to investigate motility induced phase separation in active particles [34–36]. Recently, Geigenfeind et al. presented an approximation for superadiabatic forces in a driven

binary fluid [37].

1.2. Simulation of the Brownian dynamics of hard spheres

Brownian Dynamics describe the motion of particles suspended in a solvent. However, the solvent itself is not described explicitly. Instead, interactions between the solvent molecules and the suspended particles are modelled via random displacements due to a white noise term $\mathbf{R}_i(t)$, where i is the particle index and t is time. The white noise is delta-correlated

$$\left\langle \mathbf{R}_i(t)\mathbf{R}_j(t')\right\rangle = \delta(t-t')\delta_{ij}\mathbb{1}, \tag{1.2}$$

where $\delta(\cdot)$ is the Dirac distribution, δ_{ij} is the Kronecker delta, $\mathbb{1}$ is the 3×3 unit matrix, and $\langle\cdot\rangle$ is an average over many realisations of $\mathbf{R}_i(t)$. Additionally, the mean

$$\langle \mathbf{R}_i(t)\rangle = 0 \tag{1.3}$$

vanishes under the same average. The microscopic equation of motion for the position $\mathbf{r}_i$ of the i-th particle out of a set of N particles is the Langevin equation [4]

$$\gamma\dot{\mathbf{r}}_i(t) \equiv \gamma\frac{\partial \mathbf{r}_i(t)}{\partial t} = \mathbf{f}_i^{\text{int}}(\mathbf{r}^N) + \mathbf{f}^{\text{ext}}(\mathbf{r}_i,t) + \sqrt{2\gamma k_B T}\mathbf{R}_i(t), \tag{1.4}$$

where γ is the friction coefficient of the particles with the implicit solvent, $\mathbf{f}_i^{\text{int}}(\mathbf{r}^N)$ is the internal force, which depends on the positions of all particles $\mathbf{r}^N = \{\mathbf{r}_1,\mathbf{r}_2,\ldots,\mathbf{r}_N\}$, and $\mathbf{f}^{\text{ext}}$ is the external force field. The friction coefficient γ is related to the diffusion coefficient $D = k_B T/\gamma$. Together with the particle diameter σ, the diffusion coefficient can be used to define the Brownian timescale $\tau = \sigma^2/D$. The internal force on particle i is calculated via the gradient of the total interparticle interaction potential with respect to $\mathbf{r}_i$

$$\mathbf{f}_i^{\text{int}}(\mathbf{r}^N) = -\nabla_i u\left(\mathbf{r}^N\right) = -\nabla_i \sum_{k=1}^{N}\sum_{j=k+1}^{N}\phi(\mathbf{r}_k-\mathbf{r}_j) = -\sum_{j(\neq i)}^{N}\nabla_i\phi(\mathbf{r}_i-\mathbf{r}_j). \tag{1.5}$$

However, the discontinuous nature of the hard sphere interaction poses a problem, since the derivative is ill-defined at contact ($r=\sigma$). In a naive integration of (1.4)

in time, particles which do not interact in one point in time may overlap in the next timestep, which is physically forbidden.

Different approaches have been proposed to address this issue. Cichocki and Hinsen proposed a method where, in each time step, particles are displaced one after the other with a random displacement, rejecting moves which result in particle overlap [38]. This leads to a series of particle positions, where the index in the series of positions can be related to real time based on the number of steps taken per particle. This approach is exact when the time step approaches zero, but systematically underestimates the self-diffusion coefficient [39]. Schaertl and Sillescu improved the accuracy of this approach by, instead of rejecting moves which create overlap, correcting the positions of overlapping particles after each time step [39]. Overlapping particles in the new particle configuration are moved along their connecting axis until they are just out of contact. Secondary overlaps (as in, those created by the correction of the primary overlaps) are ignored. While this method is an improvement, it still produces results with significant deviations from the statistical properties – e.g. the pair distribution function – measured in experiments, especially at high volume fractions [40]. Strating proposed a similar algorithm [40], but where Schaertl and Sillescu put overlapping particles just out of contact, Strating proposes to instead calculate the paths taken by the colliding particles, and handling their collision as an elastic collision. Secondary overlaps are then handled in the same way, until no overlapping pairs of particles remain and the next step can be calculated. Scala et al. took this approach a step further with event-driven Brownian dynamics, by proposing to assign a random velocity to each particle at the beginning of each time step and then using Newtonian dynamics to integrate the system until the next time step [41]. They demonstrated in their paper that this approach recovers the statistical properties of the hard sphere fluid in equilibrium. Their algorithm is meanwhile widely used to study the dynamics of the hard sphere liquid, e.g. by Leitmann et al. to study the microrheology of Brownian particles [42], by Mandal et al. to investigate the transport properties of dense hard-sphere colloidal fluids [43] by Voigtmann et al. in a study of the rheology of hard sphere suspension near the glass transition [44] and by Jung et al. to examine tagged-particle dynamics in confinement [45]. Here, we also choose to apply the event-driven Brownian dynamics method by Scala et al.

The event-driven algorithm works in detail as follows: We discretise the particle trajectories in time as a sequence of particle positions $\mathbf{r}_{i,k} = \mathbf{r}_i(t_k)$, where k is a time

index ($t_k = k\Delta t$) and Δt is some small[2] time step. We introduce an intermediate time t_m[3], which is updated stepwise for each collision event happening between t_k and t_{k+1}. The equation of motion is integrated between the times t_k and t_{k+1} as follows:

1. Calculate a displacement $\Delta\mathbf{r}_{i,k} = \dot{\mathbf{r}}_i(t_k)\Delta t$ for each particle, where $\dot{\mathbf{r}}_i$ is determined according to the Langevin equation (1.4). Calculate the projected next position $\mathbf{r}_{i,k+1} = \mathbf{r}_{i,k} + \Delta\mathbf{r}_{i,k}$ for each particle.
2. Set the intermediate time t_m equal to t_k.
3. Using the ballistic paths between particle positions $\mathbf{r}_i(t_\mathrm{m})$ and $\mathbf{r}_i(t_{k+1})$, detect particle collisions and calculate the time of collision $t_\mathrm{c}^{i,j}$ for each particle pair i, j. Discard all collisions occurring outside of the time interval $[t_\mathrm{m}, t_{k+1}]$.
4. From the remaining set of collision times, select the earliest $t_\mathrm{c} = \min(\{t_\mathrm{c}^{i,j}\})$. Set the intermediate time t_m equal to t_c and advance all particle positions to that point in time. If no collision occurs before t_{k+1}, advance until t_{k+1} and exit.
5. Handle the collision occurring at time t_c as an elastic collision. This results in new ballistic paths for the collision partners.
6. Continue from 3.

Once the time t_{k+1} is reached, the algorithm is continued from step 1 with k incremented by one. Scala and coworkers demonstrated that this scheme is accurate even with large step sizes in time [41].

1.3. Monte Carlo simulation of hard spheres

Metropolis Monte Carlo [4, 46, 47] is a method which can be used to sample the equilibrium distribution of a system of particles under the influence of an external potential. The total potential energy of a system of N particles is given by

$$U(\mathbf{r}^N) = \sum_{i=1}^{N}\sum_{j=i+1}^{N}\phi(\mathbf{r}_i - \mathbf{r}_j) + \sum_{i=1}^{N} V_\mathrm{ext}(\mathbf{r}_i), \tag{1.6}$$

[2] on the timescale τ of the particle dynamics
[3] m as in *m*eanwhile

where $\phi(\cdot)$ is the interparticle interaction potential and $V_{\text{ext}}(\cdot)$ is the external potential. Starting from a random initial configuration, the particle positions are updated stepwise, where a new position for a particle is selected with uniform probability out of a region around the old position. Then, the total energy of the new configuration is compared to the total energy of the configuration before the random move. If the total energy has decreased, the iteration moves on to the next particle. If the total energy has increased, the move is accepted with the probability $\exp(-\beta\Delta U)$, where ΔU is the change in energy. If the move is rejected, the position of the particle is reset to the old position and the iteration continues with the next particle. This procedure biases the displacement of the particles in the opposite direction of the local gradient of the external potential. In the case of hard spheres, a particle overlap results in an infinite interparticle interaction energy. Therefore, moves which result in particle overlap are always rejected. This process is repeated until an equilibrium state is reached, such that the average change in energy per accepted step is well below thermal noise. Once an equilibrium configuration has been found, the iteration process continues, producing a series of equilibrium configurations.

Both these simulation methods – Monte Carlo and Brownian Dynamics – have been developed into powerful tools for gaining an understanding of the hard sphere liquid. However, particle based simulation can be computationally expensive if the particle number is high due to large system sizes and/or high density. Additionally, understanding of the collective behaviour of many particles can be hard if we only view particle trajectories[4]. Instead, we can examine one-body quantities, such as the particle density profile and the particle current profile.

1.4. Equilibrium and dynamics in the one-body picture

The one-body level of correlation functions is connected to the many-body degrees of freedom via averages. The two central variables of interest are the time-dependent one-body density profile $\rho(\mathbf{r}, t)$ and the current profile $\mathbf{J}(\mathbf{r}, t)$. The density profile $\rho(\mathbf{r}, t)$ is the probability of finding a particle in the differential volume element $\mathrm{d}^3 r$ around $\mathbf{r}$

[4] it is easy to miss the forest for all the trees, as the saying goes

at time t. It is connected to the particle positions $\mathbf{r}_i(t)$ via

$$\rho(\mathbf{r},t)=\left\langle\sum_i\delta(\mathbf{r}-\mathbf{r}_i(t))\right\rangle, \tag{1.7}$$

where the sum is over all particles and the average is over noise and initial microstates. The initial microstates are distributed according to an equilibrium many-body distribution $\Psi_0(\{r_i\})$. The current profile $\mathbf{J}(\mathbf{r},t)$ is calculated as

$$\mathbf{J}(\mathbf{r},t)=\left\langle\sum_i\delta(\mathbf{r}-\mathbf{r}_i(t))\mathbf{v}_i(t)\right\rangle, \tag{1.8}$$

where $\mathbf{v}_i(t)=\dot{\mathbf{r}}_i(t)$ is the velocity of particle i [48, 49]. These variables are connected by the continuity equation

$$\dot{\rho}(\mathbf{r},t)=-\nabla\cdot\mathbf{J}(\mathbf{r},t), \tag{1.9}$$

which is a result of particle conservation. With an integration in time, we can rewrite the time-dependent density profile as

$$\rho(\mathbf{r},t)=\rho(\mathbf{r},0)-\int_0^t \mathrm{d}t'\nabla\cdot\mathbf{J}(\mathbf{r},t'). \tag{1.10}$$

With a given initial condition $\rho(\mathbf{r},0)$, knowledge of $\mathbf{J}(\mathbf{r},t)$ thus determines the density profile $\rho(\mathbf{r},t)$ for $t>0$. The current profile is determined by the force balance equation

$$\gamma\mathbf{J}(\mathbf{r},t)=-\mathrm{k_B}T\nabla\rho(\mathbf{r},t)+\rho(\mathbf{r},t)\left[\mathbf{f}^{\mathrm{int}}(\mathbf{r},t)+\mathbf{f}^{\mathrm{ext}}(\mathbf{r},t)\right], \tag{1.11}$$

where the total internal one-body force field $\mathbf{f}^{\mathrm{int}}(\mathbf{r},t)$ is linked to the Langevin picture by the configurational average

$$\mathbf{f}^{\mathrm{int}}(\mathbf{r},t)=\frac{1}{\rho(\mathbf{r},t)}\left\langle\sum_{i=1}^{N}\delta(\mathbf{r}-\mathbf{r}_i(t))\mathbf{f}_i^{\mathrm{int}}(\mathbf{r}^N(t))\right\rangle, \tag{1.12}$$

where $\mathbf{f}^{\mathrm{int}}(\mathbf{r}^N(t))$ is the many-particle internal force field as defined in (1.5). In order to have a complete and self-contained theory of the one-body dynamics, a way is needed to determine the internal force field from the density profile and current profile. One approach to achieve this is dynamic density functional theory (section 1.8), but this theory neglects a whole class of force contributions. The exact formalism to

determine the internal force field in the one-body picture is power functional theory (section 1.9). In equilibrium, $\mathbf{J}(\mathbf{r},t)=0$, and thus the density profile does not depend on time $\rho(\mathbf{r},t)=\rho(\mathbf{r},0)=\rho_0(\mathbf{r})$. For a given system under the influence of an external potential, the equilibrium density $\rho_0(\mathbf{r})$ can be calculated with density functional theory (see section 1.7).

With these tools, we examine two aspects of the dynamics of hard spheres: The bulk van Hove function of the hard sphere fluid and the hard sphere fluid under the influence of an inhomogeneous shear force field that is switched on or off.

1.5. van Hove function and the dynamical test particle limit

The density profile and current profile are one-body variables. But there exists a whole hierarchy of higher-order correlations between multiple bodies [4]. These higher-order correlations can reveal structure even in situations where the density profile is uniform. One important two-body correlation function is the van Hove function $G(\mathbf{r},t)$, which is defined [4, 50] for a bulk fluid as

$$G(\mathbf{r},t)=\left\langle \frac{1}{N}\sum_{i=1}^{N}\sum_{j=1}^{N}\delta(\mathbf{r}+\mathbf{r}_i(0)-\mathbf{r}_j(t))\right\rangle, \tag{1.13}$$

where, in the Langevin picture, the average is over noise and initial microstates [4]. This function is proportional to the probability of finding a particle at position $\mathbf{r}$ at time t, given that there was a particle at the origin at time 0. The van Hove function can be split into two parts, where the *self* part $G_s(\mathbf{r},t)$ corresponds to the probability of finding the same particle which was at the origin, and the *distinct* part $G_d(\mathbf{r},t)$ corresponds to the probability of finding a different particle. To calculate both of these components of $G(\mathbf{r},t)$, we split the double sum in (1.13) into

$$\begin{aligned} G(\mathbf{r},t) &= G_s(\mathbf{r},t)+G_d(\mathbf{r},t) \\ &= \frac{1}{N}\left\langle \sum_{i=1}^{N}\delta(\mathbf{r}+\mathbf{r}_i(0)-\mathbf{r}_i(t))\right\rangle + \frac{1}{N}\left\langle \sum_{i=1}^{N}\sum_{j\neq i}^{N}\delta(\mathbf{r}+\mathbf{r}_i(0)-\mathbf{r}_j(t))\right\rangle. \end{aligned} \tag{1.14}$$

For $t=0$ the distinct van Hove function is equal to the radial distribution function $g(r)=G_d(r,0)$, where $r\equiv|\mathbf{r}|$ is the modulus.

The radial distribution function can be calculated in density functional theory (section 1.7) with a second functional derivative of the excess free energy functional [17], using the Ornstein-Zernike equation [51]. However, this does not allow for the calculation of dynamical correlations like the van Hove function. A nonequilibrium Ornstein-Zernike equation, which allows calculation of $G(\mathbf{r}, t)$ in principle, was presented by Brader and Schmidt [52]. Another path to the van Hove function is the dynamical test particle limit, where the bulk van Hove function is mapped onto the one-body density profile of a nonequilibrium system. This approach was first presented by Percus [53] for the static case (time $t = 0$) and later extended to the full van Hove function by Archer and coworkers within dynamic density functional theory (section 1.8) [48]. Brader and Schmidt then presented a formally exact formulation of the dynamic test particle limit in the framework of power functional theory (see section 1.9 for one-component PFT or section 1.10 for PFT in the dynamic test particle limit) [54].

In a simulation, we can select one particle out of an equilibrium microstate as the *test particle*. Then, we can shift the coordinate system such that this particle is at the origin at some arbitrary fixed time $t = 0$. In the thermodynamic limit for N particles in a volume V, where $N, V \to \infty$ with the bulk number density $\rho_\mathrm{B} = N/V = \text{const}$, the dynamic density $\rho_\mathrm{d}(\mathbf{r}, t)$ of all particles except the test particle is equal to the distinct van Hove function

$$G_\mathrm{d}(\mathbf{r}, t) = \rho_\mathrm{d}(\mathbf{r}, t), \tag{1.15}$$

and the density $\rho_\mathrm{s}(\mathbf{r}, t)$ of the test particle is equal to the self van Hove function

$$G_\mathrm{s}(\mathbf{r}, t) = \rho_\mathrm{s}(\mathbf{r}, t). \tag{1.16}$$

This test particle system can be viewed as a binary mixture with a special initial condition, where the constituent particles of both components are identical except for the labelling as either *self* particle or *distinct* particle.

The van Hove function, or its spatial Fourier transform, the intermediate scattering function $F(\mathbf{k}, t)$, of the hard sphere fluid has been studied extensively. Mode-coupling theory (MCT) has been applied to study the intermediate scattering function in an effort to understand the dynamics of hard-sphere systems [55] and the glass transition [56, 57], one of the long-standing puzzles of condensed matter theory [58]. However, understanding the real-space properties and the decay processes in the van Hove function is by no means complete. Hopkins et al. presented theoretical predictions

of the bulk hard sphere van Hove function [49] using dynamic density functional theory (DDFT) with the simple Ramakrishnan–Yussouff approximation [59] for internal interactions. Stopper and coworkers improved and extended these results [60, 61] using a modified version of the White Bear Mk. II version of Rosenfeld's fundamental measure theory [62] and extended DDFT by introducing a local particle mobility. Nevertheless, an understanding of the internal one-body forces acting in the hard sphere fluid in the dynamic test particle limit is still missing. We could show that there is no sufficiently accurate model for adiabatic forces acting in the dynamics of the van Hove function [3], and to our knowledge there has been no study of the van Hove function – previously to ours – which includes superadiabatic forces explicitly.

1.6. Hard spheres under shear

One of the fundamental properties of a fluid is viscosity, which is the resistance of the fluid against deformation. We discriminate between bulk (or volume) viscosity, which is the viscosity of a fluid in response to compression or expansion, and the shear viscosity, which acts in response to deformations which do not change the volume of the fluid. The viscosity of the hard sphere fluid, and its other transport coefficients, has been the subject of a considerable body of research, starting with pioneering work of Alder, Gass, and Wrainwright, who studied the hard sphere fluid using molecular dynamics simulations [63]. This simulation approach has been continued by Naitoh and Ono [64], Erpenbeck and Wood [65–67] and Sigurgeirsson and Heyes [68].

Here, we study shear in a planar system, where – after the system has settled into a steady state – the current profile is of the form

$$\mathbf{J}(\mathbf{r}) = \rho(x)v(x)\hat{\mathbf{e}}_z, \tag{1.17}$$

where $\rho(x)$ is the density profile, $v(x)$ is the velocity profile and $\hat{\mathbf{e}}_z$ is the unit vector in z direction. We also discuss the transient behaviour that occurs in between equilibrium and the steady state. A typical situation is linear shear, where the velocity profile $v(x)$ varies linearly with x

$$v(x) = \dot{\gamma}x, \tag{1.18}$$

where $\dot{\gamma} = \partial v(x)/\partial x$ is called the shear rate. The shear viscosity of the hard sphere fluid is in general not independent of the shear rate [66]. In molecular dynamics

simulations of hard spheres, it has been found that with increasing shear rate, the shear viscosity first decreases (shear thinning), then increases again (shear thickening) [69]. Local variations in the shear rate can induce variations in the density profile of a previously homogeneous system [70]. Examples include lane formation, where the density profile varies periodically perpendicular to the flow direction [37, 71, 72], shear banding, where bands of constant shear rate coexist [73–75] and particle migration due to inhomogeneous shear rate [31, 76–81].

1.7. Classical density functional theory

Density functional theory (DFT) is a theoretical framework for the description of the statistical properties of condensed matter systems [16, 17]. DFT can be used in situations both with or without an external potential. At its core is the grand potential functional

$$\Omega[\rho] = F_{\mathrm{id}}[\rho] + F_{\mathrm{exc}}[\rho] + \int \mathrm{d}^3 r\, \rho(\mathbf{r})\left(V_{\mathrm{ext}}(\mathbf{r}) - \mu\right), \tag{1.19}$$

where the ideal free energy functional $F_{\mathrm{id}}[\rho] = \mathrm{k_B}T \int \mathrm{d}^3 r\, \rho\left(\ln(\lambda^3\rho) - 1\right)$ with thermal de Broglie wavelength λ is the ideal gas contribution to the free energy functional, $F_{\mathrm{exc}}[\rho]$ is the excess (over-ideal) free energy functional, $V_{\mathrm{ext}}(\mathbf{r})$ is the external potential, and μ is the chemical potential. This functional $\Omega[\rho]$ can be minimised with respect to the density profile to obtain the equilibrium density profile of the system. The minimisation can be expressed as the variational principle

$$\left.\frac{\delta\Omega[\rho]}{\delta\rho(\mathbf{r})}\right|_{\rho_0(\mathbf{r})} = 0 \quad (\text{min}), \tag{1.20}$$

where $\delta/\delta f(\mathbf{r})$ is the functional derivative with respect to the (generic) function $f(\mathbf{r})$, and $\rho_0(\mathbf{r})$ denotes the equilibrium density profile. The equation (1.20) can formally be solved for $\rho_0(\mathbf{r})$, which leads to the Euler-Lagrange-equation

$$\rho_0(\mathbf{r}) = \lambda^{-3} \exp\left(-\beta\left[\left.\frac{\delta F_{\mathrm{exc}}[\rho]}{\delta\rho(\mathbf{r})}\right|_{\rho_0(\mathbf{r})} + V_{\mathrm{ext}}(\mathbf{r}) - \mu\right]\right). \tag{1.21}$$

Equation (1.21) is an implicit equation for the equilibrium density profile $\rho_0(\mathbf{r})$. It can be solved e.g. with Piccard iteration [19] by starting from an initial guess for $\rho_0(\mathbf{r})$

and refining it. Appendix A covers Piccard iteration as well as solutions based on gradient-based optimisation techniques, with a discussion of the challenges arising in systems with spherical symmetry, which is relevant for our treatment of the van Hove function, below in section 2.3.

The enormous power of DFT lies in the splitting of the grand potential functional into external, ideal and excess contributions. If the excess free energy functional for a given interparticle interaction potential is known, the system can be studied in a wide range of conditions because of that splitting. To give a very much non-exhaustive list of examples: Monson gave a review of the theory of adsorption/desorption hysteresis for fluids in porous materials using DFT [82]. Chaćon and Tarazona studied the link between DFT and capillary wave theory for liquid interfaces [83]. Chacko et al. used DFT to study the solvent mediated forces between pairs of blocks immersed in a simple liquid [84]. Lutsko studied the crystallisation of a Lennard-Jones fluid in droplets with DFT [85].

All these achievements hinge on the knowledge of accurate approximations for the excess free energy functional. With the notable exception of one-dimensional hard rods [20], the excess free energy functional $F_{\text{exc}}[\rho]$ must be approximated [19]. Thankfully, high-quality functionals are available for a range of interparticle interactions. These are often based on Weeks-Chandler-Andersen decomposition [86] of the interparticle interaction into a hard-sphere core and a longer-range tail. Examples include sticky hard spheres [87], the Lennard-Jones-fluid [88] or charged hard spheres [89]. An accurate $F_{\text{exc}}[\rho]$ for hard spheres is therefore not only important for the hard sphere fluid itself, but as an ingredient in the description of other model fluids. Fundamental measure theory (FMT) allows for the construction of very accurate excess functionals for hard spheres [19].

1.7.1. Fundamental measure theory

For hard spheres, fundamental measure theory (FMT) has been very successful in producing high accuracy approximations for $F_{\text{exc}}[\rho]$ [19, 90, 91]. The excess free energy is expressed as a functional of a set of weighted densities, which are calculated from

the local density profile $\rho(\mathbf{r})$ by a convolution with a weight function:

$$n_\alpha(\mathbf{r}) = \int \mathrm{d}^3 r' \rho(\mathbf{r}') \omega_\alpha(\mathbf{r} - \mathbf{r}'). \tag{1.22}$$

The weight functions $\omega_\alpha(\mathbf{r})$ correspond to the geometric properties of the spheres (volume, surface, mean radius of curvature and Euler-Poincaré characteristic), hence the name „fundamental measure“. The exact set of weighted densities differs slightly between different FMT functionals. In our study of the sheared hard sphere fluid [1] (see section 2.2), we apply the „classic“ Rosenfeld functional with q_3 correction [19, 22, 92], which is based on the following weight functions:

$$\omega_3(\mathbf{r}) = \Theta(R - |\mathbf{r}|), \tag{1.23}$$

$$\omega_2(\mathbf{r}) = \delta(R - |\mathbf{r}|) = 4\pi R^2 \omega_0(\mathbf{r}) = 4\pi R \omega_1(\mathbf{r}), \tag{1.24}$$

$$\boldsymbol{\omega}_2(\mathbf{r}) = \frac{\mathbf{r}}{|\mathbf{r}|} \omega_2(\mathbf{r}) = 4\pi R \boldsymbol{\omega}_1(\mathbf{r}), \tag{1.25}$$

with Heaviside step function $\Theta(\cdot)$, Dirac delta distribution $\delta(\cdot)$, and sphere radius $R = \sigma/2$. Integration over these weight function gives a volume integral over the sphere volume (for ω_3), a scalar surface integral over the sphere surface (for ω_2), and a vector integral over the sphere surface (for $\boldsymbol{\omega}_2$). One should note that this assumes monodisperse hard spheres, but the theory is applicable to mixtures of spheres with different radii as well [19]. These weight functions are used to calculate the weighted densities n_0, n_1, n_2, n_3, $\mathbf{n}_1$ and $\mathbf{n}_2$ [19].

In our studies of the van Hove function [2, 3] (see section 2.3), we apply the White Bear Mk. II version of FMT [62] with Tarazona's tensorial modification [23]. This involves a further weighted density $\mathbf{n}_{\mathrm{m}_2}(\mathbf{r})$ with the weight function [19]

$$\boldsymbol{\omega}_{\mathrm{m}_2}(\mathbf{r}) = \left(\frac{1}{r^2} \mathbf{r}\mathbf{r} - \frac{1}{3} \mathbb{1} \right) \omega_2(\mathbf{r}), \tag{1.26}$$

which is a 3×3 matrix.

The excess free energy functional is then

$$F_{\mathrm{exc}}[\rho] = \int \mathrm{d}^3 r \Phi(n_\alpha) \tag{1.27}$$

with either the Rosenfeld (q3) version

$$\Phi_{\mathrm{RF}} = -n_0 \ln(1-n_3) + \frac{n_1 n_2 - \mathbf{n}_1 \cdot \mathbf{n}_2}{1-n_3} + \frac{n_2^3 \left(1 - \left(\frac{\mathbf{n}_2}{n_2}\right)^2\right)^3}{24\pi(1-n_3)^2}, \tag{1.28}$$

or the tensorial White Bear Mk. II version

$$\begin{aligned}\Phi^{\mathrm{T}}_{\mathrm{WBII}} = &- n_0 \ln(1-n_3) + (n_1 n_2 - \mathbf{n}_1 \cdot \mathbf{n}_2) \frac{1 + \frac{1}{3}\phi_2(n_3)}{1-n_3} \\ &+ \left[n_2^3 - 3 n_2 \mathbf{n}_2 \cdot \mathbf{n}_2 + \frac{9}{2}\left(2\mathbf{n}_2 \mathbf{n}_{\mathrm{m}_2} \mathbf{n}_2 - \mathrm{Tr}\ \mathbf{n}_{\mathrm{m}_2}^3\right)\right] \frac{1 - \frac{1}{3}\phi_3(n_3)}{24\pi(1-n_3)^2},\end{aligned} \tag{1.29}$$

where Tr denotes the trace, and

$$\phi_2(n_3) = \frac{1}{n_3}\left(2n_3 - n_3^2 + 2(1-n_3)\ln(1-n_3)\right) \tag{1.30}$$

$$\phi_3(n_3) = \frac{1}{n_3^2}\left(2n_3 - 3n_3^2 + 2n_3^3 + 2(1-n_3)^2 \ln(1-n_3)\right). \tag{1.31}$$

To solve eq. (1.21), we also need to calculate the functional derivative

$$\frac{\delta F[\rho(\mathbf{r}')]}{\delta \rho(\mathbf{r})} = \sum_\alpha \int \mathrm{d}^3 r' \frac{\partial \Phi(\mathbf{r}')}{\partial n_\alpha(\mathbf{r}')} \frac{\delta n_\alpha(\mathbf{r}')}{\delta \rho(\mathbf{r})} = \sum_\alpha \int \mathrm{d}^3 r' \frac{\partial \Phi(\mathbf{r}')}{\partial n_\alpha(\mathbf{r}')} \omega_\alpha(\mathbf{r}' - \mathbf{r}), \tag{1.32}$$

which can be calculated – as written here – as a sum over partial derivatives with respect to the weighted densities.

The systems studied in this thesis – the van Hove function and the sheared fluid – can both be reduced to quasi one-dimensional problems. In the sheared system, $\rho(\mathbf{r}) = \rho(x)$ depends only on a single Cartesian coordinate, and the bulk van Hove function is radially symmetric, such that the test particle densities $\rho_\alpha(\mathbf{r}) = \rho_\alpha(r)$ depend only on the modulus $|\mathbf{r}| = r$. In these cases, the other degrees of freedom in (1.22) can be integrated out to obtain effective weight functions which depend only on x or r, respectively (see appendix B).

1.7.2. DFT in the static test particle limit

In section 1.5, we have introduced the idea of the dynamic test particle limit, where there exists a correspondence between the van Hove function and the density profiles

in a binary fluid with a special initial condition. The idea of the test particle limit was first proposed in the static case by Percus [53]. Since the position of the test particle, and thus its density profile, is known by definition ($\rho_s(\mathbf{r}) = \delta(\mathbf{r})$), the influence of the test particle on the rest of the system can be modelled via an external potential $V_{\text{ext}}(\mathbf{r})$ that is equal to the pair potential $\phi(\mathbf{r})$ (see equation (1.1) for the case of hard spheres) with one particle fixed at the origin. The equilibrium density profile $\rho_0(\mathbf{r})$ of this system can be calculated using the Euler-Lagrange equation of DFT (equation (1.20)) and is then related to the radial distribution function via

$$\rho_0(\mathbf{r}) = \rho_B g(\mathbf{r}), \tag{1.33}$$

where ρ_B is the bulk density of the system (see section 1.5).

1.8. Dynamic density functional theory

DFT is a method for the study of equilibrium systems, but it has been extended to non-equilibrium systems, resulting in dynamic density functional theory (DDFT) [17, 25–27]. A phenomenological equation of motion was first proposed by Evans [17]. Marconi and Tarazona re-derived the theory from the Langevin equation [25, 26], Espanõl and Löwen did it again using projection operators [93], and Archer and Evans derived it starting from the many-body Smoluchowski equation [27].

The following section is not meant as another re-derivation of DDFT, but rather as a short sketch of the steps necessary to arrive at the DDFT equation of motion for the density profile.

For a given external force $\mathbf{f}^{\text{ext}}(\mathbf{r}, t)$ we want to know the time evolution of the density profile $\rho(\mathbf{r}, t)$ in response to that force. The time evolution of the density profile is calculated from the DFT free energy functional with the adiabatic approximation [28, 94]: At a fixed point in the time evolution of the nonequilibrium system, we construct an adiabatic potential $V_t^{\text{ad}}(\mathbf{r})$ such that the equilibrium density profile $\rho_0(\mathbf{r}) = \rho_t^{\text{ad}}(\mathbf{r})$ for that potential is equal to the non-equilibrium density profile $\rho(\mathbf{r}, t)$. The assumption is then that the current of the nonequilibrium system moves along the (positive) gradient of the adiabatic potential (plus the external force), namely

$$\gamma \mathbf{J}^{\text{ad}}(\mathbf{r}, t) = \rho_t^{\text{ad}}(\mathbf{r}) \left[\nabla V_t^{\text{ad}}(\mathbf{r}) + \mathbf{f}^{\text{ext}}(\mathbf{r}, t) \right]. \tag{1.34}$$

From equation (1.20) with $\rho_0(\mathbf{r}) = \rho_t^{\mathrm{ad}}(\mathbf{r}) = \rho(\mathbf{r},t)$ follows that

$$\left.\frac{\delta\Omega[\rho]}{\delta\rho(\mathbf{r})}\right|_{\rho(\mathbf{r},t)} = \left.\frac{\delta F_{\mathrm{id}}[\rho]}{\delta\rho(\mathbf{r})}\right|_{\rho(\mathbf{r},t)} + \left.\frac{\delta F_{\mathrm{exc}}[\rho]}{\delta\rho(\mathbf{r})}\right|_{\rho(\mathbf{r},t)} + V_t^{\mathrm{ad}}(\mathbf{r}) - \mu \tag{1.35}$$

$$= \mathrm{k_B}T\ln\left(\lambda^3\rho(\mathbf{r},t)\right) + \left.\frac{\delta F_{\mathrm{exc}}[\rho]}{\delta\rho(\mathbf{r})}\right|_{\rho(\mathbf{r},t)} + V_t^{\mathrm{ad}}(\mathbf{r}) - \mu = 0. \tag{1.36}$$

Therefore

$$\begin{aligned}\mathbf{J}^{\mathrm{ad}}(\mathbf{r},t) &= -\frac{\rho(\mathbf{r},t)}{\gamma}\left[\nabla\left(\mathrm{k_B}T\ln\left(\lambda^3\rho(\mathbf{r},t)\right) + \left.\frac{\delta F_{\mathrm{exc}}[\rho]}{\delta\rho(\mathbf{r})}\right|_{\rho(\mathbf{r},t)} - \mu\right) - \mathbf{f}^{\mathrm{ext}}(\mathbf{r},t)\right] \\ &= -D\nabla\rho(\mathbf{r},t) - \frac{\rho(\mathbf{r},t)}{\gamma}\nabla\left.\frac{\delta F_{\mathrm{exc}}[\rho]}{\delta\rho(\mathbf{r})}\right|_{\rho(\mathbf{r},t)} + \frac{\rho(\mathbf{r},t)}{\gamma}\mathbf{f}^{\mathrm{ext}}(\mathbf{r},t).\end{aligned} \tag{1.37}$$

The time evolution of the density profile then follows the partial differential equation

$$\begin{aligned}\dot{\rho}(\mathbf{r},t) &= -\nabla\cdot\mathbf{J}^{\mathrm{ad}}(\mathbf{r},t) \\ &= D\nabla^2\rho(\mathbf{r},t) + \nabla\cdot\frac{\rho(\mathbf{r},t)}{\gamma}\nabla\left.\frac{\delta F_{\mathrm{exc}}[\rho]}{\delta\rho(\mathbf{r})}\right|_{\rho(\mathbf{r},t)} - \nabla\cdot\frac{\rho(\mathbf{r},t)}{\gamma}\mathbf{f}^{\mathrm{ext}}(\mathbf{r},t),\end{aligned} \tag{1.38}$$

where $\nabla^2 = \nabla\cdot\nabla$ is the Laplace operator. In the case of the ideal gas, the excess free energy is zero, and (1.38) is exact. However, the equation of motion (1.38) is not exact for interacting particles, even if one had an exact excess free energy functional, since superadiabatic forces are missing by construction [28].

1.9. Power functional theory

A different path to a theory of non-equilibrium many-body dynamics in the one-body picture has been presented by Schmidt and Brader [28] under the name of power functional theory (PFT). This theoretical framework is a formally exact formulation of Brownian dynamics on the one-body level (variants for Newtonian dynamics [95] and quantum dynamics [96] exist). The authors proposed a functional and a variational principle to obtain an Euler-Lagrange equation for the current profile $\mathbf{J}(\mathbf{r},t)$, similar to DFT. For a known density profile $\rho(\mathbf{r},t)$ at a fixed time t, the power functional $R_t[\rho,\mathbf{J}]$

is minimised with respect to the trial current $\mathbf{J}(\mathbf{r},t)$ to obtain the physically realised current $\mathbf{J}_0(\mathbf{r},t)$:

$$\left.\frac{\delta R_t[\rho,\mathbf{J}]}{\delta \mathbf{J}(\mathbf{r},t)}\right|_{\mathbf{J}_0(\mathbf{r},t)} = 0 \quad \text{(min)}. \tag{1.39}$$

It is important to note that this functional derivative is taken at a fixed time t, that is, it is a variation of $R_t[\rho,\mathbf{J}]$ with respect to a function of space. In general, however, $R_t[\rho,\mathbf{J}]$ depends on the values of $\rho(\mathbf{r},t)$ and $\mathbf{J}(\mathbf{r},t)$ at times earlier than t. With the current profile thus determined, the continuity equation (1.9) is used to calculate the change in the density profile. Together, these equations are used to determine the time evolution of $\rho(\mathbf{r},t)$.

The functional R_t consists of multiple components

$$R_t[\rho,\mathbf{J}] = P_t^{\text{id}}[\rho,\mathbf{J}] + P_t^{\text{exc}}[\rho,\mathbf{J}] + \dot{F}[\rho] - X_t[\rho,\mathbf{J}], \tag{1.40}$$

where the ideal dissipation functional is

$$P_t^{\text{id}}[\rho,\mathbf{J}] = \gamma \int \mathrm{d}^3 r \, \frac{\mathbf{J}(\mathbf{r},t)^2}{2\rho(\mathbf{r},t)}, \tag{1.41}$$

the time derivative of the free energy functional is

$$\dot{F}[\rho] = \int \mathrm{d}^3 r \mathbf{J}(\mathbf{r},t) \cdot \nabla \left.\frac{\delta F[\rho]}{\delta \rho(\mathbf{r})}\right|_{\rho(\mathbf{r},t)}, \tag{1.42}$$

and the external power is

$$X_t[\rho,\mathbf{J}] = \int \mathrm{d}^3 r \left(\mathbf{J}(\mathbf{r},t) \cdot \mathbf{f}^{\text{ext}}(\mathbf{r},t) - \rho(\mathbf{r},t)\dot{V}_{\text{ext}}(\mathbf{r},t)\right), \tag{1.43}$$

with the external force $\mathbf{f}^{\text{ext}}(\mathbf{r},t)$ and the external potential $V_{\text{ext}}(\mathbf{r},t)$. The superadiabatic power functional is $P_t^{\text{exc}}[\rho,\mathbf{J}]$, which is in general unknown and must be approximated. With this splitting we get from (1.39)

$$\gamma \frac{\mathbf{J}(\mathbf{r},t)}{\rho(\mathbf{r},t)} + \left.\frac{\delta P_t^{\text{exc}}[\rho,\mathbf{J}]}{\delta \mathbf{J}(\mathbf{r},t)}\right|_{\mathbf{J}(\mathbf{r},t)=\mathbf{J}_0(\mathbf{r},t)} + \nabla \left.\frac{\delta F[\rho]}{\delta \rho(\mathbf{r})}\right|_{\rho(\mathbf{r})=\rho(\mathbf{r},t)} - \mathbf{f}^{\text{ext}}(\mathbf{r},t) = 0, \tag{1.44}$$

and

$$\begin{aligned}\mathbf{J}(\mathbf{r},t) = &-D\nabla\rho(\mathbf{r},t) - \frac{\rho(\mathbf{r},t)}{\gamma}\nabla\left.\frac{\delta F_{\text{exc}}[\rho]}{\delta\rho(\mathbf{r})}\right|_{\rho(\mathbf{r},t)} + \frac{\rho(\mathbf{r},t)}{\gamma}\mathbf{f}^{\text{ext}}(\mathbf{r},t) \\ &- \frac{\rho(\mathbf{r},t)}{\gamma}\left.\frac{\delta P_t^{\text{exc}}[\rho,\mathbf{J}]}{\delta\mathbf{J}(\mathbf{r},t)}\right|_{\mathbf{J}_0(\mathbf{r},t)} \\ = &\frac{\rho(\mathbf{r},t)}{\gamma}\left[\mathbf{f}^{\text{id}}(\mathbf{r},t) + \mathbf{f}^{\text{ad}}(\mathbf{r},t) + \mathbf{f}^{\text{ext}}(\mathbf{r},t) + \mathbf{f}^{\text{sup}}(\mathbf{r},t)\right],\end{aligned} \tag{1.45}$$

where $\mathbf{f}^{\text{id}}(\mathbf{r},t) = -\mathrm{k_B}T\nabla\ln(\rho(\mathbf{r},t))$ is the ideal force field, $\mathbf{f}^{\text{ad}}(\mathbf{r},t) = -\nabla\left.\frac{\delta F_{\text{exc}}[\rho]}{\delta\rho(\mathbf{r},t)}\right|_{\rho(\mathbf{r},t)}$ is the adiabatic force field and $\mathbf{f}^{\text{sup}}(\mathbf{r},t) = -\left.\frac{\delta P_t^{\text{exc}}[\rho,\mathbf{J}]}{\delta\mathbf{J}(\mathbf{r},t)}\right|_{\mathbf{J}_0(\mathbf{r},t)}$ is the superadiabatic force field. A comparison between (1.45) and (1.37) shows that, with the approximation $\mathbf{f}^{\text{sup}} = 0$, PFT reduces to the equation of motion of DDFT.

The remaining – and central – challenge is the formulation of a good approximation for the superadiabatic power functional $P_t^{\text{exc}}[\mathbf{J},\rho]$, which is as universally applicable in various physical situations as state-of-the-art approximations for the excess free energy functional are in DFT. Just as the excess free energy functional, the superadiabatic power functional is in principle specific to the interparticle interaction potential. The central objective of this thesis is to find a good approximation for the superadiabatic power functional for hard spheres. Such an approximation is of similar importance to PFT as the development of high-quality excess free energy functionals is for DFT. We focus especially on the inclusion of memory effects. We can build on previous work: de las Heras and Schmidt proposed a velocity gradient superadiabatic power functional for Brownian dynamics [30]. They demonstrated that the proposed functional models viscoelastic forces and recovers the Stokes form of hydrodynamics in the case of constant density and viscosity. Stuhlmüller et al. studied structural forces in driven colloidal systems using PFT [31] and presented a superadiabatic functional which drives particle migration out of regions of high shear rate. Geigenfeind et al. presented an approximate superadiabatic power functional for binary colloidal mixtures [37] and showed how forces arising from this functional can lead to laning, mixing or jamming in driven binary systems.

In chapter 2, we extend these approximations and combine them to obtain an approximation for superadiabatic forces with applications which extend far beyond the original studies that our work is based on.

1.10. Dynamic test particle limit revisited: DDFT and PFT

In section 1.5, we have shown the construction of the dynamic test particle limit. In section 1.8 and section 1.9, we have shown the construction of an equation of motion for the density of a one-component system using, respectively, DDFT and PFT. Now, we revisit these equations of motion and show the form they take in the case of the dynamic test particle limit. To this end, we make use of PFT (or DDFT) for mixtures [54]. As stated in section 1.5, we split a system of identical particles into two components by labelling one particle as the test particle, and the rest of the particles as distinct particles. We thus have two density components $\rho_\alpha(\mathbf{r},t)$ with $\alpha = \mathrm{s},\mathrm{d}$, each of which is connected to its respective current profile $\mathbf{J}_\alpha(\mathbf{r},t)$ via the continuity equation

$$\frac{\partial}{\partial t}\rho_\alpha(\mathbf{r},t) = -\nabla\cdot\mathbf{J}_\alpha(\mathbf{r},t). \tag{1.46}$$

The normalisation of the density components is chosen such that

$$\int_V \mathrm{d}^3 r\, \rho_\mathrm{s}(\mathbf{r},t) = 1 \quad \text{and} \tag{1.47}$$

$$\int_V \mathrm{d}^3 r\, \rho_\mathrm{d}(\mathbf{r},t) = N-1. \tag{1.48}$$

The initial condition is

$$\rho_\mathrm{s}(\mathbf{r},0) = \delta(\mathbf{r}) \quad \text{and} \tag{1.49}$$

$$\rho_\mathrm{d}(\mathbf{r},t) = \rho_\mathrm{B} g(r). \tag{1.50}$$

The total free power functional for this mixture is given by

$$R_t[\{\rho_\alpha,\mathbf{J}_\alpha\}] = \dot{F}[\{\rho_\alpha\}] + \sum_\alpha P_t^\mathrm{id}[\rho_\alpha,\mathbf{J}_\alpha] + P_t^\mathrm{exc}[\{\rho_\alpha,\mathbf{J}_\alpha\}] - \sum_\alpha X_t[\rho_\alpha,\mathbf{J}_\alpha], \tag{1.51}$$

(compare equation (1.40) for the one-component case) and the Euler-Lagrange equation for each current component is given by the functional derivative of $R_t[\{\rho_\alpha,\mathbf{J}_\alpha\}]$ with respect to that current (compare equation 1.39). Here, the ideal dissipation functional $P_t^\mathrm{id}[\rho_\alpha,\mathbf{J}_\alpha]$ and the external power $X_t[\rho_\alpha,\mathbf{J}_\alpha]$ are identical to their one-component counterparts. The superadiabatic free power functional $P_t^\mathrm{exc}[\{\rho_\alpha,\mathbf{J}_\alpha\}]$ can be split into

contributions that depend on species-labelled information, and those contributions that only depend on the full density profile $\rho(\mathbf{r},t)=\rho_s(\mathbf{r},t)+\rho_d(\mathbf{r},t)$ and on the full current profile $\mathbf{J}(\mathbf{r},t)=\mathbf{J}_s(\mathbf{r},t)+\mathbf{J}_d(\mathbf{r},t)$. Our approximation for $P_t^{\text{exc}}[\{\rho_\alpha,\mathbf{J}_\alpha\}]$, and its constituent contributions, is given in section 2.1. To obtain DDFT for the dynamic test particle limit, set $P_t^{\text{exc}}[\{\rho_\alpha,\mathbf{J}_\alpha\}]$ to zero.

The intrinsic free energy functional $F[\rho_s,\rho_d]$ splits as follows:

$$F[\rho_s,\rho_d]=F_{\text{id}}[\rho_s]+F_{\text{id}}[\rho_d]+F_{\text{exc}}[\rho_s,\rho_d], \tag{1.52}$$

where the ideal free energy $F_{\text{id}}[\rho_\alpha]$ is again identical to its one-component counterpart, but the construction of the excess free energy $F_{\text{exc}}[\rho_s,\rho_d]$ is less straightforward. In general, for a mixture of identical hard spheres, we would have $F_{\text{exc}}[\rho_s,\rho_d]=F_{\text{exc}}[\rho]$, since the excess free energy does not depend on the separation into two different species of particles. However, in the test particle limit case, $\rho_s(\mathbf{r})$ represents a single particle, which DFT does not readily support, since it is formulated in the grand canonical ensemble[5]. Therefore, a density which is normalised to unity represents an *average* of one particle instead of exactly one particle [97]. This distinction is negligible for large numbers of particles, but for a single particle, it leads to major deviations [97]. This problem is known as the self interaction problem.

Stopper and coworkers studied multiple approaches to mitigate this issue [60, 61]. These range from a linearisation of $F_{\text{exc}}[\rho]$ around $\rho_s(\mathbf{r})=0$ [60]; a partial linearisation, where the linearised $F_{\text{exc}}[\rho]$ is only used to calculate forces on ρ_s [60]; to a *quenched* functional approach, where $F_{\text{exc}}[\rho_s,\rho_d]=F_{\text{exc}}[\rho]-F_{\text{exc}}[\rho_s]$ [61]. In [3], we closely examine those approaches by comparing the predicted forces to measurements obtained in particle simulations. We find that all three approaches show significant deviations from simulation results. Out of the three, the quenched functional is the most accurate.

[5] except for in the limit of a single hard particle in a cavity at $\mu\to\infty$

2. Overview of the results

In this chapter, we give an overview of the results from the publications reproduced in chapter 5. First, we introduce our approximation for superadiabatic forces in power functional theory (PFT), continuing the theoretical section 1.9 from the introduction. Then, we show how we validated this approximation.

In the first study contributing to this thesis [1], we examine the hard sphere fluid which is driven out of equilibrium by a shear force field. Using BD simulation and PFT, we examine the onset and decay of the resulting current profile as well as the properties of the current profile in steady state. We focus in this study on viscoelastic forces acting within the system in response to the external force. The approximation of the viscoelastic forces relies on memory, which can be modelled to be either spatially local or non-local. In the non-local variant, each point in space is coupled to other points in space via a diffusive process. We thus call this variant *diffusive memory*. We evaluate whether or not spatially nonlocal memory is required to accurately describe the viscoelastic forces. Indeed, spatially local memory is insufficient to reproduce the forces even qualitatively, and thus the nonlocal variant must be used.

The insights gained are used in the second and third publication [2, 3], where we study the hard sphere van Hove function using BD simulation as well as PFT. The internal forces acting on the van Hove function are split into adiabatic and superadiabatic contributions with the help of Monte Carlo (MC) simulations. Here we add memoryless drag forces and structural nonequilibrium forces with diffusive memory to our approximation of the superadiabatic power functional. We demonstrate how, with the mentioned contributions, our approximation accurately captures the behaviour of the van Hove function. Finally, we lay out why we trust to have found a universal approximation for superadiabatic forces, which should be applicable to a wider range of systems beyond those we have studied here.

2.1. Superadiabatic free power functional

In section 1.9, we have given an introduction to power functional theory. Formally, PFT delivers the exact equation of motion for the one-body density field and current field. However, we need a good approximation for the superadiabatic functional $P_t^{\text{exc}}[\rho,\mathbf{J}]$. In the following section, we show how our proposed approximation is built, starting from functionals developed for a range of different physical systems.

2.1.1. Viscoelastic force

We already briefly discussed the nature of viscosity in section 1.6. In contrast, elasticity is the tendency of a deformed volume of matter to return to its previous shape. de las Heras and Schmidt presented a velocity gradient power functional which captures viscoelastic effects in Brownian dynamics [30]:

$$P_t^{\text{exc}}[\rho,\mathbf{J}] = \frac{1}{2}\int \mathrm{d}^3 r \left[\eta\,(\nabla\times\mathbf{v})^2 + \zeta\,(\nabla\cdot\mathbf{v})^2\right], \tag{2.1}$$

where $\mathbf{v}(\mathbf{r},t)$ is the velocity field, η is the dynamical shear viscosity, and ζ is the dynamical volume viscosity. In this simple form – without memory and assuming constant density profile – the functional recovers the Stokes form of hydrodynamics [4, 30]. The authors also presented a more general form with memory

$$\begin{aligned} P_t^{\text{visc}}[\rho,\mathbf{J}] = \frac{1}{2}\int \mathrm{d}^3 r \int \mathrm{d}^3 r' \int_0^t \mathrm{d}t'\,\rho(\mathbf{r},t)\Big[K_{\text{rot}}(\mathbf{r}-\mathbf{r}',t-t')(\nabla\times\mathbf{v}(\mathbf{r},t))\cdot(\nabla'\times\mathbf{v}(\mathbf{r}',t')) \\ + K_{\text{div}}(\mathbf{r}-\mathbf{r}',t-t')(\nabla\cdot\mathbf{v}(\mathbf{r},t))(\nabla'\cdot\mathbf{v}(\mathbf{r}',t'))\Big]\rho(\mathbf{r}',t'), \end{aligned} \tag{2.2}$$

where ∇ is the derivative with respect to $\mathbf{r}$, ∇' is the derivative with respect to $\mathbf{r}'$ and $K_a(\mathbf{r},t)$, with $a = \text{rot},\text{div}$, are memory kernels for the shear and volume viscosity, respectively. However, de las Heras and Schmidt did not specify a concrete for for the memory kernel. This formulation assumes that the system is in a well-defined state at time $t = 0$, such as an equilibrium state, which by definition does not depend on the state of the system at $t < 0$.

Using this functional (2.2), and choosing

$$K_{\mathrm{rot}}(\mathbf{r},t) = \eta K(\mathbf{r},t) \quad \text{and} \tag{2.3}$$

$$K_{\mathrm{div}}(\mathbf{r},t) = \zeta K(\mathbf{r},t), \tag{2.4}$$

we get superadiabatic forces of the form

$$\begin{aligned}\mathbf{f}_{\mathrm{sup}}(\mathbf{r},t) &= -\frac{\delta P_t^{\mathrm{visc}}[\rho,\mathbf{J}]}{\delta \mathbf{J}(\mathbf{r},t)} \\ &= -\frac{1}{2\rho(\mathbf{r},t)} \int \mathrm{d}^3 r' \int_0^t \mathrm{d}t' \left[\eta \nabla \times \left(\rho\rho' K \nabla' \times \mathbf{v}'\right) - \zeta \nabla \left(\rho\rho' K \nabla' \cdot \mathbf{v}'\right)\right],\end{aligned} \tag{2.5}$$

where $\rho = \rho(\mathbf{r},t)$, $\rho' = \rho(\mathbf{r}',t')$, $\mathbf{v}' = \mathbf{v}(\mathbf{r}',t')$ and $K = K(\mathbf{r}-\mathbf{r}', t-t')$. Notice how the functional derivative acts only on $\mathbf{J}(\mathbf{r},t)$ and not $\mathbf{J}(\mathbf{r}',t')$, although technically, $\mathbf{J}(\mathbf{r}',t)$ is still included in the integration $\int_0^t \mathrm{d}t'$. This is to strictly separate the trial current $\mathbf{J}(\mathbf{r},t)$ from the (fixed) history of the physical current $\mathbf{J}(\mathbf{r}',t')$. Mathematically expressed, we consider the functional as

$$P_t^{\mathrm{visc}}[\rho,\mathbf{J}] = \int \mathrm{d}^3 r \int \mathrm{d}^3 r' \lim_{\epsilon \to 0} \int_0^{t-\epsilon} \mathrm{d}t' [\cdots], \tag{2.6}$$

where ϵ is a small, positive number, such that the test current $J(r,t)$ at fixed t is not included in the integration over t'.

So far, we have not defined the memory kernel $K(\mathbf{r},t)$, which controls the effect of the system's history on the present force field. We consider three types of memory: The simplest form is with no memory at all, where

$$K_0(\mathbf{r},t) = \delta(t)\delta(\mathbf{r}), \tag{2.7}$$

such that $P_t^{\mathrm{visc}}[\rho,\mathbf{J}]$ is local in time and space.

The second type is space-local exponential memory

$$K_{\mathrm{L}}(\mathbf{r},t) = \frac{1}{\tau_{\mathrm{M}}} \exp\left(-\frac{t}{\tau_{\mathrm{M}}}\right) \delta(\mathbf{r}), \tag{2.8}$$

which is characterised by the memory time τ_{M}. Exponential memory is a simple and common approximation for memory. It has only the single free parameter τ_{M}, making

it easy to avoid overfitting of simulation data. Ex post, this choice is supported by the observation that the relaxation of the hard sphere fluid in response to a change in the external force is indeed close to an exponential decay [1].

The third type is a fully non-local memory kernel with a Gaussian form

$$K_{\mathrm{D}}(\mathbf{r},t)=\frac{\exp\left(-\mathbf{r}^2/(4D_{\mathrm{M}}t)-t/\tau_{\mathrm{M}}\right)}{(4\pi D_{\mathrm{M}}t)^{3/2}\tau_{\mathrm{M}}}, \tag{2.9}$$

where D_{M} is the memory diffusion constant, and τ_{M} is the memory time. The reasoning for this form is similar to that of the local exponential type above, in that it is simple and does not have a large amount of free parameters. Additionally, the expanding Gaussian has initially the form of a delta peak, which is then freely diffusing. Therefore, an interpretation of this form of memory would be that information about some observable at time $t' < t$ at point $\mathbf{r}'$ is propagated diffusively through the system. We name this memory kernel *diffusive memory*.

In the limit $t \to 0$, this memory kernel (2.9) reduces to

$$\lim_{t\to 0} K_{\mathrm{D}}(\mathbf{r},t)=\delta(\mathbf{r})/\tau_{\mathrm{M}}, \tag{2.10}$$

so only at $\Delta t > 0$ are there nonlocal interactions. We show in appendix D how the memory kernel K_{D} reduces in systems with planar or radial symmetry.

In our study of the hard sphere liquid under shear [1], we apply this functional with either the local exponential memory kernel K_{L} or the diffusive memory kernel K_{D}, to evaluate the accuracy of both variants. We determine that the diffusive memory kernel is much more accurate in the case of highly inhomogeneous shear rates.

In the study of the hard sphere van Hove function, we modify the functional slightly. The reasons are first that the current profile is radially symmetric in the time evolution of the van Hove function, the term $\nabla \times \mathbf{v}$ is zero. Additionally, we find that replacing the density $\rho(\mathbf{r})$ with the weighted density $n_3(\mathbf{r})$ (see section 1.7) in (2.2) results in a better fit with simulation data. We suspect that the reason for this is that the density profiles in the test particle limit are highly inhomogeneous, leading to local packing effects which are better captured by a weighted density (further improvements might be made using further weighted densities from fundamental measure theory). Thus,

we obtain

$$P_t^{\text{visc}}[\rho,\mathbf{J}] = \frac{\zeta}{2}\int \mathrm{d}^3 r \int \mathrm{d}^3 r' \int_0^t \mathrm{d}t' n_3(\mathbf{r},t)(\nabla\cdot\mathbf{v}(\mathbf{r},t))(\nabla'\cdot\mathbf{v}(\mathbf{r}',t'))n_3(\mathbf{r}',t')K_{\text{D}}(\mathbf{r}-\mathbf{r}',t-t'). \tag{2.11}$$

Based on our experience with the different memory kernels from the sheared fluid study, we decided to use the diffusive memory kernel exclusively in this study.

2.1.2. Drag force

A drag force arises in mixtures of particles if components move at different velocities. The drag force acts so as to minimise the velocity difference $\mathbf{v}_\Delta(\mathbf{r},t) = \mathbf{v}_1(\mathbf{r},t) - \mathbf{v}_2(\mathbf{r},t)$ between the velocities of the components 1 and 2 of the fluid. The functional form for these forces was proposed by Krinninger et al. in a study of motility-induced phase separation of active Brownian particles [98] and used by Geigenfeind et. al for a binary mixture of colloids with different buoyant masses [37]. The functional is without memory:

$$P_t^{\text{drag}}[\rho_1,\rho_2,\mathbf{v}_\Delta] = \frac{C_{\text{drag}}}{2}\int \mathrm{d}^3 r \rho_1(\mathbf{r},t)\rho_2(\mathbf{r},t)\mathbf{v}_\Delta^2(\mathbf{r},t), \tag{2.12}$$

where $\rho_1(\mathbf{r},t)$ and $\rho_2(\mathbf{r},t)$ are the density profiles of the two components of the fluid and C_{drag} is a scaling factor. In the case of the test particle limit, we select the test particle as component 1 ($\rho_1 = \rho_{\text{s}}$) and the other particles as component 2 ($\rho_2 = \rho_{\text{d}}$). In the study of the sheared fluid, this force does not contribute as there is only a single fluid component.

2.1.3. Structural force

A structural force is one which creates inhomogeneity – or *structure* – in the density profile of a nonequilibrium system [31]. It is a force of this type which drives migration effects in sheared systems [31]. Geigenfeind et al. found structural forces in their study of demixing of driven colloids [37], one of which we chose to extend in our study:

$$P_t^{\text{struc}}[\rho,\mathbf{J}] = -C_{\text{struc}}\int \mathrm{d}^3 r \rho^2(\mathbf{r})\mathbf{v}_\Delta^2(\mathbf{r})\nabla\cdot\mathbf{J}(\mathbf{r}). \tag{2.13}$$

In this form, the functional is local and has no memory. We adapted this functional to obtain the following superadiabatic power functional

$$P_t^{\text{struc}}[\rho,\mathbf{J}] = -C_{\text{struc}} \int \mathrm{d}^3 r \int \mathrm{d}^3 r' \int_0^t \mathrm{d}t' \, (\nabla \cdot \mathbf{J}(\mathbf{r},t))\, n_3^2(\mathbf{r}',t') \mathbf{v}^2(\mathbf{r}',t') K_{\text{D}}(\mathbf{r}-\mathbf{r}', t-t'). \tag{2.14}$$

Notably, we changed from a memory-free expression to a form which includes memory, where the current is evaluated in the present, and velocity and the weighted density $n_3(\mathbf{r},t)$ are evaluated in the past. We switched from the differential velocity $\mathbf{v}_\Delta(\mathbf{r},t)$ to the total velocity profile $\mathbf{v}(\mathbf{r},t)$, as the self velocity component is numerically hard to determine in regions where $\rho_{\text{s}}(\mathbf{r},t)$ is very small. We chose here the diffusive memory kernel from above, as experience in our study of the sheared hard sphere fluid showed that this form is much more accurate than local memory. Additionally, we replaced the local density $\rho(\mathbf{r},t)$ with the weighted density $n_3(\mathbf{r},t)$. We use this functional (2.14) in our study of the van Hove function.

2.2. Viscoelastic effects in a sheared hard sphere fluid

In [1], we study the dynamics of the hard sphere fluid under shear using event-driven Brownian dynamics simulation and power functional theory with the viscoelastic power functional $P_t^{\text{visc}}[\rho,\mathbf{J}]$ (2.11). We examine a system of hard spheres at volume fraction $\eta \approx 0.38$, which is assumed to be homogeneous in the y-z-plane and periodic in the x direction. We subject the system to a square wave shear force field in z direction with a period of 5σ – where σ is the diameter of a particle – and an amplitude of $5\mathrm{k_B}T/\sigma$, given by

$$\mathbf{f}_{\text{ext}}(\mathbf{r}) = 5\frac{\mathrm{k_B}T}{\sigma} \operatorname{sgn}\left(\sin\left(\frac{2\pi x}{5\sigma}\right)\right)\hat{\mathbf{e}}_z, \tag{2.15}$$

where $\operatorname{sgn}(\cdot)$ is the signum function. We examine the following temporal sequence:

- The system is in equilibrium, no external force is present.
- The external shear force is switched on instantaneously. As a result, the current profile of the system changes over time.

- The system settles into a steady state after a time of about 0.1τ. In steady state, the current profile is constant over time.
- The external shear force is switched off. The current profile relaxes until equilibrium is reached again.

We obtain density and current profiles during all of these phases using BD simulation and compare these profiles to theoretical results.

Remarkably, we observe that the transition from the equilibrium current profile into the steady state current profile is nonmonotonic. The system first responds with a current profile which is larger in magnitude than the steady state current profile. Then, the current profile decays roughly exponentially until steady state is reached. The density profile evolves as well, developing small density fluctuations near regions of high shear rate (see fig. 2.1).

The transition from steady state back to equilibrium again shows an overcorrection of the current profile for the change in force. This results in a global reversal of the direction of the current profile after the shear force is switched off (see fig. 2.2). To our knowledge, this is the first report of such an effect in driven Brownian fluids and shows that the hard sphere fluid has viscoelasticity.

2.2.1. Nonlocal Memory

We calculate the steady state current profile of the system with PFT, using the same external forces as applied in simulation. We use the viscoelastic power function $P_t^{\text{visc}}[\rho,\mathbf{J}]$ to approximate the superadiabatic forces. Although structural forces should play a role in this situation, as we can see by inhomogeneities in the density profile, we did not yet have a suitable candidate functional at the time of this study. We decided to simplify our approach by imposing the inhomogeneous density profile observed in BD simulation via an external potential in the PFT calculations. We study the differences between forces calculated with the local memory kernel K_{L} (eg. (2.8)) and with the diffusive memory kernel K_{D}. We tune the free parameters in the viscoelastic power functional $P_t^{\text{visc}}[\rho,\mathbf{J}]$ to minimise the difference between the PFT current profile and the BD current profile. Thereby we determine the memory diffusion constant $D_{\text{M}} \approx 5.6\sigma^2/\tau$ and the memory time $\tau_{\text{M}} \approx 0.02\tau$. With these parameters, we find good

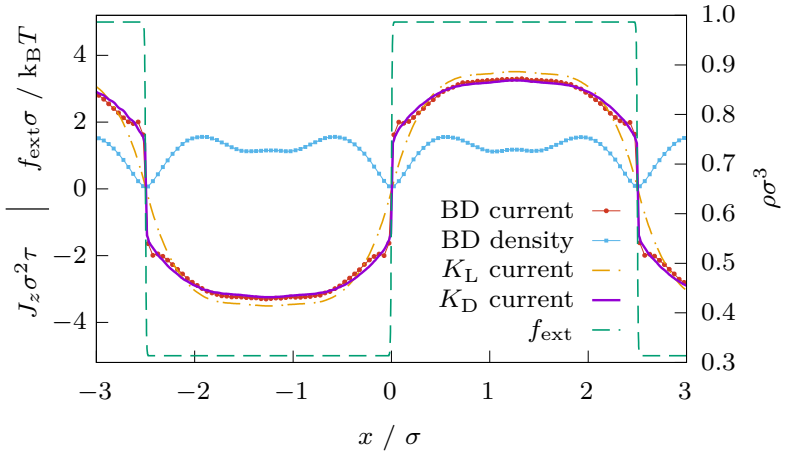

Figure 2.1.: Steady state current profile J_z and density profile ρ for a system of hard spheres in steady state under the influence of external force f_{ext}. Measurements from BD simulation (solid line with circles/squares) in comparison with current profiles calculated using PFT with a local memory kernel (yellow dash-dotted line) and a diffusive memory kernel (solid purple line). Reproduction of a figure from [1].

quantitative agreement between BD simulation and PFT with the viscoelastic power functional with diffusive memory (see fig. 2.1). The same functional with space-local exponential memory shows significant and qualitative deviations. This is especially prominent in regions of high shear rate, where the viscoelastic functional with local memory predicts a smooth transition in the current, whereas with diffusive memory, the observed discontinuity in the current profile is reproduced. In steady state, the time behaviour of the memory kernel is irrelevant, as both current profile and density profile are constant in time. Any space-local memory kernel used in our viscoelastic functional must therefore show the same defects and no improvement is possible by changing the temporal behaviour of the kernel. Hence, a non-local memory kernel, like the presented diffusive memory (2.9), is needed to adequately describe the observed viscoelastic effects.

2.2.2. Motion Reversal

As mentioned above, we observe that the change of the current profile from equilibrium to steady state and from steady state to equilibrium is non-monotonic. In the case of

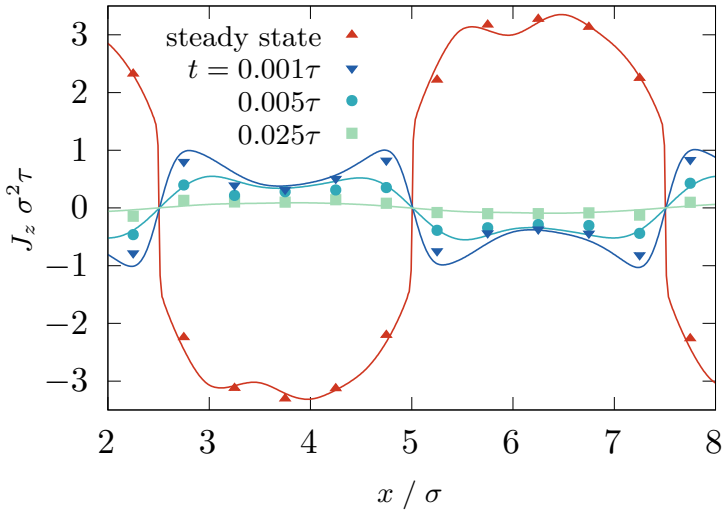

Figure 2.2.: Current profile J_z in steady state (red upwards triangle) and at different times t after the driving force has been switched off. Data from BD simulation (symbols) and PFT (solid lines) with diffusive memory taken from [1].

going from equilibrium to steady shear, this manifests itself as an immediate super-steady current[1] after switching on the driving force, which is then dampened by viscous forces. The effect is more surprising when going from steady state back to equilibrium: The current profile first over-corrects for the change in the driving force, resulting in a reversal of the direction of the current. This surprising observation is easily explained using PFT. The onset of viscous forces, which slow the current profile, is delayed because it is mediated by memory. Hence, the initial current profile after switch-on of the shear force is larger than in steady state, when the viscous slowdown is in full effect. The current reversal after switch-off of the shear force is a consequence of the same memory: Once the driving force is gone, the previously slowing force now drives a reverse current until the steady state current has been forgotten. This is an example of the power of PFT to not only reproduce simulation data with high accuracy, but to identify and explain physical effects in many-body dynamics.

[1] That is, a current that is greater in magnitude than the steady state current.

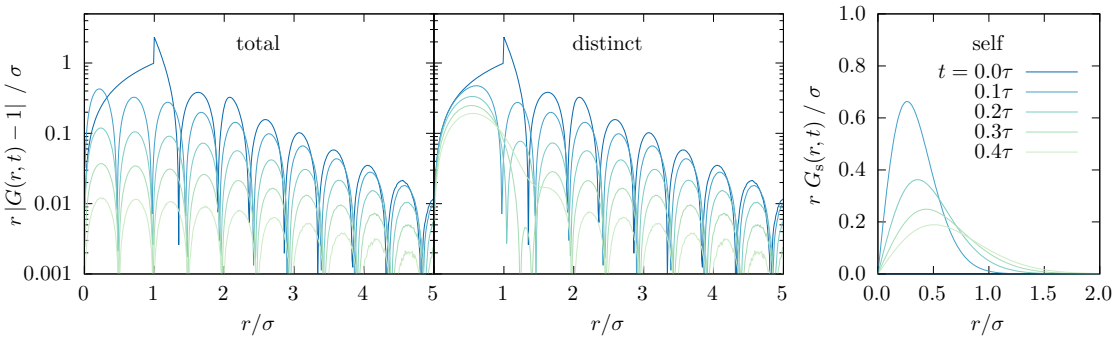

Figure 2.3.: Dynamic decay of the total, distinct, and self van Hove function $G(r,t)$. The total and distinct values are plotted as the logarithmic deviation from the long-range limit to better visualise the shell decay. Data from [3].

2.3. Superadiabatic forces in equilibrium two-body dynamics

The subject of the second study is the bulk van Hove function of the hard sphere fluid. This subject is of special interest because it is not dependent on external driving forces, but encapsulates the innate dynamics of the hard sphere liquid in equilibrium. The current profile and density profile of the test particle fluid are both highly inhomogeneous and complex, as previous studies of the hard sphere van Hove function have shown [49, 60, 61]. A study by Schindler and Schmidt of the forces of the van Hove function of the Lennard-Jones fluid shows that superadiabatic forces are highly relevant in the time evolution of the van Hove function [99], which accounts for the shortcomings of previous attempts to describe the dynamics of the van Hove function within DDFT [49, 60, 61]. Stopper et al. made progress on this front by extending DDFT with a local particle mobility term [61]. Based on our experience with the viscoelastic power functional in the sheared fluid, we hope to find forces which account for the observed local reduction in particle mobility.

2.3.1. Dynamic decay of the van Hove function

We use BD simulation to calculate the van Hove function for an equilibrium hard sphere fluid at volume fraction ≈ 0.35. We analyse the dynamic decay of the van Hove function, in particular on a logarithmic scale (see fig. 2.3), and compare with results

from a study of a Lennard-Jones fluid [99]. We find that the process is qualitatively similar in both systems. For time $t = 0$, the self van Hove function is a delta peak located at $r = 0$, since the test particle is confined at the origin. The distinct van Hove function is zero from $r = 0$ to $r = \sigma$ because the presence of the test particle prevents any other particles from entering that volume. For $r > \sigma$, the particles are arranged in concentric shells around the inner test particle. This is reflected in the distinct van Hove function as a series of maxima and minima at regular intervals with an exponentially decaying envelope.

The dynamic decay of the van Hove function is composed of two effects: As the self particle diffuses out of its initial position, the shells loose confinement, starting from the ones closest to the origin. The exponential envelope then has two regions, where the decay length inside the inner region increases with time, but the outer decay length remains stable. The border between these different regions of decay propagates outward.

Whereas the first effect (propagating deconfinement of shells) is visible in the decay of the total van Hove function, the second effect is only apparent if looking at the distinct van Hove function: As confinement due to the self particle slowly vanishes, distinct particles drift into the initial void at $r \leq \sigma$. This minimum „swallows“ the inner shells of the distinct van Hove function in an expanding region of monotonic decay. Additionally, a slow outward drift of the shells is visible in the simulation data.

We later see that looking at the total van Hove function in addition to the self and distinct components allows for a better separation of different physical effects in the dynamic decay of the van Hove function. For a complete understanding, the total view as well as the labelled view of the system are necessary.

2.3.2. Vineyard Approximation

One early attempt at a theoretical approximation for the van Hove function was presented by Vineyard [4, 100]. He proposed that the distinct van Hove function at time t should be approximately equal to the convolution between the static radial distribution function $g(r)$ and the self van Hove function at time t. We used our BD simulation data to check the accuracy of this approximation and found that it significantly overestimates the rate of decay of the outer shells of the distinct van

Hove function. The first minimum of $G_{\mathrm{d}}(r,t)$ is, however, well represented. We present details for our implementation of the numerical convolution of two spherically symmetric functions in appendix E.2.

2.3.3. Comparison with DDFT

We calculate the van Hove function using DDFT with three different excess free energy functionals to evaluate the accuracy of different methods to account for the special role of the self density of the test particle. The baseline is the uncorrected tensorial White Bear Mk. II functional [19], where $F_{\mathrm{exc}}[\rho_s,\rho_d]=F_{\mathrm{exc}}[\rho_s+\rho_d]$. Against this baseline we compare the partially linearised functional [60] and the quenched functional [61]. We find that the partially linearised excess free energy functional produces major qualitative deviations from the decay observed in BD and should therefore not be used. The differences between the quenched excess free energy functional and the uncorrected functional which are visible in the decay of the van Hove function are minor. Qualitatively, both functionals reproduce the decay mechanisms observed in simulation. However, the time scale of the decay is in all three cases too fast compared with BD simulation. This problem is well-known for DDFT [25] and has been found in other DDFT studies of the van Hove function [60, 61].

2.3.4. Adiabatic Forces

From the BD simulation data, we extract the species-resolved (self and distinct) current and internal force field in the dynamic test particle picture [48, 54]. To determine whether the overly quick decay in DDFT arises in this case purely due to missing superadiabatic forces, or also because of deviations of the adiabatic forces, we use Metropolis Monte Carlo simulations (MC) to obtain independent data for the adiabatic forces acting in the dynamic decay of the van Hove function. We do this with an inversion method („custom flow“) presented by de las Heras et al. [101]. For given target density profiles at fixed time t $\rho_{\mathrm{s}}^t(\mathbf{r})=\rho_{\mathrm{B}}G_{\mathrm{s}}(\mathbf{r},t)$, $\rho_{\mathrm{d}}^t(\mathbf{r})=\rho_{\mathrm{B}}G_{\mathrm{d}}(\mathbf{r},t)$, trial adiabatic potentials $V_{\mathrm{ad,s}}^t(\mathbf{r})$ (acting on the self component), $V_{\mathrm{ad,d}}^t(\mathbf{r})$ (acting on the distinct component) are chosen and the resulting equilibrium density profile of both fluid components is sampled using MC. The sampled profiles are then compared to the target density profiles. Where the sampled density profile is larger in magnitude

than the target, the corresponding potential is increased. Where the sampled density profile is lower in magnitude than the target, the corresponding potential is decreased. This process is repeated until the sampled density profile is very close to the target density profile.

We compare the gradient of the thus determined adiabatic potentials to the forces calculated using the different excess free energy functionals. We find that the quenched excess free energy functional [61] is a significant improvement over the uncorrected free energy functional. However, significant differences remain in comparison to BD simulation data for the adiabatic force field, especially on long time scales.

2.3.5. Total and Differential Forces

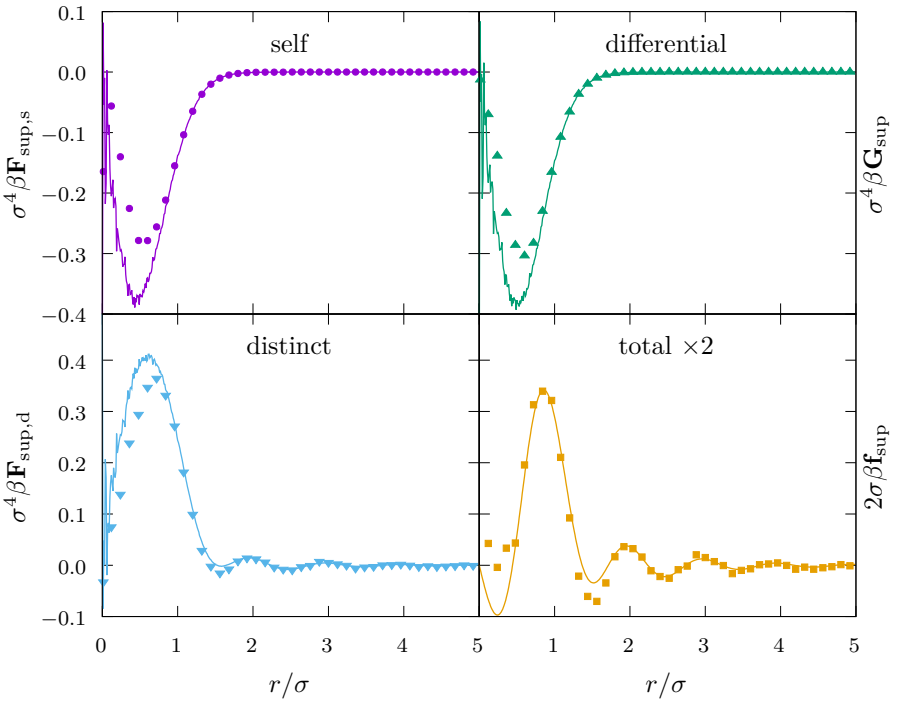

Figure 2.4.: Superadiabatic self ($\mathbf{F}_{\mathrm{sup,s}}$), distinct ($\mathbf{F}_{\mathrm{sup,d}}$) and differential ($\mathbf{G}_{\mathrm{sup}}$) force density and total force field ($\mathbf{f}_{\mathrm{sup}}$) in the time evolution of the van Hove function at time $t = 0.3\tau$. BD/MC simulation data (symbols) are shown in comparison with PFT results (lines). Data is taken from [2, 3].

We use the adiabatic force field calculated with MC to split the internal force field from BD simulation into its adiabatic and superadiabatic parts. The observed forces are quite complex, as is expected for a highly structured object like the van Hove function. We have found when analysing the van Hove function, that the effects that contribute to the dynamic decay are easier understood if looking at the total, self, and distinct components instead of just the self and distinct components. Thus, we analyse not only the forces acting on the self and distinct density components, but additionally study the total force field $\mathbf{f}(\mathbf{r},t)$ and the differential force density $\mathbf{G}(\mathbf{r},t)$. These two additional components can be calculated via a transformation that was proposed by Geigenfeind et al. in their study of a driven binary mixture [37]. By applying their transformation in the dynamic test particle case, we obtain

$$\mathbf{f}(\mathbf{r},t) = \frac{1}{\rho(\mathbf{r},t)}\left(\mathbf{F}_\mathrm{s}(\mathbf{r},t)+\mathbf{F}_\mathrm{d}(\mathbf{r},t)\right) \quad \text{and} \tag{2.16}$$

$$\mathbf{G}(\mathbf{r},t) = \frac{\rho_\mathrm{d}(\mathbf{r},t)}{\rho(\mathbf{r},t)}\mathbf{F}_\mathrm{s}(\mathbf{r},t) - \frac{\rho_\mathrm{s}(\mathbf{r},t)}{\rho(\mathbf{r},t)}\mathbf{F}_\mathrm{d}(\mathbf{r},t), \tag{2.17}$$

where $\mathbf{F}_\mathrm{s}(\mathbf{r},t)$ and $\mathbf{F}_\mathrm{d}(\mathbf{r},t)$ are the force densities acting on the self density component and the distinct density component, respectively. Figure 2.4 shows an example result of this transformation. We can see that the differential force density consists only of a single peak, while the total force is oscillatory. This decomposition of the internal force field is far less apparent in the distinct-self splitting.

2.3.6. Superadiabatic free power functional approximation

With density profiles and current profiles from BD simulation as input, we use our approximate superadiabatic power functional, consisting of the drag, viscoelastic, and structural contributions, to calculate superadiabatic forces, and compare these results to the forces determined in simulation. We tune the free parameters in the functional to minimise the difference between the forces measured in BD and those calculated with PFT. Here, the splitting into total force and differential force density helps us immensely, as the drag component acts only differentially and has no contribution to the total force, while the viscoelastic and structural forces contribute only to the total force. The resulting parameters are given in table 2.1. For the viscoelastic power functional, we apply the parameters we have already determined in the previous study [1]. It is

Table 2.1.: Parameters of the drag, viscoelastic, and structural power functionals, determined by least squares fit to superadiabatic force profiles obtained from BD simulations.

	Prefactor	Memory time	Memory diffusion constant
P_t^{drag}	$C_{\text{drag}} \approx 2.2 \mathrm{k_B} T \tau \sigma$	–	–
P_t^{visc}	$\zeta \approx 5.8 \mathrm{k_B} T \tau^{-1} \sigma^{-3}$	$\tau_{\text{M}} \approx 0.02\tau$	$D_{\text{M}} \approx 5.6\sigma^2\tau^{-1}$
P_t^{struc}	$C_{\text{struc}} \approx 0.42 \mathrm{k_B} T \tau^2 \sigma^{-2}$	$\tau_{\text{M}} \approx 0.8\tau$	$D_{\text{M}} \approx 0.25\sigma^2\tau^{-1}$

notable that the memory time for the structural force is 0.8τ, a factor of 40 higher than the memory time of the viscoelastic force. This makes the structural force surprisingly long-lived compared to the viscoelastic forces. For long times $t > \tau$, the superadiabatic force profile is dominated by the drag force. This allows us to determine a relation between the drag strength C_{drag} and the long-time self diffusion constant associated with G_{s}

$$D_{\text{L}} = \frac{\mathrm{k_B} T}{\gamma + C_{\text{drag}} \rho_{\text{B}}}. \tag{2.18}$$

The approximations which lead to this result and a derivation of the formula (2.18) are given in [3]. This modified Einstein relation predicts in our case $D_{\text{L}} \approx 0.38\sigma^2/\tau$, which is roughly consistent with the diffusion coefficient observed in BD simulation $D_{\text{L}} \approx 0.32\sigma^2/\tau$ [3]. A fit only to the latest available simulation time step improves the theoretical result to $D_{\text{L}} \approx 0.36\sigma^2/\tau$.

Our approximation has good quantitative accuracy on long time scales ($t > 0.3\tau$), but significant deviations remain at short time scales. Figure 2.4 shows an example of reasonable accuracy at an intermediate time $t = 0.3\tau$. The deviations at short times are unsurprising, as the velocity profiles and inhomogeneities in the density profile are extreme. Functionals which produce the missing forces are likely of higher order in velocity, whereas our drag and viscoelastic functionals are second order in velocity, and the structural functional is third order in velocity.

Even though the construction of PFT ensures that the superadiabatic power functional is in principle independent of the external forces (see (1.40)), it is perhaps surprising that functionals which were initially developed for specific applications in sheared fluids [1] or driven colloids [37] are also applicable in the case of the van Hove function.

This suggests some amount of universality of the presented approximation, which can therefore likely be applied to a larger range of systems.

3. Conclusions and outlook

In this thesis, we investigated the dynamic behaviour of the hard sphere fluid under shear and (on the two-body level) in the quiescent bulk, using the framework of power functional theory combined with MC and BD simulation techniques to provide quasi-exact benchmark results. We focused on the development of a superadiabatic power functional for hard spheres, which is applicable to as wide a range of situations as possible. Superadiabatic forces depend in general non-locally on the current profile and density profile as a function of time. Therefore, finding an appropriate memory kernel, which approximates the dependence of the instantaneous forces on the history of the system, has been a central objective of the thesis.

In a study of a Brownian hard sphere fluid under the influence of an inhomogeneous shear force [1], we developed a viscoelastic power functional which includes memory effects. We evaluated the accuracy of a spatially local memory kernel and of a non-local diffusive memory kernel by comparing current profiles obtained with BD simulation with current profiles calculated using PFT. We found that a spatially local memory approximation is insufficient to describe viscoelastic forces in inhomogeneous shear profiles. The diffusive memory approximation, however, produced very accurate viscoelastic forces. In addition to providing a good approximation for viscoelastic forces, we found that those forces drive a reverse current, opposite to the driving direction, when the driving shear force is switched off. This effect is caused by a viscoelastic force field, which is dependent on memory of the steady state current profile before switching.

We then amended the viscoelastic superadiabatic power functional with both a drag contribution and a structural contribution [2, 3]. Both added terms were developed previously for very different systems, by Krinninger et al. in a study of active Brownian particles [98], and by Geigenfeind et al. in a study of a driven binary mixture of colloids [37]. We showed that these force components can be applied in a much more general context, as would be expected from the building principles of PFT. We replaced

the density variable in the viscoelastic functional and the structural functional with the weighted density n_3 to capture local packing effects, and the structural functional was extended to include non-local memory as developed previously for the viscoelastic component. We used Brownian dynamics simulation to obtain the internal force field acting during the time evolution of the bulk hard sphere van Hove function in the dynamic test particle picture. With the help of Metropolis Monte Carlo simulations, we split this internal force field into its adiabatic and superadiabatic components.

Our analysis of the adiabatic forces included a comparison to three different approximations for adiabatic forces presented by Stopper et al. [60, 61]. We found that the quenched functional approach proposed in these reports is a significant improvement over previously available approximations. However, some deviations remain when comparing the resulting forces to simulation results. Additionally, the superadiabatic forces are of significant magnitude and dominate the internal force field at long timescales. Therefore, superadiabatic forces cannot be neglected in an accurate description of the dynamics of the van Hove function.

We then tested our superadiabatic power functional approximation against the results for superadiabatic forces from simulations. We found that, except on short time scales, our approximation has good quantitative accuracy. The long-time self diffusion constant determined using our approximation is roughly consistent with the one observed in simulation. The fact that this is the case despite the components of our approximation being developed for different applications points to universality of the presented approximation. We conclude that these drag, structural and viscoelastic forces are fundamental phenomena acting in the dynamics of the hard sphere fluid, and likely in other liquids with steeply repulsive interparticle interactions as well.

Further development of our approach is thus warranted, to hopefully achieve the same level of accuracy in the description of nonequilibrium systems as classical DFT has in the description of equilibrium systems. An obvious avenue for future development is the improvement of the description of packing effects in highly inhomogeneous systems, as this is an area where the approximation in its current state fails. Fundamental measure theory provides candidate weighted densities which could be applied to achieve this. Additionally, the rather simple diffusive memory kernel used here could be improved with more sophisticated temporal and spatial components. Previous work on complex memory in molecular dynamics [102, 103] could provide guidelines for this direction

of development.

4. References

1. Treffenstädt, L. L. & Schmidt, M. „Memory-induced motion reversal in Brownian liquids“. *Soft Matter* **16,** 1518 (2020).
2. Treffenstädt, L. L. & Schmidt, M. „Universality in Driven and Equilibrium Hard Sphere Liquid Dynamics“. *Phys. Rev. Lett.* **126,** 058002 (2021).
3. Treffenstädt, L. L., Schindler, T. & Schmidt, M. „Dynamic Decay and Superadiabatic Forces in the van Hove Dynamics of Bulk Hard Sphere Fluids“. *SciPost Physics.* submitted. https://scipost.org/submission/2201.06099v1 (2022).
4. Hansen, J.-P. & McDonald, I. R. *Theory of Simple Liquids* 4th ed. ISBN: 978-0-12-387032-2 (Academic Press, Oxford, 2013).
5. Zwanzig, R. *Nonequilibrium statistical mechanics* (Oxford University Press, 2001).
6. Ebner, C., Lee, M. A. & Saam, W. F. „Nonuniform one-dimensional classical fluids: Theory versus Monte Carlo experiments“. *Phys. Rev. A* **21,** 959 (1980).
7. Kaplow, R., Strong, S. L. & Averbach, B. L. „Radial Density Functions for Liquid Mercury and Lead“. *Phys. Rev.* **138,** A1336 (1965).
8. Dyre, J. C. „Simple liquids' quasiuniversality and the hard-sphere paradigm“. *J. Phys.: Condens. Matter* **28,** 323001 (2016).
9. Smith, E. B. & Alder, B. J. „Perturbation Calculations in Equilibrium Statistical Mechanics. I. Hard Sphere Basis Potential“. *J. Chem. Phys.* **30,** 1190 (1959).
10. Ascarelli, P. „Velocity of Sound and Compressibility in Liquid Metals“. *Phys. Rev.* **173,** 271 (1968).
11. Ascarelli, P. & Harrison, R. J. „Density-Dependent Potentials and the Hard-Sphere Model for Liquid Metals“. *Phys. Rev. Lett.* **22,** 385 (1969).
12. Vrij, A. *et al.* „Light scattering of colloidal dispersions in non-polar solvents at finite concentrations. Silica spheres as model particles for hard-sphere interactions“. *Faraday Disc. Chem. Soc.* **76,** 19 (1983).
13. Kirkwood, J. G. „Statistical Mechanics of Fluid Mixtures“. *J. Chem. Phys.* **3,** 300 (1935).
14. Percus, J. K. & Yevick, G. J. „Analysis of Classical Statistical Mechanics by Means of Collective Coordinates“. *Phys. Rev.* **110,** 1 (1958).

15. Carnahan, N. F. & Starling, K. E. „Thermodynamic Properties of a Rigid-Sphere Fluid“. *J. Chem. Phys.* **53,** 600 (1970).

16. Mermin, N. D. „Thermal Properties of the Inhomogeneous Electron Gas“. *Phys. Rev.* **137,** A1441 (1965).

17. Evans, R. „The nature of the liquid-vapour interface and other topics in the statistical mechanics of non-uniform, classical fluids“. *Adv. Phys.* **28,** 143 (1979).

18. Rosenfeld, Y. „Free-energy model for the inhomogeneous hard-sphere fluid mixture and density-functional theory of freezing“. *Phys. Rev. Lett.* **63,** 980 (1989).

19. Roth, R. „Fundamental measure theory for hard-sphere mixtures: a review“. *J. Phys.: Condens. Matter* **22,** 063102 (2010).

20. Percus, J. K. „Equilibrium state of a classical fluid of hard rods in an external field“. *J. Stat. Phys.* **15,** 505 (1976).

21. Robledo, A. & Varea, C. „On the relationship between the density functional formalism and the potential distribution theory for nonuniform fluids“. *J. Stat. Phys.* **26,** 513 (1981).

22. Rosenfeld, Y., Schmidt, M., Löwen, H. & Tarazona, P. „Fundamental-measure free-energy density functional for hard spheres: Dimensional crossover and freezing“. *Phys. Rev. E* **55,** 4245 (1997).

23. Tarazona, P. „Density Functional for Hard Sphere Crystals: A Fundamental Measure Approach“. *Phys. Rev. Lett.* **84,** 694 (2000).

24. Roth, R., Evans, R., Lang, A. & Kahl, G. „Fundamental measure theory for hard-sphere mixtures revisited: the White Bear version“. *J. Phys.: Condens. Matter* **14,** 12063 (2002).

25. Marconi, U. M. B. & Tarazona, P. „Dynamic density functional theory of fluids“. *J. Chem. Phys.* **110,** 8032 (1999).

26. Marconi, U. M. B. & Tarazona, P. „Dynamic density functional theory of fluids“. *J. Phys.: Condens. Matter* **12,** A413 (2000).

27. Archer, A. J. & Evans, R. „Dynamical density functional theory and its application to spinodal decomposition“. *J. Chem. Phys.* **121,** 4246 (2004).

28. Schmidt, M. & Brader, J. M. „Power functional theory for Brownian dynamics“. *J. Chem. Phys.* **138,** 214101 (2013).

29. Bernreuther, E. & Schmidt, M. „Superadiabatic forces in the dynamics of the one-dimensional Gaussian core model“. *Phys. Rev. E* **94,** 022105 (2016).

30. de las Heras, D. & Schmidt, M. „Velocity Gradient Power Functional for Brownian Dynamics“. *Phys. Rev. Lett.* **120,** 028001 (2018).

31. Stuhlmüller, N. C. X., Eckert, T., de las Heras, D. & Schmidt, M. „Structural Nonequilibrium Forces in Driven Colloidal Systems“. *Phys. Rev. Lett.* **121,** 098002 (2018).

32. de las Heras, D. & Schmidt, M. „Flow and Structure in Nonequilibrium Brownian Many-Body Systems“. *Phys. Rev. Lett.* **125,** 018001 (2020).

33. Krinninger, P. & Schmidt, M. „Power functional theory for active Brownian particles: General formulation and power sum rules“. *J. Chem. Phys.* **150,** 074112 (2019).

34. Hermann, S., Krinninger, P., de las Heras, D. & Schmidt, M. „Phase coexistence of active Brownian particles“. *Phys. Rev. E* **100,** 052604 (2019).

35. Hermann, S., de las Heras, D. & Schmidt, M. „Non-negative Interfacial Tension in Phase-Separated Active Brownian Particles“. *Phys. Rev. Lett.* **123,** 268002 (2019).

36. Hermann, S., de las Heras, D. & Schmidt, M. „Phase separation of active Brownian particles in two dimensions: anything for a quiet life“. *Molecular Physics* **119,** e1902585 (2021).

37. Geigenfeind, T., de las Heras, D. & Schmidt, M. „Superadiabatic demixing in nonequilibrium colloids“. *Commun. Phys.* **3,** 23 (2020).

38. Cichocki, B. & Hinsen, K. „Dynamic computer simulation of concentrated hard sphere suspensions: I. Simulation technique and mean square displacement data“. *Physica A* **166,** 473 (1990).

39. Schaertl, W. & Sillescu, H. „Brownian dynamics simulations of colloidal hard spheres. Effects of sample dimensionality on self-diffusion“. *J. Stat. Phys.* **74,** 687 (1994).

40. Strating, P. „Brownian dynamics simulation of a hard-sphere suspension“. *Phys. Rev. E* **59,** 2175 (1999).

41. Scala, A., Voigtmann, T. & De Michele, C. „Event-driven Brownian dynamics for hard spheres“. *J. Chem. Phys.* **126,** 134109 (2007).

42. Leitmann, S., Mandal, S., Fuchs, M., Puertas, A. M. & Franosch, T. „Time-dependent active microrheology in dilute colloidal suspensions“. *Phys. Rev. Fluids* **3,** 103301 (2018).

43. Mandal, S., Schrack, L., Löwen, H., Sperl, M. & Franosch, T. „Persistent Anti-Correlations in Brownian Dynamics Simulations of Dense Colloidal Suspensions Revealed by Noise Suppression“. *Phys. Rev. Lett.* **123,** 168001 (2019).

44. Voigtmann, T. *et al.* „Rheology of colloidal and metallic glass formers“. *Colloid Polym. Sci.* **298,** 681 (2020).

45. Jung, G., Schrack, L. & Franosch, T. „Tagged-particle dynamics in confined colloidal liquids“. *Phys. Rev. E* **102,** 032611 (2020).

46. Metropolis, N., Rosenbluth, A. W., Rosenbluth, M. N., Teller, A. H. & Teller, E. „Equation of State Calculations by Fast Computing Machines“. *J. Chem. Phys.* **21,** 1087 (1953).

47. Hastings, W. K. „Monte Carlo sampling methods using Markov chains and their applications“. *Biometrika* **57,** 97 (1970).

48. Archer, A. J., Hopkins, P. & Schmidt, M. „Dynamics in inhomogeneous liquids and glasses via the test particle limit“. *Phys. Rev. E* **75,** 040501 (2007).

49. Hopkins, P., Fortini, A., Archer, A. J. & Schmidt, M. „The van Hove distribution function for Brownian hard spheres: Dynamical test particle theory and computer simulations for bulk dynamics“. *J. Chem. Phys.* **133,** 224505 (2010).

50. Van Hove, L. „Correlations in Space and Time and Born Approximation Scattering in Systems of Interacting Particles“. *Phys. Rev.* **95,** 249 (1954).

51. Ornstein, L. S. „Accidental deviations of density and opalescence at the critical point of a single substance“. *Proc. Akad. Sci.* **17** (1914).

52. Brader, J. M. & Schmidt, M. „Nonequilibrium Ornstein-Zernike relation for Brownian many-body dynamics“. *J. Chem. Phys.* **139,** 104108 (2013).

53. Percus, J. K. „Approximation Methods in Classical Statistical Mechanics“. *Phys. Rev. Lett.* **8,** 462 (1962).

54. Brader, J. M. & Schmidt, M. „Power functional theory for the dynamic test particle limit“. *J. Phys.: Condens. Matter* **27,** 194106 (2015).

55. Voigtmann, T., Puertas, A. M. & Fuchs, M. „Tagged-particle dynamics in a hard-sphere system: Mode-coupling theory analysis“. *Phys. Rev. E* **70,** 061506 (2004).

56. Van Megen, W. & Underwood, S. M. „Glass transition in colloidal hard spheres: Mode-coupling theory analysis“. *Phys. Rev. Lett.* **70,** 2766 (1993).

57. Van Megen, W. & Underwood, S. M. „Glass transition in colloidal hard spheres: Measurement and mode-coupling-theory analysis of the coherent intermediate scattering function“. *Phys. Rev. E* **49,** 4206 (1994).

58. Gibbs, J. H. & DiMarzio, E. A. „Nature of the Glass Transition and the Glassy State“. *J. Chem. Phys.* **28,** 373 (1958).

59. Ramakrishnan, T. V. & Yussouff, M. „First-principles order-parameter theory of freezing“. *Phys. Rev. B* **19,** 2775 (1979).

60. Stopper, D., Marolt, K., Roth, R. & Hansen-Goos, H. „Modeling diffusion in colloidal suspensions by dynamical density functional theory using fundamental measure theory of hard spheres“. *Phys. Rev. E* **92,** 022151 (2015).

61. Stopper, D., Roth, R. & Hansen-Goos, H. „Communication: Dynamical density functional theory for dense suspensions of colloidal hard spheres“. *J. Chem. Phys.* **143,** 181105 (2015).

62. Hansen-Goos, H. & Roth, R. „Density functional theory for hard-sphere mixtures: the White Bear version mark II“. *J. Phys.: Condens. Matter* **18,** 8413 (2006).

63. Alder, B. J., Gass, D. M. & Wainwright, T. E. „Studies in Molecular Dynamics. VIII. The Transport Coefficients for a Hard-Sphere Fluid“. *J. Chem. Phys.* **53,** 3813 (1970).

64. Naitoh, T. & Ono, S. „The shear viscosity of a hard-sphere fluid via nonequilibrium molecular dynamics“. *J. Chem. Phys.* **70,** 4515 (1979).

65. Erpenbeck, J. J. & Wood, W. W. „Molecular dynamics calculations of shear viscosity time-correlation functions for hard spheres“. *J. Stat. Phys.* **24,** 455 (1981).

66. Erpenbeck, J. J. „Shear Viscosity of the Hard-Sphere Fluid via Nonequilibrium Molecular Dynamics“. *Phys. Rev. Lett.* **52,** 1333 (1984).

67. Erpenbeck, J. J. & Wood, W. W. „Self-diffusion coefficient for the hard-sphere fluid“. *Phys. Rev. A* **43,** 4254 (1991).

68. Sigurgeirsson, H. & Heyes, D. M. „Transport coefficients of hard sphere fluids“. *Mol. Phys.* **101,** 469 (2003).

69. Evans, D. J. & Morriss, G. P. „Shear Thickening and Turbulence in Simple Fluids“. *Phys. Rev. Lett.* **56,** 2172 (1986).

70. Leighton, D. & Acrivos, A. „The shear-induced migration of particles in concentrated suspensions“. *J. Fluid Mech.* **181,** 415 (1987).

71. Chakrabarti, J., Dzubiella, J. & Löwen, H. „Reentrance effect in the lane formation of driven colloids“. *Phys. Rev. E* **70,** 012401 (2004).

72. Wächtler, C. W., Kogler, F. & Klapp, S. H. L. „Lane formation in a driven attractive fluid“. *Phys. Rev. E* **94,** 052603 (2016).

73. Dhont, J. K. G. „A constitutive relation describing the shear-banding transition“. *Phys. Rev. E* **60,** 4534 (1999).

74. Dhont, J. K. G. *et al.* „Shear-banding and microstructure of colloids in shear flow“. *Faraday Discuss.* **123,** 157 (2003).

75. Jin, H., Kang, K., Ahn, K. H. & Dhont, J. K. G. „Flow instability due to coupling of shear-gradients with concentration: non-uniform flow of (hard-sphere) glasses“. *Soft Matter* **10,** 9470 (2014).

76. Krüger, M. & Brader, J. M. „Controlling colloidal sedimentation using time-dependent shear“. *EPL* **96,** 68006 (2011).

77. Brader, J. & Krüger, M. „Density profiles of a colloidal liquid at a wall under shear flow". *Mol. Phys.* **109,** 1029 (2011).

78. Reinhardt, J., Weysser, F. & Brader, J. M. „Density functional approach to nonlinear rheology". *EPL* **102,** 28011 (2013).

79. Aerov, A. A. & Krüger, M. „Driven colloidal suspensions in confinement and density functional theory: Microstructure and wall-slip". *J. Chem. Phys.* **140,** 094701 (2014).

80. Aerov, A. A. & Krüger, M. „Theory of rheology in confinement". *Phys. Rev. E* **92,** 042301 (2015).

81. Scacchi, A., Krüger, M. & Brader, J. M. „Driven colloidal fluids: construction of dynamical density functional theories from exactly solvable limits". *J. Phys.: Condens. Matter* **28,** 244023 (2016).

82. Monson, P. „Understanding adsorption/desorption hysteresis for fluids in mesoporous materials using simple molecular models and classical density functional theory". *Micropor. Mesopor. Mat.* **160,** 47 (2012).

83. Chacón, E. & Tarazona, P. „Capillary wave Hamiltonian for the Landau–Ginzburg–Wilson density functional". *J. Phys.: Condens. Matter* **28,** 244014 (2016).

84. Chacko, B., Evans, R. & Archer, A. J. „Solvent fluctuations around solvophobic, solvophilic, and patchy nanostructures and the accompanying solvent mediated interactions". *J. Chem. Phys.* **146,** 124703 (2017).

85. Lutsko, J. F. & Lam, J. „Classical density functional theory, unconstrained crystallization, and polymorphic behavior". *Phys. Rev. E* **98,** 012604 (2018).

86. Weeks, J. D., Chandler, D. & Andersen, H. C. „Role of Repulsive Forces in Determining the Equilibrium Structure of Simple Liquids". *J. Chem. Phys.* **54,** 5237 (1971).

87. Hansen-Goos, H. & Wettlaufer, J. S. „A fundamental measure theory for the sticky hard sphere fluid". *J. Chem. Phys.* **134,** 014506 (2011).

88. Sweatman, M. B. „Weighted density functional theory for simple fluids: Supercritical adsorption of a Lennard-Jones fluid in an ideal slit pore". *Phys. Rev. E* **63,** 031102 (2001).

89. Roth, R. & Gillespie, D. „Shells of charge: a density functional theory for charged hard spheres". *J. Phys.: Condens. Matter* **28,** 244006 (2016).

90. Tarazona, P., A., C. J. & Martinez-Ratoń. *Theory and simulation of hard-sphere fluids and related systems* (Springer, 2008).

91. Lutsko, J. F. „Recent developments in classical density functional theory". *Adv. Chem. Phys.* **144,** 1 (2010).

92. Rosenfeld, Y., Schmidt, M., Löwen, H. & Tarazona, P. „Dimensional crossover and the freezing transition in density functional theory“. *J. Phys.: Condens. Matter* **8,** L577 (1996).

93. Español, P. & Löwen, H. „Derivation of dynamical density functional theory using the projection operator technique“. *J. Chem. Phys.* **131,** 244101 (2009).

94. Fortini, A., de las Heras, D., Brader, J. M. & Schmidt, M. „Superadiabatic Forces in Brownian Many-Body Dynamics“. *Phys. Rev. Lett.* **113,** 167801 (2014).

95. Schmidt, M. „Power functional theory for Newtonian many-body dynamics“. *J. Chem. Phys.* **148,** 044502 (2018).

96. Schmidt, M. „Quantum power functional theory for many-body dynamics“. *J. Chem. Phys.* **143,** 174108 (2015).

97. de las Heras, D. & Schmidt, M. „Full Canonical Information from Grand-Potential Density-Functional Theory“. *Phys. Rev. Lett.* **113,** 238304 (2014).

98. Krinninger, P., Schmidt, M. & Brader, J. M. „Nonequilibrium Phase Behavior from Minimization of Free Power Dissipation“. *Phys. Rev. Lett.* **117,** 208003 (2016).

99. Schindler, T. & Schmidt, M. „Dynamic pair correlations and superadiabatic forces in a dense Brownian liquid“. *J. Chem. Phys.* **145,** 064506 (2016).

100. Vineyard, G. H. „Scattering of Slow Neutrons by a Liquid“. *Phys. Rev.* **110,** 999 (5 1958).

101. de las Heras, D., Renner, J. & Schmidt, M. „Custom flow in overdamped Brownian dynamics“. *Phys. Rev. E* **99,** 023306 (2019).

102. Lesnicki, D., Vuilleumier, R., Carof, A. & Rotenberg, B. „Molecular Hydrodynamics from Memory Kernels“. *Phys. Rev. Lett.* **116,** 147804 (2016).

103. Jung, G., Hanke, M. & Schmid, F. „Iterative Reconstruction of Memory Kernels“. *J. Chem. Theory Comput.* **13,** 2481 (2017).

104. *Numerical implementation of DDFT in the dynamic test particle limit.* `https://github.com/mithodin/ddft-spherical`.

105. *Making a Physicist Website.* `https://map.podigee.io`.

106. Nocedal, J. „Updating quasi-Newton matrices with limited storage“. *Math. Comp.* **35,** 773 (1980).

107. Liu, D. C. & Nocedal, J. „On the limited memory BFGS method for large scale optimization“. *Math. Programming* **45,** 503 (1989).

108. Johnson, S. G. *The NLopt nonlinear-optimization package.* `https://github.com/stevengj/nlopt`.

109. Stopper, D. *Theorie der Diffusion in dichten kolloidalen Suspensionen.* Bachelor's Thesis (Eberhard Karls Universität Tübingen, 2014).

110. Harju, A., Siro, T., Canova, F. F., Hakala, S. & Rantalaiho, T. *Computational Physics on Graphics Processing Units.* in *Applied Parallel and Scientific Computing* (Springer, 2013). ISBN: 978-3-642-36803-5.

111. *Nvidia CUDA Website.* https://developer.nvidia.com/cuda-zone.

112. *Nvidia cuRAND Website.* https://developer.nvidia.com/curand.

113. *Optimizing Parallel Reduction in CUDA.* https://developer.download.nvidia.com/assets/cuda/files/reduction.pdf.

114. *Numerical implementation of the Vineyard approximation.* https://github.com/mithodin/vineyard.

5. Publications

There are three publications [1–3] contributing to the thesis. The first is a study of the hard sphere fluid under inhomogeneous shear [1], using BD simulation and PFT. We develop an approximate superadiabatic power functional with nonlocal memory to describe viscoelastic effects observed in BD simulation in steady state and transient dynamics. The second and third publications report on a study of the equilibrium dynamics of the van Hove function of a hard sphere fluid [2, 3]. The second publication [2] is a concise presentation of the results and their importance for the theory of liquids, whereas the third [3] contains a more in-depth presentation of the methodology and discusses the findings with more detail. We examine in detail adiabatic and superadiabatic forces with a combination of BD and Metropolis Monte Carlo simulations, discuss existing models for the adiabatic forces, and present a PFT approximation for the superadiabatic forces. We base this approximation on the viscoelastic superadiabatic power functional presented in [1] as well as functionals developed for colloidal mixtures by Geigenfeind et al. [37].

Chapter 2 gives an overview of the results of these studies. The publications themselves are reproduced in chapter 5.

The author's contribution to these studies is the development of software for

- GPU accelerated event-driven Brownian dynamics simulation of hard spheres in one to three dimensions,
- Metropolis Monte Carlo simulation for hard spheres in three dimensions,
- GPU accelerated DFT minimisation with planar symmetry and radial symmetry for hard spheres,
- GPU accelerated PFT minimisation with planar symmetry and radial symmetry for hard spheres,

as well as significant contributions to the development of the PFT approximation for superadiabatic forces in the relevant systems. The author generated all simulation and theoretical data on the behaviour of the hard sphere systems used in the publications with the help of the above mentioned software and was responsible for the analysis of said data. Thomas Schindler as a co-author of Ref. [3] developed the DDFT integration scheme presented in the appendix of [3] and contributed some portions of the text of that paper. Data for the van Hove function of the Lennard-Jones liquid used in [3] was produced by Thomas Schindler. Analysis of the drift of shells for the Lennard-Jones liquid (see section 2.3.1) was done by the author. The source code for the DDFT in the dynamic test particle limit was developed in collaboration between Thomas Schindler and the author, and is available online at [104].

A primer on GPU accelerated computation is given in appendix C. In addition to the research presented in this thesis, the author produced a bi-weekly podcast under the title „Making a Physicist“ [105], where he presented the methods and results of his work for a non-scientific audience.

5.1. Table of publications

Reference	Pages
Treffenstädt, L. L. & Schmidt, M. „Memory-induced motion reversal in Brownian liquids“. *Soft Matter* **16,** 1518 (2020)	55 – 63
Treffenstädt, L. L. & Schmidt, M. „Universality in Driven and Equilibrium Hard Sphere Liquid Dynamics“. *Phys. Rev. Lett.* **126,** 058002 (2021)	64 – 69
Treffenstädt, L. L. *et al.* „Dynamic Decay and Superadiabatic Forces in the van Hove Dynamics of Bulk Hard Sphere Fluids“. *SciPost Physics.* submitted. https://scipost.org/submission/2201.06099v1 (2022)	70 – 101

Soft Matter

PAPER

View Article Online
View Journal

Cite this: DOI: 10.1039/c9sm02005e

Memory-induced motion reversal in Brownian liquids

Lucas L. Treffenstädt and Matthias Schmidt *

We study the Brownian dynamics of hard spheres under spatially inhomogeneous shear, using event-driven Brownian dynamics simulations and power functional theory. We examine density and current profiles both for steady states and for the transient dynamics after switching on and switching off an external square wave shear force field. We find that a dense hard sphere fluid (volume fraction ≈ 0.35) undergoes global motion reversal after switching off the shear force field. We use power functional theory with a spatially nonlocal memory kernel to describe the superadiabatic force contributions and obtain good quantitative agreement of the theoretical results with simulation data. The theory provides an explanation for the motion reversal: internal superadiabatic nonequilibrium forces that oppose the externally driven current arise due to memory after switching off. The effect is genuinely viscoelastic: in steady state, viscous forces oppose the current, but they elastically generate an opposing current after switch-off.

Received 8th October 2019,
Accepted 7th January 2020

DOI: 10.1039/c9sm02005e

rsc.li/soft-matter-journal

I. Introduction

The non-equilibrium properties of hard spheres under shear have attracted considerable attention. Rheological experiments under steady shear, *e.g.* using silica particles,[1,2] show non-Newtonian viscosity effects, with both shear thickening and shear thinning occurring depending on the volume fraction. Shear thinning was observed in Brownian dynamics (BD) simulation, *e.g.* by Foss and Brady.[3] Dhont *et al.* studied the distortion of the microstructure of colloids using light scattering experiments.[4] Dhont and Nägele derived the viscoelastic response of a suspension of colloids to shear from the Smoluchowski equation.[5] Fuchs and coworkers have developed theoretical descriptions of these effects using mode coupling theory and integration through transients.[6–8] A thorough overview of the nonlinear rheology of colloidal dispersions has been given by Brader.[9]

Hard spheres under inhomogeneous shear exhibit a broad range of effects. In particular, inhomogeneities in the shear rate can induce particle migration[10] and thus lead to inhomogeneities in the density profile. Examples of this mechanism are lane formation, where particles move in stacked layers separated by low density bands,[11,12] and deformation of boundary density profiles of sheared systems in confinement.[13–15] Jin *et al.* studied flow instabilities in inhomogeneous shear with Browninan dynamics simulations.[16]

Theoretische Physik II, Universität Bayreuth, Universitätsstr. 30, D-95447 Bayreuth, Germany. E-mail: Matthias.Schmidt@uni-bayreuth.de

The transient behaviour in the time evolution from equilibrium to a sheared steady state and the reverse process from steady shear to equilibrium has attracted similar attention. Reinhardt *et al.*[17] studied the distortion of the pair correlation function under start-up shear. Koumakis *et al.*[18] reported on stresses in the start-up phase of shearing, in particular on the dependence of the stress overshoot on the Peclet number and on the volume fraction, using both simulation and experiments with sterically stabilized PMMA spheres using confocal microscopy and rheological measurements. Stress overshoot in start-up and cessation of shear and the connection to the microscopic fluid structure have also been studied.[19] Ackerson *et al.*[20] reported on solid-like ordering of nearly hard spheres under the influence of oscillatory shear. Krüger and Brader applied dynamic density functional theory,[21,22] extended to sheared systems with a scattering kernel approach,[13] to study sedimentation of colloids under time-dependent shear,[23] and Metzger and Butler examined the time evolution of particle clusters in periodic shear.[24]

Microscopic methods such as BD or molecular dynamics simulations are based on equations of motions which are instantaneous in time on the many-body level. However, on the one-body level, nonequilibrium states are generally dependent on the history of the system. By integrating out degrees of freedom, coarse-grained methods can be obtained, which generally have non-Markovian form, as can be shown with the Mori–Zwanzig formalism.[25,26] There is previous work done to derive accurate memory kernels for generalised Langevin equations for Brownian dynamics. Smith and Harris[27] proposed a method to approximate memory kernels and generate random

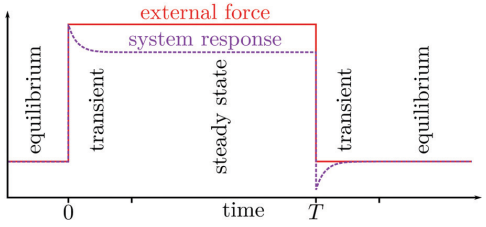

Fig. 1 Sketch of the time evolution of the system, external force (solid red line) and system response (dashed purple line) in arbitrary units. The system was in equilibrium at negative times. An external force is switched on at $t = 0$, and the system is monitored during the transient into a steady state as well as in the steady state itself. At time $t = T$, the external force is switched off and the system is observed until it has reached equilibrium again.

forces with a given autocorrelation. Szymczak and Cichocki[28] studied memory in the macroscopic dynamics of Brownian systems. Bao *et al.*[29] investigated breaking of ergodicity due to memory in non-Markovian Brownian dynamics. Recently, iterative methods have been developed to reconstruct memory kernels for generalized Langevin equations from molecular dynamics simulations by matching the force autocorrelation function or the velocity autocorrelation function between both methods.[30,31]

In this paper, we examine a system of Brownian hard spheres both in steady state under temporally constant but spatially inhomogeneous shear as well as the transient dynamics after switching the driving field both on and off. Fig. 1 shows a sketch of the dynamics: starting in a well-defined equilibrium state, a shear force field is switched on. The system needs some time to relax into a steady state. Then, the shear force field is switched off, and the system relaxes back into equilibrium. We report in particular on the shape of the current profile in the steady state under the influence of a square wave shear profile. This particular form of shear is well suited to show and examine nonlocal effects, since small regions of extreme shear rate alternate with large regions of low shear rate. We find that the transition in the current field between opposite flow directions is non-monotonic. After switching-off of the driving shear force, the current field reverses globally before settling into equilibrium.

We employ state-of-the-art event driven Brownian dynamics simulations,[32] which solve the problem of infinite gradients in the hard sphere interaction potential by evolving the system continuously with ballistic motion between BD timesteps. At fixed timesteps, the velocities of the particles are randomised according to a Maxwell distribution.

In addition to observations in simulation, the system is examined in the framework of power functional theory (PFT),[33] which describes the full non-equilibrium dynamics of many-particle systems, beyond the adiabatic approximation made in dynamical density functional theory (DDFT). DDFT is an extension of equilibrium density functional theory (DFT) to nonequilibrium systems,[34,35] which approximates the time evolution of the system through a series of adiabatic states, where the internal forces can be calculated from an equivalent equilibrium system with matching instantaneous density.[36] However, this approximation leads to shortcomings, such as underestimation of relaxation times.[34] There have been attempts to correct these shortcomings *via* empirical corrections, see *e.g.* ref. 37 and 38.

Superadiabatic forces were shown to occur in a variety of systems, such as Gaussian core particles,[39] hard spheres[40] and active Brownian particles.[41] We extend here an approximation for superadiabatic forces for Brownian hard spheres, presented recently by de las Heras and Schmidt[40] by introducing a diffusing memory kernel. This approximation derives forces from the gradient of the velocity field. The free parameters in this model – memory time, memory diffusion constant, and overall memory strength – are determined using a least-squares fit to BD simulation data.

This paper is organised as follows: in Section II, we introduce the considered system and our PFT approach. Section III contains implementation details for the BD simulations. Sections IV and V cover results in steady state and during transients, respectively. We draw conclusions and provide an outlook in Section VI.

II. Model and power functional theory

We consider a fluid of N monodisperse hard spheres with diameter σ. The system has planar geometry with Cartesian coordinates $\mathbf{r} = (x,y,z)$ and we take σ as the unit of length. Isotropy is broken by an external shear force field

$$\mathbf{f}_{\text{ext}}(\mathbf{r}) = f_{\text{ext}}(x)\hat{\mathbf{e}}_z, \tag{1}$$

where $\hat{\mathbf{e}}_z$ is the unit vector in the z-direction and $f_{\text{ext}} = |\mathbf{f}_{\text{ext}}|$ is the modulus of the force field. Since the intrinsic dynamics are diffusive, we choose as the unit of time the diffusion time $\tau = \sigma^2/D$ with diffusion constant $D = k_{\text{B}}T/\gamma$, where k_{B} is the Boltzmann constant, T indicates the absolute temperature, and γ is the friction constant against the implicit solvent.

The particle positions $\mathbf{r}_1,\ldots,\mathbf{r}_N \equiv \mathbf{r}^N$ evolve in time according to the Langevin equation of motion

$$\gamma\dot{\mathbf{r}}_i(t) = \mathbf{f}_{\text{int},i}(\mathbf{r}^N) + \mathbf{f}_{\text{ext}}(\mathbf{r}_i,t) + \sqrt{2\gamma k_{\text{B}}T}\mathbf{R}_i(t) \tag{2}$$

where $\mathbf{f}_{\text{int},i} = -\nabla_i u(\mathbf{r}^N)$ is the internal force that all other particles exert on particle i due to the interaction potential $u(\mathbf{r}^N)$ and $\mathbf{R}_i(t)$ is a delta-correlated Gaussian random white noise with $\langle\mathbf{R}_i(t)\rangle = 0$ and $\langle\mathbf{R}_i(t)\mathbf{R}_j(t')\rangle = \delta(t-t')\delta_{ij}\mathbb{1}$, where $\delta(\cdot)$ is the Dirac distribution, δ_{ij} indicates the Kronecker delta, and $\mathbb{1}$ is the 3×3 unit matrix.

The one-body density distribution is defined as

$$\rho(\mathbf{r},t) = \left\langle \sum_i \delta(\mathbf{r}-\mathbf{r}_i) \right\rangle, \tag{3}$$

where $\langle\cdot\rangle$ indicates an average over the noise and over initial microstates. The one-body current distribution is defined as

$$\mathbf{J}(\mathbf{r},t) = \left\langle \sum_i \delta(\mathbf{r}-\mathbf{r}_i)\mathbf{v}_i(t) \right\rangle, \tag{4}$$

where, in a numerical simulation, $\mathbf{v}_i$ must be calculated with a finite difference centred at time t.[42] The velocity field $\mathbf{v}(\mathbf{r},t)$ is defined as

$$\mathbf{v}(\mathbf{r},t) = \frac{\mathbf{J}(\mathbf{r},t)}{\rho(\mathbf{r},t)}. \tag{5}$$

The dynamics of (3) and (4) can be expressed as

$$\gamma\mathbf{v}(\mathbf{r},t) = \mathbf{f}_{\mathrm{int}} + \mathbf{f}_{\mathrm{ext}} - k_{\mathrm{B}}T\nabla\ln\rho, \tag{6}$$

$$\frac{\partial}{\partial t}\rho(\mathbf{r},t) = -\nabla\cdot\mathbf{J}(\mathbf{r},t), \tag{7}$$

with the total internal one-body force field given by the configurational average

$$\mathbf{f}_{\mathrm{int}}(\mathbf{r},t) = \frac{1}{\rho}\left\langle\sum_i \delta(\mathbf{r}-\mathbf{r}_i)\mathbf{f}_{\mathrm{int},i}\right\rangle. \tag{8}$$

Eqn (6) constitutes the one-body force balance relationship where the negative friction force (left hand side) is equal to the sum of internal, external and diffusive one-body forces (right hand side). The one-body continuity equation (7) is a consequence of local particle conservation and it links the density profile and the current distribution to each other. The set of equations (6) and (7) is exact and can be obtained from averaging over the many-body Smoluchowski equation (see, *e.g.*, ref. 33).

The internal force field consists of two parts according to

$$\mathbf{f}_{\mathrm{int}} = \mathbf{f}_{\mathrm{ad}} + \mathbf{f}_{\mathrm{sup}}, \tag{9}$$

with the adiabatic force ($\mathbf{f}_{\mathrm{ad}}$) and the superadiabatic force ($\mathbf{f}_{\mathrm{sup}}$) contributions.[33,36] The adiabatic force is defined as the internal force acting in a constructed equilibrium system with an external potential $V_{\mathrm{ad}}(\mathbf{r})$ chosen such that the equilibrium density matches the instantaneous density $\rho(\mathbf{r},t)$. The underlying map from the equilibrium density distribution to the external potential V_{ad} has been shown by Evans[43] and Mermin.[44] Thus, $\mathbf{f}_{\mathrm{ad}}$ depends only on the density at time t.

The superadiabatic force field, in contrast, depends in general on the history of both $\rho(\mathbf{r},t')$ and $\mathbf{J}(\mathbf{r},t')$ for $t' \leq t$, making (6) in general an implicit equation. This distinction physically defines the splitting of internal forces. Superadiabatic forces can be measured in particle-based simulations[36] and they are absent in dynamical density functional theory.[34,35]

Power functional theory is based on the free power functional $R_t[\rho,\mathbf{J}]$, which captures in a formally exact way the full many-body dynamics. R_t is microscopically defined[33] and it satisfies an instantaneous minimisation principle with respect to the current. As a result, the functional derivative with respect to the current distribution vanishes at the minimum,

$$\frac{\delta R_t[\rho,\mathbf{J}]}{\delta\mathbf{J}(\mathbf{r},t)} = 0 \quad (\min), \tag{10}$$

where the density is held fixed upon building the derivative. The functional dependence of $R_t[\rho,\mathbf{J}]$ is also on the history of the system, *i.e.* on $\rho(\mathbf{r},\tilde{t})$ and $\mathbf{J}(\mathbf{r},\tilde{t})$ for $\tilde{t} < t$. Eqn (10) determines the current $\mathbf{J}(\mathbf{r},t)$ at time t, which then allows together with the continuity eqn (7) to evolve the system in time.

The free power functional $R_t[\rho,\mathbf{J}]$ consists of a sum of intrinsic and external contributions.[33] The intrinsic contribution is composed of an adiabatic part that is the time derivative of the adiabatic free energy ($\dot{F}$) and a superadiabatic part (P_t) which is the genuine nonequilibrium contribution. Both are combined together with the external power X_t *via*[33]

$$R_t = \dot{F} + P_t - X_t. \tag{11}$$

Inserting the decomposition (11) in the condition (10) and carrying out the functional derivatives leads to the force balance relation (6). In order to illustrate this, we briefly describe all occurring terms; details can be found in ref. 33.

The time derivative of the intrinsic Helmholtz free energy functional $F[\rho]$ is given by

$$\dot{F} = \int \mathrm{d}\mathbf{r}\mathbf{J}\cdot\nabla\frac{\delta F[\rho]}{\delta\rho(\mathbf{r},t)}. \tag{12}$$

The (Helmholtz) free energy functional $F[\rho]$ consists of a sum of an ideal gas part and an excess contribution, $F_{\mathrm{exc}}[\rho]$, which arises due to the interparticle interactions. Hence

$$F[\rho] = k_{\mathrm{B}}T\int \mathrm{d}\mathbf{r}\rho[\ln(\rho\Lambda^3) - 1] + F_{\mathrm{exc}}[\rho], \tag{13}$$

where the first term on the right hand side is the ideal gas free energy functional; Λ is the (irrelevant) thermal de Broglie wavelength. In the results presented below we choose the Rosenfeld functional[45] in order to approximate the excess free energy functional $F_{\mathrm{exc}}[\rho]$ for hard spheres.

The (negative) functional derivative of $\dot{F}_{\mathrm{exc}}$ with respect to $\mathbf{J}$ generates the adiabatic force field $\mathbf{f}_{ad}$ *via*

$$\mathbf{f}_{\mathrm{ad}}(\mathbf{r},t) = -\frac{\delta\dot{F}_{\mathrm{exc}}}{\delta\mathbf{J}(\mathbf{r},t)} = -\nabla\frac{\delta F_{\mathrm{exc}}[\rho]}{\delta\rho(\mathbf{r},t)}. \tag{14}$$

As $F_{\mathrm{exc}}[\rho]$ is a density functional and hence independent of the current, the adiabatic force field $\mathbf{f}_{\mathrm{ad}}$ is also a functional of only the density profile ρ at time t.

The external power X_t, as it appears in the decomposition of the total free power (11), depends on the external force field $\mathbf{f}_{\mathrm{ext}}$, as well as on the time derivative $\dot{V}_{\mathrm{ext}}$ of the external potential. The external power is an instantaneous space integral over these one-body fields according to

$$X_t = \int \mathrm{d}\mathbf{r}(\mathbf{J}\cdot\mathbf{f}_{\mathrm{ext}} - \rho\dot{V}_{\mathrm{ext}}). \tag{15}$$

In the present application the external force field $\mathbf{f}_{\mathrm{ext}}(\mathbf{r},t)$ is the sum of the shearing force field (1) and an additional conservative force field $-\nabla V_{\mathrm{ext}}(\mathbf{r})$ which we use in order to induce particle migration effects. In the present application V_{ext} is independent of time and hence $\dot{V}_{\mathrm{ext}} = 0$.

Finally, P_t consists of a sum of the ideal gas contribution (P_t^{id}) and an excess part (P_t^{exc}), according to

$$P_t = P_t^{\mathrm{id}} + P_t^{\mathrm{exc}}. \tag{16}$$

The ideal gas dissipation functional is given by the position- and time-local expression

$$P_t^{\mathrm{id}}[\rho,\mathbf{J}] = \gamma\int \mathrm{d}\mathbf{r}\frac{\mathbf{J}^2}{2\rho}. \tag{17}$$

The superadiabatic free power functional $P_t^{\mathrm{exc}}[\rho,\mathbf{J}]$ contains all genuine nonequilibrium effects that arise from the interparticle interactions. In general, its dependence on ρ and $\mathbf{J}$ is nonlocal in both space and in time, with the temporal dependence being of the "history", *i.e.* the behaviour at earlier times, as is clear from causality. The superadiabatic force field $\mathbf{f}_{\mathrm{sup}}$, *cf.* eqn (9), is generated *via* functional differentiation,

$$\mathbf{f}_{\mathrm{sup}}(\mathbf{r},t) = -\frac{\delta P_t^{\mathrm{exc}}[\rho,\mathbf{J}]}{\delta\mathbf{J}(\mathbf{r},t)}. \tag{18}$$

P_t^{exc} is specific to the type of interparticle interaction potential and must in general be approximated. This status is very similar to that of the excess free energy functional $F_{\mathrm{exc}}[\rho]$ in equilibrium DFT. Here, we choose the velocity gradient form,[40] given by

$$\begin{aligned} P_t^{\mathrm{exc}} = \frac{1}{2}\int\mathrm{d}\mathbf{r}\int\mathrm{d}\mathbf{r}'\int_{-\infty}^{t}\mathrm{d}t'\rho(\mathbf{r},t)[\eta(\nabla\times\mathbf{v})\cdot(\nabla'\times\mathbf{v}') \\ +\zeta(\nabla\cdot\mathbf{v})(\nabla'\cdot\mathbf{v}')]\rho(\mathbf{r}',t')K(\mathbf{r}-\mathbf{r}',t-t'), \end{aligned} \tag{19}$$

where $\mathbf{v} = \mathbf{v}(\mathbf{r},t)$ is the velocity field as defined in (5); we use the shorthand $\mathbf{v}' = \mathbf{v}(\mathbf{r}',t')$ to express dependence on the primed space and time arguments, and ∇' indicates the derivative with respect to $\mathbf{r}'$.

P_t^{exc} depends not only on the instantaneous density and velocity fields, but also on the history of the system, and it is non-local in space. The constants ζ and η indicate the volume viscosity and the shear viscosity, respectively. The coupling to the history is governed by the memory kernel $K(\mathbf{r}-\mathbf{r}',t-t')$. The kernel is normalised to unity, such that $\int\mathrm{d}\mathbf{r}\int\mathrm{d}tK(\mathbf{r},t) = 1$.

We consider two different functional forms of K. The first form, K_{L}, is chosen as a simple reference. It is taken to be local in space and to possess a purely exponential temporal decay:

$$K_{\mathrm{L}}(\mathbf{r},t) = \delta(\mathbf{r})\tau_{\mathrm{M}}{}^{-1}\exp(-t/\tau_{\mathrm{M}})\Theta(t), \tag{20}$$

with τ_{M} indicating the memory time and $\Theta(\cdot)$ denoting the Heaviside step function. We expect the form (20) to perform well in cases of small shear gradients, where it models time-dependent behaviour independent of spatial correlation effects.

The second version is spatially non-local. We base its functional form on the diffusive nature of the underlying microscopic dynamics. Hence we assume that that interactions between distant particles propagate according to an effective diffusion process, characterized by a corresponding memory diffusion constant D_{M}. Specifically we assume the memory kernel to possess the form

$$K_{\mathrm{D}}(\mathbf{r},t) = \frac{\mathrm{e}^{-\mathbf{r}^2/(4D_{\mathrm{M}}t)-t/\tau_{\mathrm{M}}}}{(4\pi D_{\mathrm{M}}t)^{3/2}\tau_{\mathrm{M}}}\Theta(t), \tag{21}$$

where the memory time τ_{M} sets the time scale for the decay, as above. We shall call the form (21) the diffusing memory kernel, since the spatial part corresponds to a diffusion process. The constants τ_{M} and D_{M} are adjustable parameters that in principle are determined by the underlying interparticle interactions.

The timescale τ_{M} controls the exponential decay of the memory effect. D_{M} has the units of (length)^2 per time and it controls how fast information propagates from point $\mathbf{r}'$ to point $\mathbf{r}$ in (19) *via* a diffusion process. In the limit of $t' \to t$, the spatial part of K_{D} approaches the Dirac delta distribution. Therefore, there are no instantaneous non-local interactions in this model.

In steady state, the density and the current do not depend on time, *i.e.* $\rho(\mathbf{r},t) = \rho_{\mathrm{s}}(\mathbf{r})$ and $\mathbf{J}(\mathbf{r},t) = \mathbf{J}_{\mathrm{s}}(\mathbf{r})$ with $\nabla\cdot\mathbf{J}_{\mathrm{s}} = 0$. In this case, the time integral in (19) acts only on K and, as K is known from (20) or (21), can be carried out explicitly. The respective results for both kernels are

$$K_{\mathrm{L}}^{\mathrm{s}} = \int_{-\infty}^{t}K_{\mathrm{L}}(\mathbf{r}-\mathbf{r}',t-t')\mathrm{d}t' = \delta(\mathbf{r}-\mathbf{r}'), \tag{22}$$

$$\begin{aligned} K_{\mathrm{D}}^{\mathrm{s}} &= \int_{-\infty}^{t}K_{\mathrm{D}}(\mathbf{r}-\mathbf{r}',t-t')\mathrm{d}t' \\ &= \frac{1}{4\pi\tau_{\mathrm{M}}D_{\mathrm{M}}|\mathbf{r}-\mathbf{r}'|}\exp\left(-\frac{|\mathbf{r}-\mathbf{r}'|}{\sqrt{\tau_{\mathrm{M}}D_{\mathrm{M}}}}\right). \end{aligned} \tag{23}$$

Thus, $K_{\mathrm{L}}^{\mathrm{s}}$ does not depend on the parameter τ_{M} and $K_{\mathrm{D}}^{\mathrm{s}}$ depends only on a new length scale

$$\sigma_{\mathrm{M}} = \sqrt{\tau_{\mathrm{M}}D_{\mathrm{M}}}, \tag{24}$$

which can be interpreted as an effective interaction length in steady state. The parameters τ_{M} and D_{M} can therefore not be independently determined from measurements of one-body quantities in steady state. However, one can determine the value of σ_{M}. In steady state, it is less computationally intensive to obtain accurate density and current profiles from particle simulations, so σ_{M} can be determined with high accuracy. Knowledge of σ_{M} then reduces the number of free parameters to be determined with measurements in the full time evolution.

For the given system, all integrals in y and z in $R_t[\rho,\mathbf{J}]$ can be explicitly carried out, since density and current are by construction homogeneous in these directions. Thus, the current only depends on one space coordinate x and time t: $\mathbf{J}(x,t) = J_x(x,t)\hat{\mathbf{e}}_x + J_z(x,t)\hat{\mathbf{e}}_z$, where J_x is the current in gradient direction $\hat{\mathbf{e}}_x$, and J_z is the current in flow direction $\hat{\mathbf{e}}_z$.

It should be noted that the form of P_t^{exc} applied here contains no coupling between the flow direction and the gradient direction of $\mathbf{J}$. Therefore, a system with an initially homogeneous density and no external force acting in the x direction will always remain homogeneous in this approximation, whereas in reality, structural migration forces occur. P_t^{exc} can be extended to include these effects,[39] but that is beyond the scope of this work. Instead, we impose the density profile ρ_{BD} obtained in BD simulations *via* an external potential $V_{\mathrm{ext}}(x)$, chosen so that $\rho_{\mathrm{BD}}(x)$ is the equilibrium density in the potential.

We numerically minimize $R_t[\rho,\mathbf{J}]$ for a given $\rho(x,t)$ at time t using a generic nonlinear numerical optimiser,[46] thus solving the Euler–Lagrange-eqn (10) and obtaining $\mathbf{J}(x,t)$. Using the continuity equation (7), we numerically evolve ρ in time, *i.e.* proceed by one time step Δt and repeat the procedure. Then, we compare results for $\rho(x,t)$ and

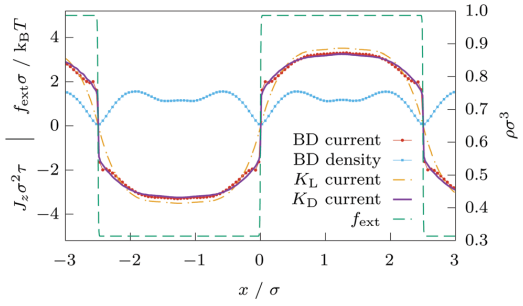

Fig. 2 Steady state current $J_z(x)$ and density profile $\rho(x)$ in BD simulation under a square wave shear force $f_{ext}(x)$ acting along $\hat{\mathbf{e}}_z$. The plot shows only part of the simulation box.

$\mathbf{J}(x,t)$ calculated with PFT to results for the same quantities sampled in BD simulations. We determine the free parameters η, τ_M, and D_M that appear in P_t^{exc} [as given by (19) together with the alternative forms for the memory kernel (20) and (21)] by using a least-squares fit to the simulation results for the velocity field. Here the simulation results are obtained *via* sampling at fixed times during the transient time evolution. For steady states we average over time. We start from reasonable estimates for the parameters and use a nonlinear numerical optimiser[46] with a derivative-free optimisation routine.[47]

III. Brownian dynamics simulations

We employ event-driven Brownian dynamics simulations[32] to integrate the Langevin equation (2) and obtain particle trajectories. We use $N = 1090$ particles in a simulation box of size $10 \times 10 \times 15\ \sigma^3$ with periodic boundary conditions in all directions. By choosing a strongly inhomogeneous shear force field, we expect to clearly showcase the importance of nonlocal interactions. Our choice of a field that is periodic in x relieves us from the need for Lees–Edwards boundary conditions,[48] which are commonly used for periodic systems with constant shear rate. We calculate one-body quantities such as density and current by averaging over many-body trajectories.

We obtain the steady state current and density profile by averaging 10^6 trajectory samples from a runlength of $10^3\tau$ after an initial relaxation period of 2τ. For start-up dynamics, the system is simulated in equilibrium for an initial 0.1τ, after which shear is switched on and the system is evolved for a further 0.4τ. Dynamics after switch-off are simulated initially for 1.5τ under shear, after which the shear force is switched off and the system is evolved for a further 0.1τ. In our experience, this protocol is sufficient to ensure that a steady state has been reached, given our parameters. Time-dependent current and density profiles for the dynamics in full non-equilibrium are then calculated per timestep *via* an average over 10^4 realisations.

IV. Steady state

We subject our system to a strongly inhomogeneous, but steady, square wave external force in z direction with an amplitude of $5\frac{k_BT}{\sigma}$ and a period of 5σ (see Fig. 2). After a short time $\approx 10^{-1}\tau$, the system settles into a steady state ($\partial_t\rho = \partial_t \mathbf{J} = 0$).

This state has some interesting properties (Fig. 2, current and density profile in steady state). The BD results indicate that, even though no external force is acting in the x direction, the density profile becomes inhomogeneous. This effect is driven purely by superadiabatic forces and is thus a true non-equilibrium effect. Phenomenological approaches to incorporate such forces into DDFT have been proposed in ref. 9 and 23. Stuhlmüller *et al.*[39] have studied shear induced particle migration in a system of Gaussian core particles with PFT. In our PFT calculations, we impose the inhomogeneous density sampled in BD with a temporally constant external potential $V_{ext}(x)$.

The harsh spatial step in the driving force field is reflected in the current profile: the current reverses its orientation in a region smaller than $\sigma/10$. Inside the regions of near-constant force, instead of a monotonic approach to the maximum, the current profile displays an oscillation close to the edge. The occurrence of this effect suggests a complex nonlocal interaction, supporting our corresponding approach in PFT.

Using a least-squares fit of the PFT velocity profile to the BD velocity profile, we obtain values for the shear viscosity η, as it appears in P_t^{exc}, *cf.* (19), as well as for σ_M, *cf.* (24); the latter variable is relevant for determining the parameters of the diffusing memory kernel K_D (23). Fig. 2 shows the resulting velocity profiles from PFT. In the given case, we obtain $\sigma_M \approx \sigma/3$, which is of the order of the hard sphere radius. The effective interaction in steady state is therefore short-ranged.

While not being perfect, the agreement between BD and PFT is much better for the diffusing memory form (21) than it is for the local form (20). Perhaps contrary to intuition, the profile obtained from the local memory model is smoother and does not represent the jump in the current profile that is observed in BD. The reason for this becomes clear when considering the effect of the spatial nonlocality of K_D.

The velocity gradient $\partial_x v_z$ has a large spike at the jump of the velocity itself. In the local memory model, this spike contributes evenly for every point in the history of the system. In the diffusing model, it is smoothed out by the integral over x' for times $t' < t$. The penalty for a jump in the velocity is thus much lower in the diffusing model.

Since P_t^{exc} depends only on inter-particle interactions and not on external forces, and should be translationally invariant, no spatially local memory kernel can accurately represent this feature in the velocity profile, no matter how complex the temporal behaviour. In other words, spatial nonlocality is not only the most general form of memory, but it is required for the correct description of strong inhomogeneities within the velocity gradient approach.

V. Transient dynamics

We next investigate the transient dynamics into and out of the steady state. First, we address the transient going from equilibrium to a sheared system. The external shear force field is the

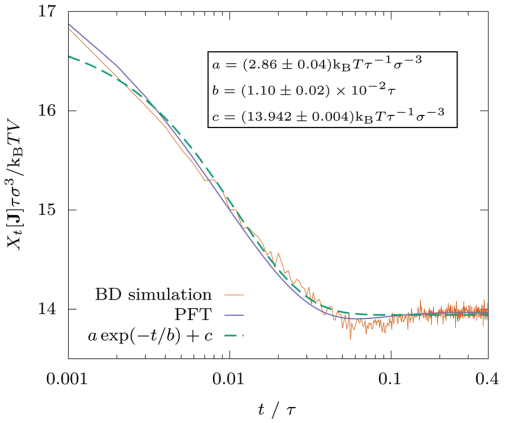

Fig. 3 Time evolution (on a logarithmic scale) of the scaled mean external power X_t per volume after switching on the shear force at $t = 0$, from BD simulation and PFT, together with a least-squares fit of a simple exponential decay $a \exp(-t/b) + c$.

same as above. It is switched on instantaneously at $t = 0$ and switched off again at a later time. The system responds instantly to the external force, with an instantaneous current profile that has larger magnitude than the steady state current. This instant response to the external force is consistent with the fact that inertia is neglected in overdamped BD. Then, viscosity slows the system down into the steady state (see Fig. 3). This process takes finite time, because the particles need to traverse, on average, the mean free path $\lambda = (\sqrt{2}\pi\rho\sigma^2)^{-1}$ between collisions,[49] which takes, with diffusive dynamics, about λ^2/D, which is $\approx 0.1\tau$ in our system.

The decay of the mean external power (15) into the steady state can be described reasonably well with an exponential decay model $X_t/V = a \exp(-t/b) + c$, where a and c are parameters with the dimension of power per volume, and b is a parameter with the dimension of a time. Physically, c can be identified as the mean steady state external power density, a as the initial mean super-steady external power density, and b as the decay time. However, the decay shows features beyond a simple exponential, which are captured by PFT with diffusing memory kernel. For times $0.05 \leq t/\tau \leq 0.1$, the external power dips below the plateau value, and the initial decay is steeper than exponential.

Next, we explore the dynamics after switching off the shear force (see Fig. 4). Surprisingly, the current does not relax

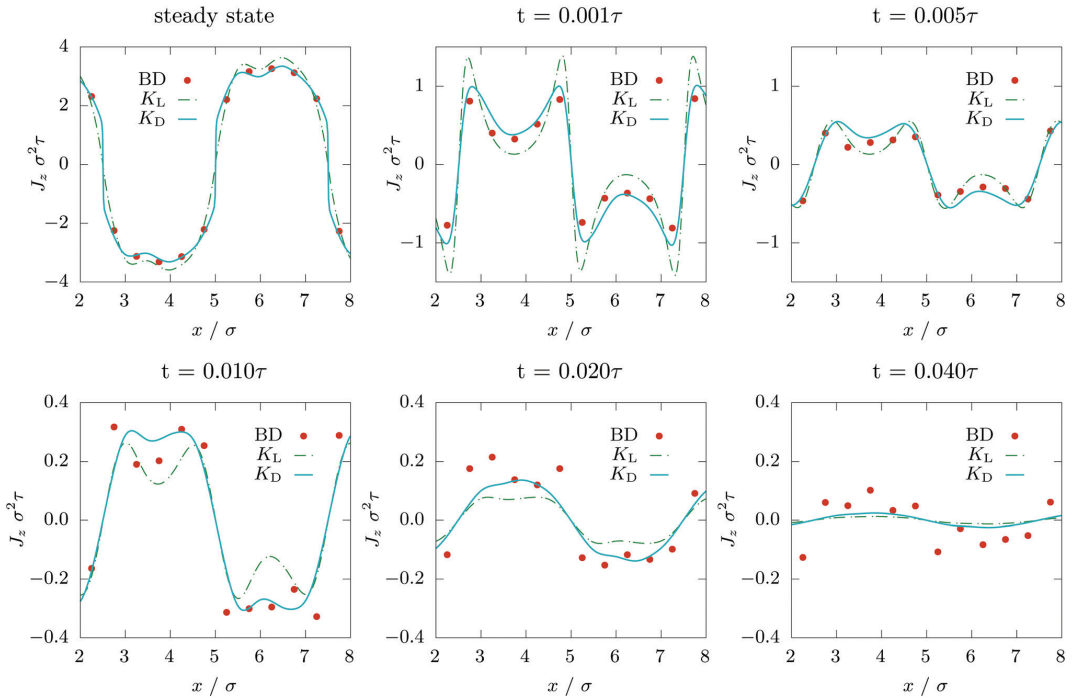

Fig. 4 Time evolution of the scaled current profile $J_x\sigma^2\tau$ as a function of x/σ after switching off the shear force at $t = 0$, obtained from BD simulation (symbols), and PFT with local memory kernel K_L (dashed line) and diffusing memory kernel K_D (solid line). The sign of the current flips globally after the shear force is switched off, followed by a decay into equilibrium. The diffusing memory model in PFT significantly outperforms the local approach in representing the BD current profiles.

monotonically into equilibrium, but rather undergoes a global reversal first, and then smoothly equilibrates. This remarkable result has perhaps been hinted at by Krüger and Brader,[23] who report "If the shear field is suddenly switched off, we find that the equilibration dynamics show an interesting symmetry with that following switch on[. . .]." Other than that, to the best of our knowledge, this effect has not been reported in the literature.

Using the time-dependent velocity field measured in BD for switch-on and switch-off, we can determine the remaining free parameters in K_L and K_D. The exponential decay in both K_L and K_D is one of the most simple forms of memory. Starting from an initial equilibrium state, the memory integral at time $t = 0$ vanishes, because the velocity gradient vanishes at negative times. Therefore, the superadiabatic force field is also zero just after switching on, and the current is directly proportional to the driving force. Memory then slowly builds up, with a dynamical behaviour that is governed in our approximation by the memory time τ_M. We obtain memory times of roughly $\tau_M = 0.02\tau$ for switch-on. The superadiabatic forces oppose the current, slowing the system into a steady state.

The steady state is truely reached once the current has not changed over a few memory times τ_M and thus the memory integral no longer changes. Then, the driving force can be switched off and the transient back into equilibrium can be observed. PFT accurately predicts the motion reversal observed in BD and provides an explanation: in the steady state, the force balance (*cf.* eqn (6)) includes adiabatic forces $\mathbf{f}_{ad}$, external forces $\mathbf{f}_{ext}$ and superadiabatic forces $\mathbf{f}_{sup}$. In the direction of shear, $\mathbf{f}_{ad}\cdot\hat{\mathbf{e}}_z = 0$ because of the homogeneity of ρ in z. As we know, $\mathbf{f}_{sup}$ is opposed to the external force. With $\mathbf{f}_{ext} = 0$ after switching-off, the superadiabatic excess forces still remain, because they arise from the memory integral. Thus, the superadiabatic forces become driving forces with an opposed direction of motion. The system returns to equilibrium only after the memory has cleared. The memory time obtained here is roughly $\tau_M = 0.01\tau$. While the decay of the counter-current is well described by the exponential decay memory model up until $t \approx 0.02\tau$, it seems to overestimate the rate of relaxation for later times (see Fig. 4).

VI. Conclusion

We have studied the Brownian hard sphere fluid under inhomogeneous, time-dependent shear with BD simulations and PFT. In steady state, under strongly inhomogeneous shear, spatially nonlocal memory shapes the current profile in ways spatially local memory cannot. Non-local memory is therefore required to describe general external forces acting on the fluid with a true separation of intrinsic and extrinsic effects. Exponential memory is an adequate and simple approximation that well describes nonequilibrium dynamics after switching (on and off) of an external field. The effect of motion reversal after switch-off is surprising if thought about in a microscopic picture, but has a straightforward explanation in PFT: slowing memory forces in steady state become driving forces after the shear force has been switched off. The rigorous framework of PFT is therefore an appropriate tool to gain insight into the behaviour of the Brownian hard-sphere fluid.

Non-local memory could be a relevant factor in the study of inhomogeneous colloidal systems such as colloids undergoing capillary collapse at an interface.[50] We are also interested to investigate the effect of the approximation presented here on the bulk dynamics of hard spheres, such as the van Hove correlation function, which has been studied recently experimentally and with DDFT.[51] To this end, we plan to employ PFT in the dynamic test particle limit.[21,22,52]

The excess superadiabatic functional can be further developed in two directions: spatially, structural forces can be incorporated with higher orders of the velocity gradient. The diffusing nonlocality provides good results, but has free parameters that need to be tuned by BD simulation or other benchmarks. Instead, they might be derived from the particle interaction, perhaps based on fundamental measures to allow for a deeper physical interpretation. Temporally, the exponential decay model could be improved. Research on memory in molecular dynamics provides a jumping-off point.[30] Recently, Jung *et al.*[31] presented a method to obtain memory kernels that could be adapted to our approach.

It would also be interesting to investigate the implications of the diffusing memory kernel (21) in the context of the non-equilibrium Ornstein–Zernike relation for the dynamical two-body structure.[53,54]

Finally, we expect the current reversal effect, presented here for Brownian hard spheres, to be reproducible in an experimental realisation with colloidal particles. External forces could be applied either mechanically, using a rheometer with a specifically designed geometry that approximates the step shear, or with optical methods. However, hydrodynamic interactions, which are neglected in our study, will likely induce additional effects.

Conflicts of interest

There are no conflicts of interest to declare.

Acknowledgements

We thank Daniel de las Heras for useful comments. This work is supported by the German Research Foundation (DFG) *via* SCHM 2632/1-1.

References

1 C. d. de Kruif, E. Van Iersel, A. Vrij and W. Russel, Hard sphere colloidal dispersions: Viscosity as a function of shear rate and volume fraction, *J. Chem. Phys.*, 1985, **83**, 4717.
2 L. Marshall and C. F. Zukoski, Experimental studies on the rheology of hard-sphere suspensions near the glass transition, *J. Phys. Chem.*, 1990, **94**, 1164.
3 D. R. Foss and J. F. Brady, Brownian dynamics simulation of hard-sphere colloidal dispersions, *J. Rheol.*, 2000, **44**, 629.

4 J. K. G. Dhont, M. P. Lettinga, Z. Dogic, T. A. J. Lenstra, H. Wang, S. Rathgeber, P. Carletto, L. Willner, H. Frielinghaus and P. Lindner, Shear-banding and microstructure of colloids in shear flow, *Faraday Discuss.*, 2003, **123**, 157.

5 J. K. G. Dhont and G. Nägele, Critical viscoelastic behavior of colloids, *Phys. Rev. E*, 1998, **58**, 7710.

6 M. Cates, C. Holmes, M. Fuchs and O. Henrich, Schematic mode coupling theories for shear thinning, shear thickening, and jamming, in *Unifying Concepts in Granular Media and Glasses*, ed. A. Coniglio, A. Fierro, H. Herrmann and M. Nicodemi, Elsevier, Amsterdam, 2004.

7 M. Fuchs and M. E. Cates, Integration through transients for Brownian particles under steady shear, *J. Phys.: Condens. Matter*, 2005, **17**, S1681.

8 M. Fuchs and M. E. Cates, A mode coupling theory for Brownian particles in homogeneous steady shear flow, *J. Rheol.*, 2009, **53**, 957.

9 J. M. Brader, Nonlinear rheology of colloidal dispersions, *J. Phys.: Condens. Matter*, 2010, **22**, 363101.

10 D. Leighton and A. Acrivos, The shear-induced migration of particles in concentrated suspensions, *J. Fluid Mech.*, 1987, **181**, 415.

11 J. Chakrabarti, J. Dzubiella and H. Löwen, Reentrance effect in the lane formation of driven colloids, *Phys. Rev. E*, 2004, **70**, 012401.

12 C. W. Wächtler, F. Kogler and S. H. L. Klapp, Lane formation in a driven attractive fluid, *Phys. Rev. E*, 2016, **94**, 052603.

13 J. M. Brader and M. Krüger, Density profiles of a colloidal liquid at a wall under shear flow, *Mol. Phys.*, 2011, **109**, 1029.

14 A. A. Aerov and M. Krüger, Driven colloidal suspensions in confinement and density functional theory: Microstructure and wall-slip, *J. Chem. Phys.*, 2014, **140**, 094701.

15 A. A. Aerov and M. Krüger, Theory of rheology in confinement, *Phys. Rev. E: Stat., Nonlinear, Soft Matter Phys.*, 2015, **92**, 042301.

16 H. Jin, K. Kang, K. H. Ahn and J. K. G. Dhont, Flow instability due to coupling of shear-gradients with concentration: non-uniform flow of (hard-sphere) glasses, *Soft Matter*, 2014, **10**, 9470.

17 J. Reinhardt, F. Weysser and J. M. Brader, Density functional approach to nonlinear rheology, *Europhys. Lett.*, 2013, **102**, 28011.

18 N. Koumakis, M. Laurati, A. R. Jacob, K. J. Mutch, A. Abdellali, A. B. Schofield, S. U. Egelhaaf, J. F. Brady and G. Petekidis, Start-up shear of concentrated colloidal hard spheres: Stresses, dynamics, and structure, *J. Rheol.*, 2016, **60**, 603.

19 S. Marenne, J. F. Morris, D. R. Foss and J. F. Brady, Unsteady shear flows of colloidal hard-sphere suspensions by dynamic simulation, *J. Rheol.*, 2017, **61**, 477.

20 B. J. Ackerson and P. N. Pusey, Shear-induced order in suspensions of hard spheres, *Phys. Rev. Lett.*, 1988, **61**, 1033.

21 A. J. Archer, P. Hopkins and M. Schmidt, Dynamics in inhomogeneous liquids and glasses via the test particle limit, *Phys. Rev. E*, 2007, **75**, 040501.

22 P. Hopkins, A. Fortini, A. J. Archer and M. Schmidt, The van Hove distribution function for Brownian hard spheres: Dynamical test particle theory and computer simulations for bulk dynamics, *J. Chem. Phys.*, 2010, **133**, 224505.

23 M. Krüger and J. M. Brader, Controlling colloidal sedimentation using time-dependent shear, *Europhys. Lett.*, 2011, **96**, 68006.

24 B. Metzger and J. E. Butler, Clouds of particles in a periodic shear flow, *Phys. Fluids*, 2012, **24**, 021703.

25 R. Zwanzig, Memory effects in irreversible thermodynamics, *Phys. Rev.*, 1961, **124**, 983.

26 H. Mori, Transport, collective motion, and Brownian motion, *Prog. Theor. Phys.*, 1965, **33**, 423.

27 D. E. Smith and C. B. Harris, Generalized Brownian dynamics. I. Numerical integration of the generalized Langevin equation through autoregressive modeling of the memory function, *J. Chem. Phys.*, 1990, **92**, 1304.

28 P. Szymczak and B. Cichocki, Memory effects in collective dynamics of Brownian suspensions, *J. Chem. Phys.*, 2004, **121**, 3329.

29 J.-D. Bao, P. Hänggi and Y.-Z. Zhuo, Non-markovian Brownian dynamics and nonergodicity, *Phys. Rev. E*, 2005, **72**, 061107.

30 D. Lesnicki, R. Vuilleumier, A. Carof and B. Rotenberg, Molecular hydrodynamics from memory kernels, *Phys. Rev. Lett.*, 2016, **116**, 147804.

31 G. Jung, M. Hanke and F. Schmid, Iterative reconstruction of memory kernels, *J. Chem. Theory Comput.*, 2017, **13**, 2481.

32 A. Scala, T. Voigtmann and C. De Michele, Event-driven Brownian dynamics for hard spheres, *J. Chem. Phys.*, 2007, **126**, 134109.

33 M. Schmidt and J. M. Brader, Power functional theory for Brownian dynamics, *J. Chem. Phys.*, 2013, **138**, 214101.

34 U. M. B. Marconi and P. Tarazona, Dynamic density functional theory of fluids, *J. Chem. Phys.*, 1999, **110**, 8032.

35 A. J. Archer and R. Evans, Dynamical density functional theory and its application to spinodal decomposition, *J. Chem. Phys.*, 2004, **121**, 4246.

36 A. Fortini, D. de las Heras, J. M. Brader and M. Schmidt, Superadiabatic forces in Brownian many-body dynamics, *Phys. Rev. Lett.*, 2014, **113**, 167801.

37 D. Stopper, K. Marolt, R. Roth and H. Hansen-Goos, Modeling diffusion in colloidal suspensions by dynamical density functional theory using fundamental measure theory of hard spheres, *Phys. Rev. E*, 2015, **92**, 022151.

38 D. Stopper, R. Roth and H. Hansen-Goos, Dynamical density functional theory for dense suspensions of colloidal hard spheres, *J. Chem. Phys.*, 2015, **143**, 181105.

39 N. C. X. Stuhlmüller, T. Eckert, D. de las Heras and M. Schmidt, Structural nonequilibrium forces in driven colloidal systems, *Phys. Rev. Lett.*, 2018, **121**, 098002.

40 D. de las Heras and M. Schmidt, Velocity gradient power functional for Brownian dynamics, *Phys. Rev. Lett.*, 2018, **120**, 028001.

41 P. Krinninger and M. Schmidt, Power functional theory for active Brownian particles: General formulation and power sum rules, *J. Chem. Phys.*, 2019, **150**, 074112.

42 D. de las Heras, J. Renner and M. Schmidt, Custom flow in overdamped Brownian dynamics, *Phys. Rev. E*, 2019, **99**, 023306.
43 R. Evans, The nature of the liquid-vapour interface and other topics in the statistical mechanics of non-uniform, classical fluids, *Adv. Phys.*, 1979, **28**, 143.
44 N. D. Mermin, Thermal properties of the inhomogeneous electron gas, *Phys. Rev.*, 1965, **137**, A1441.
45 Y. Rosenfeld, Free-energy model for the inhomogeneous hard-sphere fluid mixture and density-functional theory of freezing, *Phys. Rev. Lett.*, 1989, **63**, 980.
46 S. G. Johnson, The nlopt nonlinear-optimization package, http://ab-initio.mit.edu/nlopt.
47 M. J. Powell, A direct search optimization method that models the objective and constraint functions by linear interpolation, *Advances in optimization and numerical analysis*, Springer, 1994, pp. 51–67.
48 A. W. Lees and S. F. Edwards, The computer study of transport processes under extreme conditions, *J. Phys. C*, 1972, **5**, 1921.
49 J.-P. Hansen and I. R. McDonald, *Theory of Simple Liquids*, Academic Press, Oxford, 4th edn, 2013.
50 J. Bleibel, S. Dietrich, A. Domínguez and M. Oettel, Shock waves in capillary collapse of colloids: A model system for two-dimensional screened Newtonian gravity, *Phys. Rev. Lett.*, 2011, **107**, 128302.
51 D. Stopper, A. L. Thorneywork, R. P. A. Dullens and R. Roth, Bulk dynamics of Brownian hard disks: Dynamical density functional theory versus experiments on two-dimensional colloidal hard spheres, *J. Chem. Phys.*, 2018, **148**, 104501.
52 J. M. Brader and M. Schmidt, Power functional theory for the dynamic test particle limit, *J. Phys.: Condens. Matter*, 2015, **27**, 194106.
53 J. M. Brader and M. Schmidt, Nonequilibrium Ornstein-Zernike relation for Brownian many-body dynamics, *J. Chem. Phys.*, 2013, **139**, 104108.
54 J. M. Brader and M. Schmidt, Dynamic correlations in Brownian many-body systems, *J. Chem. Phys.*, 2014, **140**, 034104.

PHYSICAL REVIEW LETTERS **126,** 058002 (2021)

Universality in Driven and Equilibrium Hard Sphere Liquid Dynamics

Lucas L. Treffenstädt and Matthias Schmidt*
Theoretische Physik II, Physikalisches Institut, Universität Bayreuth, D-95447 Bayreuth, Germany

(Received 10 October 2020; revised 4 December 2020; accepted 5 January 2021; published 4 February 2021)

We demonstrate that the time evolution of the van Hove dynamical pair correlation function is governed by adiabatic forces that arise from the free energy and by superadiabatic forces that are induced by the flow of the van Hove function. The superadiabatic forces consist of drag, viscous, and structural contributions, as occur in active Brownian particles, in liquids under shear and in lane forming mixtures. For hard sphere liquids, we present a power functional theory that predicts these universal force fields in quantitative agreement with our Brownian dynamics simulation results.

DOI: 10.1103/PhysRevLett.126.058002

The van Hove function is arguably one of the most fundamental correlators that characterize the dynamical pair structure of a liquid on the microscopic scale [1,2]. It measures the probability of finding two particles at a distance r, where the particles are randomly chosen, but with a time lapse of duration t between the two position measurements. Both the motion of the same particle and spatiotemporal correlations of two distinct particles are captured. Significant physical insights into the dynamics of simple and complex systems could be gained from studying their van Hove function. Examples thereof include cage formation in nematic and smectic liquid crystals [3], de Gennes narrowing of liquid iron [4], self-motion of water [5], and the dynamics of colloidal hard spheres [6–8] and of colloid-polymer mixtures [9]. Experimentally, highly accurate results for the van Hove function are accessible based on the microscopy of colloidal systems [6], as well as by scattering methods. The latter yield the Fourier transform [2,5].

Much of our knowledge and understanding of the properties of the van Hove function are based on computer simulation work. Formulating a theoretical description for the complex spatial and temporal two-body dynamics remains a formidable challenge. Much insightful work has been carried out by Medina-Noyola and his coworkers on the basis of generalized Langevin equations [10–19]. Mode-coupling theory was used at high densities [20]. Furthermore, the closely related problem of identifying and studying memory kernels has received much recent attention in the context of molecular dynamics [21–25].

The dynamical test particle limit [26–28] constitutes a formally exact reformulation of the time evolution of the van Hove function in a one-body picture. Instead of working explicitly with two-body correlations, an equivalent dynamical situation is constructed in which one-body profiles evolve in time. This approach results in a significant conceptual simplification. Fixing a particle at the initial time at the origin establishes the equivalence with the original problem. The concept is formally exact, but it requires a prescription for the one-body dynamics to be useful in practice.

When choosing the dynamical density functional theory (DDFT) [29–31] to perform the one-body dynamics of the van Hove function [6–8,26,27] one finds too rapid temporal decay of the interparticle correlations [32] compared to benchmark data from Brownian dynamics (BD) computer simulations. This trend persists even when choosing Rosenfeld's fundamental measure theory [33–36] as an excellent approximation for the (hard sphere) free energy functional. Accounting for the observed reduction of particle mobility at increased density requires empirical adjustments to the DDFT framework [6–8,27].

Power functional theory (PFT) [37] provides formally exact test particle dynamics [28], albeit very little explicit knowledge of the crucial superadiabatic force contributions [37,38], i.e., those beyond DDFT, had originally been available [28]. In BD simulation work, it was shown that the superadiabatic forces that govern the van Hove function are both significant in magnitude and nontrivial in their spatial and temporal structure [39]. In a variety of nonequilibrium systems, different superadiabatic force types were identified as providing the key mechanisms for prominent physical effects, such as the emergence of viscous and structural forces in BD flow [40–42], motility-induced phase separation in active Brownian particles [43,44], spontaneous lane formation in counterdriven mixtures [45], and memory-induced motion reversal [46].

Here we show that the identical types of superadiabatic forces that rule the behavior of these driven systems determine, qualitatively and quantitatively, the van Hove function and hence the intrinsic equilibrium dynamics. That the same form of superadiabatic forces applies across such a wide range of different physical situations indicates that the microscopic liquid dynamics are governed by universal mechanisms. Besides the conceptual importance of this finding, it allows concrete crossfertilization between results obtained for apparently very different systems.

Within the dynamical test particle limit, the van Hove function is expressed as a time-dependent one-body density profile $\rho(\mathbf{r}, t)$; here $\mathbf{r}$ indicates position and t time. Often one splits into self and distinct parts: $\rho(\mathbf{r}, t) = \rho_{\text{self}}(\mathbf{r}, t) + \rho_{\text{dist}}(\mathbf{r}, t)$. At the initial time, the test ("self") particle is taken to be at the origin, and the distinct particles are distributed according to the (static) pair correlation function $g(r)$ of the bulk liquid (as prescribed by Percus' static test particle limit [47]). Hence, the initial conditions at $t = 0$ are $\rho_{\text{self}}(\mathbf{r}, 0) = \delta(\mathbf{r})$ and $\rho_{\text{dist}}(\mathbf{r}, 0) = \rho_b g(r)$, where $\delta(\cdot)$ indicates the Dirac delta function, ρ_b is the bulk fluid number density, and $r = |\mathbf{r}|$. Figure 1(a) and (b) depicts an illustration. The dynamics of the van Hove function are associated with time-dependent one-body self and distinct currents, $\mathbf{J}_{\text{self}}(\mathbf{r}, t)$ and $\mathbf{J}_{\text{dist}}(\mathbf{r}, t)$, respectively. The total van Hove current is the sum $\mathbf{J} = \mathbf{J}_{\text{self}} + \mathbf{J}_{\text{dist}}$. A continuity equation holds for each species: $\partial\rho_\alpha/\partial t = -\nabla \cdot \mathbf{J}_\alpha$, where $\alpha = \text{self, dist}$ labels the two different species, and ∇ indicates the derivative with respect to $\mathbf{r}$. The partial one-body currents $\mathbf{J}_\alpha(\mathbf{r}, t)$ arise from free diffusion and from internal interactions. Hence, the one-body force density balance relation is

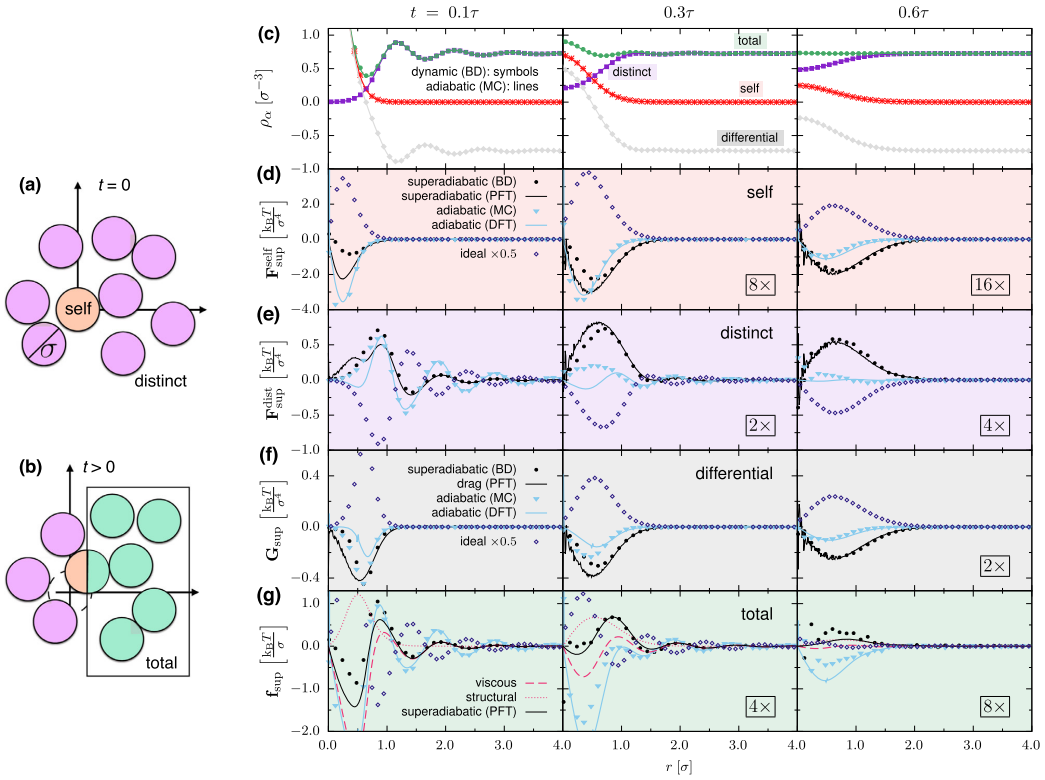

FIG. 1. Two-body dynamics of the hard sphere fluid. (a) Illustration of the van Hove dynamical two-body correlation function in a bulk liquid of hard spheres of diameter σ at time $t = 0$ and at $t > 0$ (b). (c)–(g) Results for the dynamical decay of the two-body structure of a bulk liquid of hard spheres at packing fraction 0.35 at times $t = 0.1\tau$ (left column), 0.3τ (middle column), and 0.6τ (right column) and as a function of the scaled distance r/σ. (c) Total (ρ), self (ρ_{self}), distinct (ρ_{dist}), and differential (ρ_Δ) parts of the van Hove function, as indicated. The results from BD simulation (symbols) of the time evolution and from MC simulation (lines) of the corresponding adiabatic state coincide on the scale of the plot. (d) Self part of the superadiabatic force density $\mathbf{F}^{\text{self}}_{\text{sup}}$ as obtained from BD (symbols) and from PFT (solid line); also shown is the adiabatic self force density $\mathbf{F}^{\text{self}}_{\text{ad}}$ from MC simulation (blue symbols) and DFT (blue line). The ideal self force density $-k_B T\nabla\rho_{\text{self}}$ is shown as a reference. (e) Distinct part of the superadiabatic force density $\mathbf{F}^{\text{dist}}_{\text{sup}}$ as obtained from BD and from PFT. (f) Differential superadiabatic (drag) force density $\mathbf{G}_{\text{sup}}$ as obtained from BD (symbols) and from PFT (black line), and differential adiabatic force density $\mathbf{G}_{\text{ad}}$ as arising from the adiabatic self correction. (g) Species-independent superadiabatic force field $\mathbf{f}_{\text{sup}}$ as obtained from BD and from PFT, along with the theoretical viscous ($\mathbf{f}_{\text{visc}} = -\rho^{-1}\delta P_t^{\text{visc}}/\delta\mathbf{v}$) and structural contributions ($\mathbf{f}_{\text{struc}} = -\rho^{-1}\delta P_t^{\text{struc}}/\delta\mathbf{v}$), where $\mathbf{f}_{\text{sup}} = \mathbf{f}_{\text{visc}} + \mathbf{f}_{\text{struc}}$. For the sake of clarity, the results in (d)–(g) at $t = 0.3\tau$ and 0.6τ are multiplied by factors of 2, 4, 8, or 16 as indicated.

$$\gamma \mathbf{J}_\alpha = -k_B T \nabla \rho_\alpha + \mathbf{F}^\alpha_{\rm int}, \tag{1}$$

where γ is the friction constant against the static background, k_B is the Boltzmann constant, T indicates absolute temperature, and $\mathbf{F}^\alpha_{\rm int}(\mathbf{r},t)$ is the internal force density distribution that acts on species α. No external forces act in the bulk system, and the time-dependent (nonequilibrium) situation is solely introduced by the initial conditions $\rho_\alpha(\mathbf{r},0)$.

The internal force density consists of adiabatic ($\mathbf{F}^\alpha_{\rm ad}$) and superadiabatic ($\mathbf{F}^\alpha_{\rm sup}$) contributions [37,38], according to the sum $\mathbf{F}^\alpha_{\rm int} = \mathbf{F}^\alpha_{\rm ad} + \mathbf{F}^\alpha_{\rm sup}$. Here $\mathbf{F}^\alpha_{\rm ad}(\mathbf{r},t)$ is the force density distribution in an equilibrium ("adiabatic") system that is defined to possess one-body density profiles $\rho^\alpha_{\rm ad}(\mathbf{r})$ that are identical to those in the dynamical system at time t: $\rho^\alpha_{\rm ad}(\mathbf{r}) \equiv \rho_\alpha(\mathbf{r},t)$. This adiabatic construction is performed at each point in time, and hence $\rho^\alpha_{\rm ad}(\mathbf{r})$ depends parametrically on t. The interparticle interaction potential in the adiabatic system is identical to that in the original dynamical system. The density distributions $\rho^\alpha_{\rm ad}(\mathbf{r})$ in the adiabatic system are stabilized by species-dependent external potentials $V^\alpha_{\rm ad}(\mathbf{r})$, which are guaranteed to exist in the adiabatic system due to the Mermin-Evans map of classical density functional theory (DFT) [2,29].

The adiabatic force density can be obtained by direct sampling in the adiabatic system [48] or, as we do here, from the force balance in the adiabatic system:

$$\mathbf{F}^\alpha_{\rm ad} = k_B T \nabla \rho_\alpha + \rho_\alpha \nabla V^\alpha_{\rm ad}, \tag{2}$$

where all quantities on the right-hand side are known. In practice, we use a variant of the custom flow iterative method [48], where we sample the density profile at each iteration step using Monte Carlo (MC) simulation and adjust the external potentials $V^\alpha_{\rm ad}(\mathbf{r})$ accordingly [38] until the sampled density profiles in the adiabatic system match the dynamical ("target") density profiles $\rho_\alpha(\mathbf{r},t)$.

Within classical density functional theory, the adiabatic internal force density acting on species α is given by $\mathbf{F}^\alpha_{\rm ad}(\mathbf{r},t) = -\rho_\alpha(\mathbf{r},t)\nabla \delta F_{\rm exc}/\delta \rho_\alpha(\mathbf{r},t)$, where $F_{\rm exc}$ is the excess (over ideal gas) intrinsic Helmholtz free energy functional. For the case of hard spheres, Rosenfeld's fundamental measure theory [33–36] constitutes an excellent approximation for $F_{\rm exc}$. We furthermore use the "quenched" approach by Stopper *et al.* [8], where a self-correction is applied in order to account for the fact that the self density profile represents a single particle sharply (rather than a grand ensemble average). This approach avoids having to use canonical decomposition [49,50] in order to generate results that are specific to fixed particle number.

Within PFT, the superadiabatic force density is obtained from a functional derivative of the superadiabatic excess free power functional $P^{\rm exc}_t$ according to

$$\mathbf{F}^\alpha_{\rm sup}(\mathbf{r},t) = -\frac{\delta P^{\rm exc}_t}{\delta \mathbf{v}_\alpha(\mathbf{r},t)}, \tag{3}$$

where the derivative is taken at fixed density profiles, and the species-resolved one-body velocity profile is $\mathbf{v}_\alpha(\mathbf{r},t) = \mathbf{J}_\alpha(\mathbf{r},t)/\rho_\alpha(\mathbf{r},t)$. As an approximation, we use a functional that consists of drag [43–45], viscous [40–42,45,46], and structural [41,42,44] contributions, $P^{\rm exc}_t = P^{\rm drag}_t + P^{\rm visc}_t + P^{\rm struc}_t$, according to

$$\begin{aligned} P^{\rm exc}_t = {} & \frac{C_{\rm drag}}{2} \int d\mathbf{r} \rho_{\rm self} \rho_{\rm dist} (\mathbf{v}_{\rm self} - \mathbf{v}_{\rm dist})^2 \\ & + \int d\mathbf{r} d\mathbf{r}' \int_0^t dt' n_3 n_3' (\nabla \cdot \mathbf{v})(\nabla' \cdot \mathbf{v}') K_{\rm visc} \\ & - \int d\mathbf{r} d\mathbf{r}' \int_0^t dt' (n_3' \mathbf{v}')^2 (\nabla \cdot \mathbf{J}) K_{\rm struc}, \end{aligned} \tag{4}$$

where $C_{\rm drag}$ is a constant and the kernels $K_e(\Delta\mathbf{r},\Delta t)$, where $e =$ visc, struc, depend on the relative spatial and temporal distances $\Delta\mathbf{r} = \mathbf{r} - \mathbf{r}'$ and $\Delta t = t - t'$; the local packing fraction $n_3(\mathbf{r},t)$ is obtained by convolution with $\rho(\mathbf{r},t)$ [33–36]; ∇' indicates the derivative with respect to $\mathbf{r}'$, and we use the shorthand $n_3' \equiv n_3(\mathbf{r}',t')$ and $\mathbf{v}' \equiv \mathbf{v}(\mathbf{r}',t')$. Here the total microscopic velocity profile is $\mathbf{v} = \mathbf{J}/\rho$. We use the diffusing memory form [46] for $K_e(\Delta\mathbf{r},\Delta t)$, which consists of a product of a constant C_e that controls the overall strength, an exponential decay with decay time constant τ_e, and a diffusing Gaussian with diffusion constant D_e. Explicitly the form is

$$K_e(\Delta\mathbf{r},\Delta t) = \frac{C_e \exp[-\Delta\mathbf{r}^2/(4D_e\Delta t) - \Delta t/\tau_e]}{(4\pi D_e \Delta t)^{3/2}\tau_e}. \tag{5}$$

The derivative Eq. (3), when applied to Eq. (4), yields an explicit expression for $\mathbf{F}^\alpha_{\rm sup}$, which we evaluate below, using BD data for ρ_α and $\mathbf{v}_\alpha$ as input. We choose the following set of parameters. The drag strength is $C_{\rm drag} = 2.2\gamma\sigma^3$. The values for viscous memory kernel are identical to those used in Ref. [46]: $C_{\rm visc} = 5.8 k_B T/(\sigma^3\tau)$, $D_{\rm visc} = 5.6\sigma^2/\tau$, and $\tau_{\rm visc} = 0.02\tau$. The structural memory kernel has $C_{\rm struc} = 0.42 k_B T \tau^2/\sigma^2$, $D_{\rm struc} = 0.25\sigma^2/\tau$, and $\tau_{\rm struc} = 0.8\tau$. Here the natural (Brownian) timescale is $\tau = \gamma\sigma^2/(k_B T)$, where σ is the hard sphere diameter. For standard colloids with diameter $\sigma = 1\ \mu$m dispersed in water at $T = 20$°C, using the Stokes-Einstein form for $\gamma = 3\pi\eta\sigma$ [2] gives $\gamma = 9.44 \times 10^{-13}$ kg s^{-1}, which yields $\tau = 2.33$ s. The corresponding memory times are $\tau_{\rm visc} = 0.046$ s and $\tau_{\rm struc} = 1.87$ s, i.e., values that are well inside of an experimentally accessible range. Using larger colloids [6,51] scales up the values for the memory times accordingly; the particles used, e.g., for the (two-dimensional) system of Ref. [6] are of size $\sigma = 4.04\ \mu$m, which correspondingly upscales the values for both memory times by a factor of 4.

In order to gain further insight into the nature of the relevant forces, we follow Ref. [45] and rewrite the internal forces that act in a binary mixture as consisting of a nonselective ("differential") force field ($\mathbf{f}_{\rm int}$) and a selective ("total") force density ($\mathbf{G}_{\rm int}$) such that the self and distinct internal force density distributions, respectively, can be expressed as

$$\mathbf{F}_{\rm int}^{\rm self} = \rho_{\rm self}\mathbf{f}_{\rm int} + \mathbf{G}_{\rm int}, \qquad \mathbf{F}_{\rm int}^{\rm dist} = \rho_{\rm dist}\mathbf{f}_{\rm int} - \mathbf{G}_{\rm int}. \quad (6)$$

Using the new fields $\mathbf{f}_{\rm int}$ and $\boldsymbol{G}_{\rm int}$ in the partial force density balance Eq. (1) leads to equations of motion for the total and for the "differential" motion,

$$\gamma\mathbf{v} = -k_B T\nabla\ln\rho + \mathbf{f}_{\rm int}, \quad (7)$$

$$\gamma\mathbf{J}_\Delta = -k_B T\nabla\rho_\Delta + \rho_\Delta\mathbf{f}_{\rm int} + 2\mathbf{G}_{\rm int}, \quad (8)$$

where the differential van Hove current is $\mathbf{J}_\Delta = \mathbf{J}_{\rm self} - \mathbf{J}_{\rm dist}$, and the differential van Hove function is $\rho_\Delta = \rho_{\rm self} - \rho_{\rm dist}$. Solving the linear set of Eq. (6) yields

$$\mathbf{f}_{\rm int} = \mathbf{F}_{\rm int}/\rho, \qquad \mathbf{G}_{\rm int} = (\rho_{\rm dist}\mathbf{F}_{\rm int}^{\rm self} - \rho_{\rm self}\mathbf{F}_{\rm int}^{\rm dist})/\rho, \quad (9)$$

which allows one to obtain results for $\mathbf{f}_{\rm int}(\mathbf{r},t)$ and $\mathbf{G}_{\rm int}(\mathbf{r},t)$ [from the correlators on the right-hand sides of Eq. (9)]. Due to the linearity of the transformations Eq. (9), splitting into adiabatic and superadiabatic contributions applies according to $\mathbf{f}_{\rm int} = \mathbf{f}_{\rm ad} + \mathbf{f}_{\rm sup}$ and $\mathbf{G}_{\rm int} = \mathbf{G}_{\rm ad} + \mathbf{G}_{\rm sup}$.

Figure 1(c) presents results for the van Hove function of hard spheres. Shown are the self and the distinct parts, $\rho_{\rm self}(r,t)$ and $\rho_{\rm dist}(r,t)$, at three different representative times: $t/\tau = 0.1$, 0.3, 0.6. The results are obtained using event-driven BD computer simulations [52]. We use $N = 1090$ particles in a three-dimensional simulation box of size $15\times10\times10\ \sigma^3$. The sampling is based on 10^6 time steps of size $10^{-3}\tau$, and hence an overall simulation time of $10^3\tau$. Appropriate filling of histograms of particle pair distances yields results for the van Hove function.

At the early time $t = 0.1\tau$ (first column of Fig. 1), the van Hove function has moderately decayed compared to its initial condition. Over the course of time, cf. the results for 0.3τ (middle column) and 0.6τ (right column), the self part broadens and its height correspondingly decreases. The initial correlation hole in the distinct van Hove function is gradually being filled. Besides these transport processes, the initially pronounced oscillations at distances $r \gtrsim \sigma$ decay.

We demonstrate the agreement of adiabatic and dynamical density profiles in Fig. 1(c) by showing the MC simulation results obtained from equilibrium sampling of the adiabatic state, i.e., of the system in which the external potential $V_{\rm ad}^{\rm self}(\mathbf{r})$ acts on the (single) self particle and $V_{\rm ad}^{\rm dist}(\mathbf{r})$ acts on the remaining $N-1$ particles. (As N is large enough, we do not expect that finite size effects are relevant.) Apart from very small numerical artifacts, clearly the agreement of the dynamical and adiabatic density profiles is excellent. Hence, we trust the results for the adiabatic force densities (presented below) obtained via Eq. (2).

Besides the self and distinct parts, we also show results for the total van Hove function $\rho = \rho_{\rm self} + \rho_{\rm dist}$ and the differential van Hove function $\rho_\Delta = \rho_{\rm self} - \rho_{\rm dist}$ in Fig. 1(c). Clearly the spatial structuring of ρ is much reduced upon disregarding the self-distinct labeling. Nevertheless, as all particles in the system are ultimately identical, and the self-distinct labeling was introduced for mere bookkeeping purposes, one might wonder whether the physically most relevant phenomena are revealed or are rather hidden by the labeling.

In Fig. 1(d), we show results for the different contributions to the self force density. As a reference, we plot the ideal contribution $-k_B T\nabla\rho_{\rm self}$, which tends to spread the self peak in time. Here positive (negative) values of force fields and force densities indicate the outward (inward) direction. The adiabatic force density counteracts the ideal part and hence tends to stabilize the self density peak. The DFT results agree very satisfactorily with the MC data at all times considered. The superadiabatic self force density supports the effect of $\mathbf{F}_{\rm ad}^{\rm self}$, but it has longer range and larger magnitude at later times. Except for a slight overestimation at time 0.1τ, the PFT reproduces this effect very well and hence provides a mechanism for the slowing down of the dynamics.

The contributions to the distinct force density, shown in Fig. 1(e), show more complex, oscillatory behavior at both earlier times. The ideal force density is again directly related, via the spatial derivative, to the distinct density, shown in Fig. 1(c). The oscillations of the distinct density profiles are hence imprinted into the ideal force density and their effect is to homogenize the density. As is the case for the self part, the adiabatic force density counteracts this effect and hence tends to stabilize the density oscillations. The DFT results for $\mathbf{F}_{\rm ad}^{\rm self}$ are very satisfactory, with some underestimation inside the core $r \lesssim \sigma$. The superadiabatic distinct force density has complex spatial features. It tends to slow down the decay of the spatial structure. At early times, the magnitude is smaller than that of $\mathbf{F}_{\rm ad}^{\rm dist}$, but this relationship changes at later times where $\mathbf{F}_{\rm sup}^{\rm dist}$ becomes dominant. Again, up to some deviations inside of the core, the PFT describes $\mathbf{F}_{\rm sup}^{\rm dist}$ in very good agreement with the BD data.

In Fig. 1(f), we show results for the contributions to the differential force density $\mathbf{G}_{\rm int}$ [as defined in Eq. (9)], which is relevant for the differential equation of motion, Eq. (8). Within the PFT, we can clearly identify that $\mathbf{G}_{\rm sup}$ is solely due to the drag effect, i.e., the friction generated by the interflow of the self and distinct components. This result is relevant for the hard sphere dynamics at long times. Taking only the drag force as the dominant internal effect and

balancing it with ideal diffusion, the long time self diffusion coefficient follows as $D_L = k_B T/(\gamma + \rho_b C_{\text{drag}})$. Within this approximation, we obtain $D_L = 0.38\sigma^2/\tau$ ($= 0.16\ \mu\text{m}^2/s$ for $\sigma = 1\ \mu\text{m}$ and $\tau = 2.33$ s as above), which is in very reasonable agreement with our bare simulation result of $D_L = 0.32\sigma^2/\tau$ ($= 0.14\ \mu\text{m}^2/\text{s}$). In contrast, the motion of the total van Hove function, for which we show the relevant force fields in Fig. 1(g), is due to both compressional viscosity and structural forces, with both complex spatial and temporal behavior, which are well captured by the PFT. Crucially, while the details of the superadiabatic force fields vary depending on the type of dynamical situation considered, regarding these as arising from a kinematic functional Eq. (4) reveals their universal characteristics.

In conclusion, we have traced the mechanisms that govern the time evolution of the van Hove function for hard spheres by identifying three different and universal types of nonequilibrium force contributions, all of which have been shown previously to be relevant across a broad spectrum of nonequilibrium and driven systems. The forces are due to (i) drag of the tagged ("self") particle against the surrounding fluid of distinct particles, (ii) volume (or "bulk") viscosity due to the correlation shells undergoing compressional-expansional flow, and (iii) structural nonequilibrium effects that stabilize the spatial liquid structure against decay. The power functional approximation generates all three types of nonequilibrium force fields in quantitative agreement with Brownian dynamics computer simulation results. Our results hence demonstrate intimate interrelationships between equilibrium and nonequilibrium hard sphere properties.

It would be interesting to investigate in future work the relationship of our findings to Rosenfeld's excess entropy scaling [53,54], as advanced by Truskett and his coworkers [55,56], to the nonequilibrium Ornstein-Zernike framework [57,58], and to the findings of Dyre and coworkers on universality across systems with different interparticle interaction potentials [59,60].

We thank Daniel de las Heras and Sophie Hermann for useful comments. This work is supported by the German Research Foundation (DFG) via Project no. 317849184.

*Corresponding author.
Matthias.Schmidt@uni-bayreuth.de

[1] L. van Hove, Correlations in space and time and Born approximation scattering in systems of interacting particles, Phys. Rev. **95**, 249 (1954).
[2] J. P. Hansen and I. R. McDonald, *Theory of Simple Liquids*, 4th ed. (Academic Press, London, 2013).
[3] M. Bier, R. van Roij, M. Dijkstra, and P. van der Schoot, Self-Diffusion of Particles in Complex Fluids: Temporary Cages and Permanent Barriers, Phys. Rev. Lett. **101**, 215901 (2008).
[4] B. Wu, T. Iwashita, and T. Egami, Atomic Dynamics in Simple Liquid: de Gennes Narrowing Revisited, Phys. Rev. Lett. **120**, 135502 (2018).
[5] Y. Shinohara, W. Dmowski, T. Iwashita, D. Ishikawa, A. Q. R. Baron, and T. Egami, Local self-motion of water through the van Hove function, Phys. Rev. E **102**, 032604 (2020).
[6] D. Stopper, A. Thorneywork, R. P. A. Dullens, and R. Roth, Bulk dynamics of Brownian hard disks: Dynamical density functional theory versus experiments on two-dimensional colloidal hard spheres, J. Chem. Phys. **148**, 104501 (2018).
[7] D. Stopper, K. Marolt, R. Roth, and H. Hansen-Goos, Modeling diffusion in colloidal suspensions by dynamical density functional theory using fundamental measure theory of hard spheres, Phys. Rev. E **92**, 022151 (2015).
[8] D. Stopper, R. Roth, and H. Hansen-Goos, Communication: Dynamical density functional theory for dense suspensions of colloidal hard spheres, J. Chem. Phys. **143**, 181105 (2015).
[9] D. Stopper, R. Roth, and H. Hansen-Goos, Structural relaxation and diffusion in a model colloid-polymer mixture: Dynamical density functional theory and simulation, J. Phys. Condens. Matter **28**, 455101 (2016).
[10] L. Yeomans-Reyna and M. Medina-Noyola, Overdamped van Hove function of colloidal suspensions, Phys. Rev. E **62**, 3382 (2000).
[11] M. A. Chávez-Rojo and M. Medina-Noyolaa, Van Hove function of colloidal mixtures: Exact results, Physica (Amsterdam) **366A**, 55 (2006).
[12] L. López-Flores, L. L. Yeomans-Reyna, M. Chávez-Páez, and M. Medina-Noyola, The overdamped van Hove function of atomic liquids, J. Phys. Condens. Matter **24**, 375107 (2012).
[13] L. López-Flores, H. Ruiz-Estrada, M. Chávez-Páez, and M. Medina-Noyola, Dynamic equivalences in the hard-sphere dynamic universality class, Phys. Rev. E **88**, 042301 (2013).
[14] E. Lázaro-Lázaro, P. Mendoza-Méndez, L. F. Elizondo-Aguilera, J. A. Perera-Burgos, P. E. Ramirez-González, G. Pérez-Angel, R. Castaneda-Priego, and M. Medina-Noyola, Self-consistent generalized Langevin equation theory of the dynamics of multicomponent atomic liquids, J. Chem. Phys. **146**, 184506 (2017).
[15] L. Yeomans-Reyna, H. Acuna-Campa, F. de Jesus Guevara-Rodriguez, and M. Medina-Noyola, Self-consistent theory of collective Brownian dynamics: Theory versus simulation, Phys. Rev. E **67**, 021108 (2003).
[16] L. Yeomans-Reyna, M. A. Chávez-Rojo, P. E. Ramirez-González, R. Juárez-Maldonado, M. Chávez-Páez, and M. Medina-Noyola, Dynamic arrest within the self-consistent generalized Langevin equation of colloid dynamics, Phys. Rev. E **76**, 041504 (2007).
[17] R. Juárez-Maldonado, M. A. Chávez-Rojo, P. E. Ramirez-González, L. Yeomans-Reyna, and M. Medina-Noyola, Simplified self-consistent theory of colloid dynamics, Phys. Rev. E **76**, 062502 (2007).
[18] M. Medina-Noyola and P. Ramirez-González, Non-equilibrium relaxation and near-arrest dynamics in colloidal suspensions, J. Phys. Condens. Matter **21**, 504103 (2009).
[19] P. Ramirez-González and M. Medina-Noyola, Aging of a homogeneously quenched colloidal glass-forming liquid, Phys. Rev. E **82**, 061504 (2010).

[20] F. Weysser, A. M. Puertas, M. Fuchs, and T. Voigtmann, Structural relaxation of polydisperse hard spheres: Comparison of the mode-coupling theory to a Langevin dynamics simulation, Phys. Rev. E **82**, 011504 (2010).

[21] D. Lesnicki, R. Vuilleumier, A. Carof, and B. Rotenberg, Molecular Hydrodynamics from Memory Kernels, Phys. Rev. Lett. **116**, 147804 (2016).

[22] D. Lesnicki and R. Vuilleumier, Microscopic flow around a diffusing particle, J. Chem. Phys. **147**, 094502 (2017).

[23] G. Jung and F. Schmid, Computing bulk and shear viscosities from simulations of fluids with dissipative and stochastic interactions, J. Chem. Phys. **144**, 204104 (2016).

[24] G. Jung, M. Hanke, and F. Schmid, Iterative reconstruction of memory kernels, J. Chem. Theory Comput. **13**, 2481 (2017).

[25] G. Jung, M. Hanke, and F. Schmid, Generalized Langevin dynamics: Construction and numerical integration of non-Markovian particle-based models, Soft Matter **14**, 9368 (2018).

[26] A. J. Archer, P. Hopkins, and M. Schmidt, Dynamics in inhomogeneous liquids and glasses via the test particle limit, Phys. Rev. E **75**, 040501(R) (2007).

[27] P. Hopkins, A. Fortini, A. J. Archer, and M. Schmidt, The van Hove distribution function for Brownian hard spheres: Dynamical test particle theory and computer simulations for bulk dynamics, J. Chem. Phys. **133**, 224505 (2010).

[28] J. M. Brader and M. Schmidt, Power functional theory for the dynamic test particle limit, J. Phys. Condens. Matter **27**, 194106 (2015).

[29] R. Evans, The nature of the liquid-vapour interface and other topics in the statistical mechanics of non-uniform, classical fluids, Adv. Phys. **28**, 143 (1979).

[30] U. M. B. Marconi and P. Tarazona, Dynamic density functional theory of fluids, J. Chem. Phys. **110**, 8032 (1999).

[31] A. J. Archer and R. Evans, Dynamical density functional theory and its application to spinodal decomposition, J. Chem. Phys. **121**, 4246 (2004).

[32] J. Reinhardt and J. M. Brader, Dynamics of localized particles from density functional theory, Phys. Rev. E **85**, 011404 (2012).

[33] Y. Rosenfeld, Free-Energy Model for the Inhomogeneous Hard-Sphere Fluid Mixture and Density-Functional Theory of Freezing, Phys. Rev. Lett. **63**, 980 (1989).

[34] P. Tarazona, J. A. Cuesta, and Y. Martinez-Raton, Density functional theories of hard particle systems, Lect. Notes Phys. **753**, 247 (2008).

[35] R. Roth, Fundamental measure theory for hard-sphere mixtures: A review, J. Phys. Condens. Matter **22**, 063102 (2010).

[36] J. F. Lutsko, Recent developments in classical density functional theory, Adv. Chem. Phys. **144**, 1 (2010).

[37] M. Schmidt and J. M. Brader, Power functional theory for Brownian dynamics, J. Chem. Phys. **138**, 214101 (2013).

[38] A. Fortini, D. de las Heras, J. M. Brader, and M. Schmidt, Superadiabatic Forces in Brownian Many-Body Dynamics, Phys. Rev. Lett. **113**, 167801 (2014).

[39] T. Schindler and M. Schmidt, Dynamic pair correlations and superadiabatic forces in a dense Brownian liquid, J. Chem. Phys. **145**, 064506 (2016).

[40] D. de las Heras and M. Schmidt, Velocity Gradient Power Functional for Brownian Dynamics, Phys. Rev. Lett. **120**, 028001 (2018).

[41] N. C. X. Stuhlmüller, T. Eckert, D. de las Heras, and M. Schmidt, Structural Nonequilibrium Forces in Driven Colloidal Systems, Phys. Rev. Lett. **121**, 098002 (2018).

[42] D. de las Heras and M. Schmidt, Flow and Structure in Nonequilibrium Brownian Many-Body Systems, Phys. Rev. Lett. **125**, 018001 (2020).

[43] P. Krinninger, M. Schmidt, and J. M. Brader, Nonequilibrium Phase Behaviour from Minimization of Free Power Dissipation, Phys. Rev. Lett. **117**, 208003 (2016).

[44] S. Hermann, D. de las Heras, and M. Schmidt, Non-Negative Interfacial Tension in Phase-Separated Active Brownian Particles, Phys. Rev. Lett. **123**, 268002 (2019).

[45] T. Geigenfeind, D. de las Heras, and M. Schmidt, Superadiabatic demixing in nonequilibrium colloids, Commun. Phys. **3**, 23 (2020).

[46] L. L. Treffenstädt and M. Schmidt, Memory-induced motion reversal in Brownian liquids, Soft Matter **16**, 1518 (2020).

[47] J. K. Percus, Approximation Methods in Classical Statistical Mechanics, Phys. Rev. Lett. **8**, 462 (1962).

[48] D. de las Heras, J. Renner, and M. Schmidt, Custom flow in overdamped Brownian dynamics, Phys. Rev. E **99**, 023306 (2019).

[49] D. de las Heras and M. Schmidt, Full Canonical Information from Grand Potential Density Functional Theory, Phys. Rev. Lett. **113**, 238304 (2014).

[50] D. de las Heras, J. M. Brader, A. Fortini, and M. Schmidt, Particle conservation in dynamical density functional theory, J. Phys. Condens. Matter **28**, 244024 (2016).

[51] C. P. Royall, J. Dzubiella, M. Schmidt, and A. van Blaaderen, Non-Equilibrium Sedimentation of Colloids on the Particle Scale, Phys. Rev. Lett. **98**, 188304 (2007).

[52] A. Scala, T. Voigtmann, and C. De Michele, Event-driven Brownian dynamics for hard spheres, J. Chem. Phys. **126**, 134109 (2007).

[53] Y. Rosenfeld, Relation between the transport coefficients and the internal entropy of simple systems, J. Chem. Phys. **149**, 210901 (2018).

[54] J. C. Dyre, Perspective: Excess-entropy scaling, J. Chem. Phys. **149**, 210901 (2018).

[55] J. Mittal, J. R. Errington, and T. M. Truskett, Quantitative link between single-particle dynamics and static structure of supercooled liquids, J. Phys. Chem. B **110**, 18147 (2006).

[56] M. J. Pond, J. R. Errington, and T. M. Truskett, Communication: Generalizing Rosenfeld's excess-entropy scaling to predict long-time diffusivity in dense fluids of Brownian particles: From hard to ultrasoft interactions, J. Chem. Phys. **134**, 081101 (2011).

[57] J. M. Brader and M. Schmidt, Nonequilibrium Ornstein-Zernike relation for Brownian many-body dynamics, J. Chem. Phys. **139**, 104108 (2013).

[58] J. M. Brader and M. Schmidt, Dynamic correlations in Brownian many-body systems, J. Chem. Phys. **140**, 034104 (2014).

[59] J. C. Dyre, Simple liquids' quasiuniversality and the hard-sphere paradigm, J. Phys. Condens. Matter **28**, 323001 (2016).

[60] L. Costigliola, D. M. Heyes, T. B. Schrøder, and J. C. Dyre, Revisiting the Stokes-Einstein relation without a hydrodynamic diameter, J. Chem. Phys. **150**, 021101 (2019).

SciPost Physics CONTENTS

Dynamic Decay and Superadiabatic Forces in the van Hove Dynamics of Bulk Hard Sphere Fluids

Lucas L. Treffenstädt[1], Thomas Schindler[2] and Matthias Schmidt[1⋆]

1 Theoretische Physik II, Universität Bayreuth, Universitätsstr. 30, 95447 Bayreuth, Germany
2 Theoretische Physik 1, FAU Erlangen-Nürnberg, 91058 Erlangen, Germany
⋆ Matthias.Schmidt@uni-bayreuth.de

19th March 2022

Abstract

We study the dynamical decay of the van Hove function of Brownian hard spheres using event-driven Brownian dynamics simulations and dynamic test particle theory. Relevant decays mechanisms include deconfinement of the self particle, decay of correlation shells, and shell drift. Comparison to results for the Lennard-Jones system indicates the generality of these mechanisms for dense overdamped liquids. We use dynamical density functional theory on the basis of the Rosenfeld functional with self interaction correction. Superadiabatic forces are analysed using a recent power functional approximation. The power functional yields a modified Einstein long-time self diffusion coefficient in good agreement with simulation data.

Contents

1 Introduction

Even a homogeneous liquid at equilibrium has microscopic motion. Although the average one-body density profile is constant in space and in time, the underlying particle motion is vigorous at the particle scale. The van Hove function is the fundamental two-body correlation function to characterise the dynamics of bulk liquids [1–3]. Given a particle at the origin at time $t = 0$, the van Hove function $G(r, t)$ gives the probability density of finding a particle at a distance r away from the origin at time t. The van Hove function can be measured experimentally via confocal microscopy [2, 4] or by measuring its Fourier transform, the intermediate scattering function, and then inverse Fourier transforming to real space [3, 5]. Studying the van Hove function yields significant insight into the dynamics of simple and complex systems. Notable examples thereof include cage formation in nematic and smectic liquid crystals [6], de Gennes narrowing of liquid iron [7], self-motion of water [5] and the dynamics of colloid-polymer mixtures [8]. Likewise, much effort has been made to gain a theoretical understanding of the dynamics of the van Hove function itself. Medina-Noyola and coworkers presented a series of insightful studies based on generalised Langevin equations [9–18]. Weysser et al. used mode-coupling theory in comparison to Langevin dynamics simulations [19]. The closely related problem of complex memory in molecular dynamics has recently received much attention [20–24].

For $t = 0$, the van Hove function is proportional to the radial distribution function $g(r) \propto G(r, 0)$. The asymptotic decay of $g(r)$ at large distances r has been the subject of intensive study for a broad range of model liquids. Fisher and Widom, when studying in a one-dimensional model the decay of correlations at walls, found that a line in the temperature-density plane separates the phase diagram into a region of monotonic decay and a region of oscillatory decay [25]. The Fisher-Widom line separates the two classes of universal decay, in the sense that the type of decay applies not only to the behaviour of liquids at interfaces, but also to the large distance behaviour of the bulk liquid radial distribution function [26, 27], see e.g. [28–32] for studies in a variety of systems.

Classical density functional theory (DFT) [33, 34] has proven to be a powerful tool in the study of soft condensed matter [35]. A particular success was the development of fundamental measure theory (FMT) for the description of the hard sphere liquid [35–38]. DFT provides two pathways to calculating the radial distribution function. The Ornstein-Zernike equation relates the radial distribution function to the direct correlation function [3], which can be calculated from functionally differentiating the free energy functional [3]. This path was recently shown to be accessible even in inhomogeneous situations [39, 40]. (A nonequilibrium Ornstein-Zernike equation for time-dependent systems was proposed by Brader and Schmidt [41, 42].) Alternatively to the Ornstein-Zernike route, the radial distribution function can be calculated via Percus' static test particle limit [43]. Here, a system is put under the influence of an external potential that corresponds to the pair potential of one particle fixed at the origin. The equilibrium density distribution of the system is then proportional to $g(r)$ [3, 43]. For applications of the static test part limit, see e.g. [28, 29, 44, 45].

A similar mapping of two-body correlations to one-body distributions is possible for the van Hove function. This dynamic test particle limit was first presented using dynamic density functional theory (DDFT) [46, 47]. DDFT [34, 48, 49] is an extension of DFT, which is based

upon approximating the effects of interparticle interactions as those calculated from a free energy functional via the adiabatic construction [50], in order to obtain the time evolution of a non-equilibrium system. The dynamic test particle limit, just as its static counterpart, splits all particles in a system into a single tagged ('self') particle and the remaining ('distinct') particles. Starting from an equilibrium configuration with the self particle fixed at the origin, the self particle is released and the system evolves in time. Its one-body density profile is then proportional to the van Hove function. The dynamic test particle approach was implemented for the Lennard-Jones liquid within Brownian dynamics simulations by Schindler and Schmidt [51]. Brader and Schmidt presented a formally exact formulation of the dynamic test particle limit using power functional theory (PFT) [52, 53]. The power functional framework provides a systematic way to improve upon the well-known defects of DDFT, such as the overestimation of relaxation rates [48, 54]. At the core of PFT is the formally exact splitting of the time-dependent one-body internal force field into adiabatic and superadiabatic contributions. The former can be obtained from the equilibrium free energy functional, and the latter constitute genuine nonequilibrium, flow-dependent forces that are generated by the superadiabatic power functional.

There is much recent and renewed interest in the dynamics of the van Hove function. Stopper et al. studied the van Hove function of a hard sphere liquid at densities up to $0.76\sigma^{-3}$, using dynamic density functional theory (DDFT) with a partially linearised White Bear Mk. 2 excess free energy functional [55]. The authors also carried out kinetic Monte Carlo simulations. They subsequently improved upon their approach by introducing a 'quenched' excess free energy functional to address the problem of self interactions within the self density component. Furthermore, they introduced an inhomogeneous particle mobility correction to the DDFT equation of motion [56]. More recently, they extended their approach to two-dimensional hard discs and found good agreement of their results with experimental data obtained by video microscopy of a two-dimensional colloidal suspension of melamine formaldehyde particles [4].

Despite these successes, studies of the van Hove function with DDFT systematically neglect superadiabatic effects by construction [46, 47]. Recently, we have combined viscoelastic, drag-like and structural forces to obtain an approximation for superadiabatic forces in the dynamics of the hard sphere van Hove function [57]. This work builds upon an approximation developed for viscoelastic forces in a sheared system of hard spheres [58] and approximations developed for drag-like and structural forces in a binary system of counter-driven hard spheres [59]. In [57], we have shown that superadiabatic forces contribute significantly to the internal force field at all times. Our approximation describes the internal force field accurately starting at short times $t > 0.3\tau$ up to at least $t = 1.5\tau$, where $\tau \equiv \sigma^2/D$ is the intrinsic Brownian timescale of the system, with particle diameter σ and diffusion constant D.

Here, we expand on our previous study [57]. We investigate the van Hove function of a bulk hard sphere liquid at bulk density $\rho_B \approx 0.73\sigma^{-3}$ (packing fraction $\eta \approx 0.38$). Although the hard sphere model liquid is simple, both its static and dynamic properties are often considered to be universal and taken to represent a much wider range of systems [3, 60]. Using event-driven Brownian dynamics simulations (BD) [61], we obtain the van Hove function itself as well as the internal force field acting in this system. We compare the dynamic structural decay of the van Hove function for hard spheres with results for the Lennard Jones liquid [51]. The adiabatic contributions to the internal force field are calculated using Monte Carlo simulations [62, 63] and DDFT [48, 49] in the dynamic test particle limit. For the latter method, we evaluate the accuracy of two modifications of the free energy functional, which correct for unphysical self interactions of the test particle within the dynamic test particle limit [55, 56]. Since adiabatic forces vanish in the long-time behaviour of the van Hove function, the DDFT approximation asymptotically approaches ideal diffusion, and hence fails to model collective slowing down. Therefore, we examine the superadiabatic contributions to the internal force

field that governs the time evolution of the van Hove function. The construction of our previously presented PFT approximation [57] for the superadiabatic force field is shown in detail. Finally, we use the PFT approximation to calculate the long-time diffusion constant of the self part of the van Hove function and compare it to simulation results to evaluate the accuracy of the approximation.

This paper is structured as follows: Section 2 describes in detail the models, theory and algorithms used in our work. Section 3 presents results. Starting with the radial distribution function, we examine the dynamic structural decay of the hard sphere van Hove function in BD and DDFT and also compare with the van Hove function of the Lennard-Jones liquid. Lastly, we identify adiabatic and superadiabatic contributions to the internal force field using MC simulation and present our PFT approximation for superadiabatic forces. We summarise and give an outlook in section 4.

2 Model and Theory

2.1 Brownian Dynamics

We consider a system of N monodisperse hard spheres with diameter σ. The particle positions $\mathbf{r}_1,\dots,\mathbf{r}_N \equiv \mathbf{r}^N$ evolve in time according to the Langevin equation of motion

$$\gamma\dot{\mathbf{r}}_i(t) = \mathbf{f}_{\mathrm{int},i}(\mathbf{r}^N) + \mathbf{f}_{\mathrm{ext}}(\mathbf{r}_i,t) + \sqrt{2\gamma k_\mathrm{B}T}\mathbf{R}_i(t), \tag{1}$$

where $\gamma \equiv k_\mathrm{B}T/D$ is the friction constant of the particles against the implicit solvent, $\mathbf{f}_{\mathrm{int},i}(\mathbf{r}^N) = -\nabla_i u(\mathbf{r}^N)$ is the internal force that all other particles exert on particle $i = 1,\dots,N$ due to the interparticle interaction potential $u(\mathbf{r}^N)$. Furthermore, $\mathbf{f}_{\mathrm{ext}}(\mathbf{r},t)$ is an external one-body force field that in general drives the system out of equilibrium, and $\mathbf{R}_i(t)$ is a delta-correlated Gaussian white noise with $\langle\mathbf{R}_i(t)\rangle = 0$ and $\langle\mathbf{R}_i(t)\mathbf{R}_j(t')\rangle = \delta(t-t')\delta_{ij}\mathbb{1}$, where $\delta(\cdot)$ is the Dirac distribution, δ_{ij} indicates the Kronecker delta, and $\mathbb{1}$ is the 3×3 unit matrix. The intrinsic (Brownian) timescale of the system is τ.

Since for hard spheres the interparticle interaction potential is discontinuous at contact, integration of the equation of motion (1) requires specifically adapted algorithms. One state-of-the-art algorithm is event-driven Brownian dynamics [61], which we apply to the bulk dynamics where $\mathbf{f}_{\mathrm{ext}}(\mathbf{r},t) = 0$. We choose a fixed timestep Δt. (See [64] for adaptive Brownian dynamics for soft potentials.) At the beginning of a simulation step, the particle velocities are randomised according to the Maxwell distribution. The particles are then moved according to the laws of ballistic motion with elastic collisions. Potential particle collisions are detected in advance and handled in the order at which they occur. Once the time Δt has passed in the simulation timeframe, the particle velocities are again randomised and the process is repeated.

2.2 One- and Two-Body Correlation Functions

In a general nonequilibrium situation, the behaviour of the liquid can be characterised by the time-dependent one-body density and current distributions. The density distribution is defined as

$$\rho(\mathbf{r},t) = \left\langle \sum_{i=1}^{N} \delta(\mathbf{r}-\mathbf{r}_i(t)) \right\rangle, \tag{2}$$

where $\langle\cdot\rangle$ indicates an instantaneous average over the noise and over initial microstates. The one-body current distribution is defined as

$$\mathbf{J}(\mathbf{r},t) = \left\langle \sum_{i=1}^{N} \delta(\mathbf{r}-\mathbf{r}_i(t))\mathbf{v}_i(t) \right\rangle, \tag{3}$$

where, in a numerical simulation, the velocity $\mathbf{v}_i(t)$ of particle i must be calculated with a finite difference of the particle position, centred at time t [65]. We calculate the current distribution in our BD simulations in this manner. The density distribution is connected to the current distribution via the continuity equation

$$\frac{\partial}{\partial t}\rho(\mathbf{r},t) = -\nabla\cdot\mathbf{J}(\mathbf{r},t), \tag{4}$$

where ∇ denotes the derivative with respect to $\mathbf{r}$. Given a current $\mathbf{J}(\mathbf{r},t)$ and an initial condition $\rho(\mathbf{r},0)$, the time evolution of the density distribution follows from the continuity equation. In this work, we study a liquid in equilibrium without external fields, so the total density field is always constant and the total current distribution vanishes at all times. However, using the dynamic test particle limit [53] enables us to express time-dependent two-body quantities via one-body quantities in a suitably constructed setup, which then acquires an inhomogeneous density distribution and nonzero current (see Sec. 2.3).

The van Hove function [1,3] is a dynamical two-body correlation function, defined for a bulk fluid as

$$G(\mathbf{r},t) = \frac{1}{N}\left\langle \sum_{i=1}^{N}\sum_{j=1}^{N}\delta\left(\mathbf{r}+\mathbf{r}_j(0)-\mathbf{r}_i(t)\right)\right\rangle. \tag{5}$$

The van Hove function measures the probability of finding a particle at $\mathbf{r}$ at time t, given that there was a particle at the origin at time zero. In equilibrium without external forces, $G(\mathbf{r},t)$ is radially symmetric, and thus depends only on the modulus $r=|\mathbf{r}|$, i.e. $G(r,t)$. The double sum in (5) can be split according to

$$G(\mathbf{r},t) = \frac{1}{N}\left\langle \sum_{i=1}^{N}\delta\left(\mathbf{r}+\mathbf{r}_i(0)-\mathbf{r}_i(t)\right)\right\rangle + \frac{1}{N}\left\langle \sum_{i=1}^{N}\sum_{j\neq i}^{N}\delta\left(\mathbf{r}+\mathbf{r}_j(0)-\mathbf{r}_i(t)\right)\right\rangle \tag{6}$$

$$\equiv G_\mathrm{s}(\mathbf{r},t) + G_\mathrm{d}(\mathbf{r},t), \tag{7}$$

where $G_\mathrm{s}(\mathbf{r},t)$ is the self part of the van Hove function and $G_\mathrm{d}(\mathbf{r},t)$ is its distinct part.

2.3 Dynamic Test Particle Limit

While the van Hove function is a dynamical two-body correlation function, it can be equivalently expressed in terms of time-dependent one-body quantities of a system with a specifically constructed initial condition [46]. In a system of N identical particles in volume V, one particular particle is selected as the test (or self) particle. The system is prepared such that the test particle is at the origin, with the $N-1$ remaining particles (the distinct particles) being in equilibrium around the test particle. For $N,V\to\infty$ with the bulk number density $\rho_B = N/V = \text{const}$, the self particle is distributed according to the self density distribution

$$\rho_\mathrm{s}(\mathbf{r},0) = \delta(\mathbf{r}), \tag{8}$$

and the distinct particles are distributed according to the distinct density distribution

$$\rho_\mathrm{d}(\mathbf{r},0) = \rho_\mathrm{B} g(r), \tag{9}$$

where the normalisation is such that

$$\int_V \mathrm{d}\mathbf{r}\rho_\mathrm{s}(\mathbf{r},t) = 1 \tag{10}$$

$$\int_V \mathrm{d}\mathbf{r}\rho_\mathrm{d}(\mathbf{r},t) = N-1. \tag{11}$$

By starting from this special initial condition, we obtain for the self density distribution the correspondence

$$\rho_{\mathrm{s}}(\mathbf{r},t) = G_{\mathrm{s}}(\mathbf{r},t), \tag{12}$$

whereas the distinct particles have the density distribution

$$\rho_{\mathrm{d}}(\mathbf{r},t) = G_{\mathrm{d}}(\mathbf{r},t). \tag{13}$$

The test particle correspondence can be used to calculate the van Hove function with an approach that delivers microscopic dynamics on the one-body level, such as DDFT or PFT (see Secs. 2.4, 2.5). The time evolution can be expressed in terms of self and distinct currents $\mathbf{J}_\alpha(\mathbf{r},t)$, where $\alpha = \mathrm{s},\mathrm{d}$ is a label for the self or distinct part. The continuity equation relates van Hove current and density according to

$$\frac{\partial}{\partial t} G_\alpha(\mathbf{r},t) = -\nabla\cdot\mathbf{J}_\alpha(\mathbf{r},t). \tag{14}$$

The current arises from a force balance relationship [53, 66]

$$\gamma\mathbf{J}_\alpha(\mathbf{r},t) = -\mathrm{k_B}T\nabla G_\alpha(\mathbf{r},t) + G_\alpha(\mathbf{r},t)\mathbf{f}_{\mathrm{int},\alpha}(\mathbf{r},t), \tag{15}$$

where $-\mathrm{k_B}T\nabla G_\alpha(\mathbf{r},t)$ is the ideal force density and $\mathbf{f}_{\mathrm{int},\alpha}(\mathbf{r},t)$ is the internal force acting on $G_\alpha(\mathbf{r},t)$. The (species-labelled) internal force density is the product

$$\mathbf{F}_{\mathrm{int},\alpha}(\mathbf{r},t) = G_\alpha(\mathbf{r},t)\mathbf{f}_{\mathrm{int},\alpha}(\mathbf{r},t). \tag{16}$$

In BD simulation, we can sample the species-labelled current using (3) by considering either only the distinct particles or only the self particle. Results for $\mathbf{F}_{\mathrm{int},\alpha}(\mathbf{r},t)$ can then be calculated using (15).

The force density $\mathbf{F}_{\mathrm{int},\alpha}(\mathbf{r},t)$ consists of an adiabatic and a superadiabatic contribution,

$$\mathbf{F}_{\mathrm{int},\alpha}(\mathbf{r},t) = \mathbf{F}_{\mathrm{ad},\alpha}(\mathbf{r},t) + \mathbf{F}_{\mathrm{sup},\alpha}(\mathbf{r},t), \tag{17}$$

where the adiabatic force density $\mathbf{F}_{\mathrm{ad},\alpha}(\mathbf{r},t)$ is defined via the adiabatic construction [50]: At each fixed point in time t, one chooses a pair of external potentials $V_{\mathrm{ad,s}}(\mathbf{r},t)$ and $V_{\mathrm{ad,d}}(\mathbf{r},t)$ that act on the test particle and on the distinct particles respectively, such that the equilibrium densities $\rho_{\mathrm{s}}(\mathbf{r},t)$ and $\rho_{\mathrm{d}}(\mathbf{r},t)$ under the influence of these potentials match the van Hove function at that point in time. Hence the matching condition is

$$\rho_\alpha(\mathbf{r},t) = G_\alpha(\mathbf{r},t). \tag{18}$$

The adiabatic force field $\mathbf{f}_{\mathrm{ad},\alpha}(\mathbf{r},t) \equiv \mathbf{F}_{\mathrm{ad},\alpha}(\mathbf{r},t)/\rho_\alpha(\mathbf{r},t)$ is then defined as the internal force acting in this equilibrium system [50]. This force can be identified from a known adiabatic external potential $V_{\mathrm{ad},\alpha}(\mathbf{r},t)$ via

$$\mathbf{f}_{\mathrm{ad},\alpha}(\mathbf{r},t) = \nabla V_{\mathrm{ad},\alpha}(\mathbf{r},t) + \mathrm{k_B}T\nabla\ln\left(\rho_\alpha(\mathbf{r},t)\right). \tag{19}$$

For a known internal force density $\mathbf{F}_{\mathrm{int},\alpha}(\mathbf{r},t)$, the superadiabatic force density can then be easily calculated by subtracting $\mathbf{F}_{\mathrm{ad},\alpha}(\mathbf{r},t)$ from $\mathbf{F}_{\mathrm{int},\alpha}(\mathbf{r},t)$ (see eqn. (17)).

The adiabatic construction can be performed either with DFT or with particle-based computer simulation. In DFT, the adiabatic force field is directly available from the excess free energy functional via

$$\mathbf{f}_{\mathrm{ad},\alpha}(\mathbf{r},t) = -\nabla\frac{\delta F_{\mathrm{exc}}[\rho_{\mathrm{s}},\rho_{\mathrm{d}}]}{\delta\rho_\alpha(\mathbf{r},t)}. \tag{20}$$

In simulation, iterative methods can be applied to find the adiabatic potentials $V_{\mathrm{ad,s}}(\mathbf{r},t)$ and $V_{\mathrm{ad,d}}(\mathbf{r},t)$ [65, 67]. Using simulations has the advantage of being exact up to stochastic fluctuations and finite size effects. We choose this procedure to analyse adiabatic force profiles for a few representative points in the time evolution of the van Hove function, using Metropolis Monte Carlo simulation to obtain the adiabatic density profiles.

2.4 Dynamic Density Functional Theory

Dynamic density functional theory (DDFT) [34, 48, 49] is a method of calculating the time evolution of a one-body density distribution. In the case of an M-component mixture, we have M density components $\rho_\alpha(\mathbf{r},t)$ and M current components $\mathbf{J}_\alpha(\mathbf{r},t)$ with $\alpha = 1,\dots,M$. Each current component is approximated by the adiabatic current

$$\gamma \mathbf{J}_\alpha^{\mathrm{ad}}(\mathbf{r},t) = \rho_\alpha(\mathbf{r},t)\left[\mathbf{f}_{\mathrm{ext},\alpha}(\mathbf{r},t) - \nabla\frac{\delta F[\{\rho_\alpha(\mathbf{r},t)\}]}{\delta\rho_\alpha(\mathbf{r},t)}\right], \tag{21}$$

where $\mathbf{f}_{\mathrm{ext},\alpha}(\mathbf{r},t)$ is an external force on component α and $F[\{\rho_\alpha\}]$ is the free energy functional

$$\begin{aligned} F[\{\rho_\alpha\}] &= F_{\mathrm{exc}}[\{\rho_\alpha\}] \\ &\quad + \sum_{\alpha=1}^{M} \mathrm{k_B}T \int \mathrm{d}\mathbf{r}\rho_\alpha(\mathbf{r},t)\left(\ln\Lambda^3\rho_\alpha(\mathbf{r},t) - 1\right), \end{aligned} \tag{22}$$

with thermal de Broglie wavelength Λ and excess free energy functional $F_{\mathrm{exc}}[\{\rho_\alpha\}]$. By inserting (21) and (22) into (4), we obtain the DDFT equation of motion [34, 48, 49]

$$\begin{aligned} \gamma\frac{\partial}{\partial t}\rho_\alpha(\mathbf{r},t) &= \mathrm{k_B}T\nabla^2\rho_\alpha(\mathbf{r},t) \\ &\quad + \nabla\cdot\rho_\alpha(\mathbf{r},t)\left(\nabla\frac{\delta F_{\mathrm{exc}}[\{\rho_\alpha\}]}{\delta\rho_\alpha(\mathbf{r},t)} - \mathbf{f}_{\mathrm{ext},\alpha}(\mathbf{r},t)\right). \end{aligned} \tag{23}$$

Here, the implicit assumption is made that the adiabatic current is a fair representation of the total current in the system. However, in many cases, this assumption does not hold (see e.g. [50, 58, 68]) and we will investigate this point for the present problem below.

The test particle limit can be treated in DDFT as a special case of a binary mixture. The density is then a mixture of a self component $\rho_\mathrm{s}(\mathbf{r},t)$, representing the test particle, and a distinct component $\rho_\mathrm{d}(\mathbf{r},t)$, representing the rest of the system. The accuracy of results obtained using DDFT hinges upon having a reliable approximation of the excess free energy functional, which is not known exactly for any kind of interacting particles, save for e.g. the case of hard rods in one dimension [3, 38, 69, 70]. Since the interactions of the constituent particles of both of the density components in the test particle limit are identical, one could think that the excess free energy functional is simply $F_{\mathrm{exc}}[\rho_\mathrm{s},\rho_\mathrm{d}] = F_{\mathrm{exc}}[\rho_\mathrm{s}+\rho_\mathrm{d}]$. One would then apply the appropriate one-component excess free energy functional. However, equilibrium DFT is constructed in the grand canonical ensemble, which means that a density profile normalised to unity represents an average of one particle, instead of exactly one particle [71]. This leads to unphysical self-interactions within the self density component [47].

Stopper et al. proposed in Ref. [55] a partially linearised approach, where, for the calculation of the forces on the self density component, the contribution of $\rho_\mathrm{s}(\mathbf{r},t)$ to the excess free energy functional is expanded around $\rho_\mathrm{s}(\mathbf{r},t) = 0$, while the force field acting on the distinct component is calculated using the full, i.e. unlinearised, functional. In a follow-up paper [56], they furthermore proposed a 'quenched' free energy functional

$$F_{\mathrm{exc,q}}[\rho_\mathrm{s},\rho_\mathrm{d}] = F_{\mathrm{exc}}[\rho_\mathrm{s}+\rho_\mathrm{d}] - F_{\mathrm{exc}}[\rho_\mathrm{s}], \tag{24}$$

and found that the accuracy of their results for $G(\mathbf{r},t)$ were greatly increased over the prior method. To further evaluate the accuracy of both the partially linearised and the quenched free energy functional, we calculate reference data for the adiabatic force field using Monte Carlo simulation. This allows us to compare these quasi-exact results to approximate forces obtained using the free energy functional. As a base one-component functional, we choose the White Bear Mk. 2 free energy functional [72] with tensorial modification [73], which is known to perform very well, even up to high densities, see e.g. [74].

2.5 Power Functional Theory

The phenomenological equation of motion (23) of DDFT does not capture the full non-equilibrium dynamics of many-particle systems. Important physical effects such as drag [59], viscosity [58, 75] and structural non-equilibrium forces [59, 76–82, 82] are absent. PFT provides a formally exact method for including such effects and for calculating the full current in a non-equilibrium system [52]; see Ref. [66] for a pedagogical introduction to the framework. Both adiabatic forces, which give rise to the adiabatic current $\mathbf{J}^{\mathrm{ad}}(\mathbf{r},t)$ via equation (21), but also superadiabatic forces, which characteristically depend functionally on both the density profile *and* on the current distribution, are included. It has been shown that superadiabatic forces can be of very significant magnitude and that they are in general not trivially related to the adiabatic forces [68, 76].

The full current of an overdamped M-component liquid can be calculated in PFT in principle from a functional derivative of the total free power functional $R_t[\{\rho_\alpha,\mathbf{J}_\alpha\}]$ via

$$\frac{\delta R_t[\{\rho_\alpha,\mathbf{J}_\alpha\}]}{\delta\mathbf{J}_\alpha(\mathbf{r},t)}=0 \quad \text{(min)}, \tag{25}$$

where $R_t[\{\rho_\alpha,\mathbf{J}_\alpha\}]$ is minimal at the solution $\mathbf{J}_\alpha(\mathbf{r},t)$ to this implicit equation [52]. The functional consists of physically distinct contributions according to

$$R_t[\{\rho_\alpha,\mathbf{J}_\alpha\}]=\dot{F}[\{\rho_\alpha\}]+\sum_\alpha P_t^{\mathrm{id}}[\rho_\alpha,\mathbf{J}_\alpha]+P_t^{\mathrm{exc}}[\{\rho_\alpha,\mathbf{J}_\alpha\}]-\sum_\alpha X_t[\rho_\alpha,\mathbf{J}_\alpha]. \tag{26}$$

These contributions comprise the time derivative of the free energy functional (22)

$$\dot{F}[\{\rho_\alpha\}]=\sum_\alpha\int \mathrm{d}\mathbf{r}\,\mathbf{J}_\alpha(\mathbf{r},t)\cdot\nabla\frac{\delta F[\{\rho_\alpha\}]}{\delta\rho_\alpha(\mathbf{r},t)}, \tag{27}$$

the ideal dissipation functional

$$P_t^{\mathrm{id}}[\rho_\alpha,\mathbf{J}_\alpha]=\frac{\gamma_\alpha}{2}\int \mathrm{d}\mathbf{r}\frac{\mathbf{J}_\alpha^2(\mathbf{r},t)}{\rho_\alpha(\mathbf{r},t)}, \tag{28}$$

and the external power X_t due to the external potential $V_{\mathrm{ext},\alpha}(\mathbf{r},t)$ and external forces $\mathbf{f}_{\mathrm{ext},\alpha}(\mathbf{r},t)=-\nabla V_{\mathrm{ext},\alpha}(\mathbf{r},t)+\mathbf{f}_{\mathrm{nc},\alpha}(\mathbf{r},t)$, with non-conservative external forces $\mathbf{f}_{\mathrm{nc},\alpha}(\mathbf{r},t)$, given by

$$X_t[\rho_\alpha,\mathbf{J}_\alpha]=\int \mathrm{d}\mathbf{r}\big(\mathbf{J}_\alpha(\mathbf{r},t)\cdot\mathbf{f}_{\mathrm{ext},\alpha}(\mathbf{r},t)-\rho_\alpha(\mathbf{r},t)\dot{V}_{\mathrm{ext},\alpha}(\mathbf{r},t)\big). \tag{29}$$

The genuine nonequilibrium contributions in (26) are contained in the superadiabatic excess free power functional $P_t^{\mathrm{exc}}[\{\rho_\alpha,\mathbf{J}_\alpha\}]$. Thus, from inserting (26) into (25), we obtain the Euler-Lagrange equation [53]

$$\begin{aligned}\gamma\frac{\mathbf{J}_\alpha(\mathbf{r},t)}{\rho_\alpha(\mathbf{r},t)}&=\gamma\mathbf{v}_\alpha(\mathbf{r},t)=\\ &-\nabla\frac{\delta F[\{\rho_\alpha\}]}{\delta\rho_\alpha(\mathbf{r},t)}-\frac{\delta P_t^{\mathrm{exc}}[\{\rho_\alpha,\mathbf{J}_\alpha\}]}{\delta\mathbf{J}_\alpha(\mathbf{r},t)}+\mathbf{f}_{\mathrm{ext}}(\mathbf{r},t).\end{aligned} \tag{30}$$

The superadiabatic free power functional generates the superadiabatic interparticle force field via

$$\mathbf{f}_{\mathrm{sup},\alpha}(\mathbf{r},t)=-\frac{\delta P_t^{\mathrm{exc}}[\{\rho_\alpha,\mathbf{J}_\alpha\}]}{\delta\mathbf{J}_\alpha(\mathbf{r},t)}. \tag{31}$$

Setting $P_t^{\mathrm{exc}}=0$, the PFT equation of motion (30) reduces to the DDFT (21).

Just like F_{exc} in DFT, P_t^{exc} is not known exactly and must be approximated in practice. We recently presented an approximation for superadiabatic forces in the dynamics of the van Hove function [57]. Here, the superadiabatic free power functional consists of three contributing functionals

$$P_t^{\text{exc}}[\rho_s,\rho_d,\mathbf{J}_s,\mathbf{J}_d] = P_t^{\text{visc}}[\rho,\mathbf{J}] + P_t^{\text{struc}}[\rho,\mathbf{J}] + P_t^{\text{drag}}[\rho_s,\rho_d,\mathbf{v}_\Delta], \tag{32}$$

where $P_t^{\text{visc}}[\rho,\mathbf{J}]$, $P_t^{\text{struc}}[\rho,\mathbf{J}]$ and $P_t^{\text{drag}}[\rho_s,\rho_d,\mathbf{v}_\Delta]$ are the contributions due to viscoelasticity, structural forces, and drag, respectively. The latter functional depends on the species-labelled density profiles $\rho_\alpha(\mathbf{r},t)$ and on the difference of the species-labelled velocity fields $\mathbf{v}_\Delta(\mathbf{r},t) = \mathbf{v}_s(\mathbf{r},t) - \mathbf{v}_d(\mathbf{r},t)$. The former two functionals depend only on the total current $\mathbf{J}(\mathbf{r},t) = \mathbf{J}_s(\mathbf{r},t) + \mathbf{J}_d(\mathbf{r},t)$ and on the total density profile $\rho(\mathbf{r},t) = \rho_s(\mathbf{r},t) + \rho_d(\mathbf{r},t)$. Each of these contributions is based on functionals developed previously for repulsive spheres in nonequilibrium situations [58, 59, 75, 76]. We describe the mathematical structure of each functional in the following.

The viscoelastic contribution is based on the velocity gradient functional presented by de las Heras and Schmidt [75]. Treffenstädt and Schmidt extended this functional with a concrete approximate form for the memory kernel [58] in a study of the hard sphere liquid under inhomogeneous shear. They showed that this functional describes very accurately viscoelastic effects in the sheared hard sphere system. The general viscoelastic functional form is given by

$$P_t^{\text{visc}}[\rho,\mathbf{J}] = \int \mathrm{d}\mathbf{r} \int \mathrm{d}\mathbf{r}' \int_{-\infty}^{t} \mathrm{d}t' \rho(\mathbf{r},t)[\eta(\nabla\times\mathbf{v})\cdot(\nabla'\times\mathbf{v}') + \zeta(\nabla\cdot\mathbf{v})(\nabla'\cdot\mathbf{v}')]\rho(\mathbf{r}',t')K(\mathbf{r}-\mathbf{r}',t-t'), \tag{33}$$

where $\mathbf{v}\equiv\mathbf{v}(\mathbf{r},t)$, $\mathbf{v}'\equiv\mathbf{v}(\mathbf{r}',t')$ is a shorthand notation and η and ζ are constants. Here, $K(\mathbf{r},t)$ is a memory kernel, which describes the interaction of the system with its own past, given by

$$K(\mathbf{r},t) = \frac{\mathrm{e}^{-\mathbf{r}^2/(4D_M t)-t/\tau_M}}{(4\pi D_M t)^{3/2}\tau_M}\Theta(t), \tag{34}$$

with memory time τ_M and memory diffusion constant D_M. (For simplicity, we assume that $K(\mathbf{r},t)$ is identical for the rotational and divergence contributions in (33).) In the case of the bulk van Hove function, $P_t^{\text{visc}}[\rho,\mathbf{J}]$ simplifies, since $\nabla\times\mathbf{v}=0$ due to symmetry. In addition, we replace the local density $\rho(\mathbf{r},t)$ by the weighted density $n_3(\mathbf{r},t)$ of FMT, to better capture packing effects. The weighted density $n_3(\mathbf{r},t)$ is calculated by a convolution of the local density $\rho(\mathbf{r},t)$ with a weight function

$$\omega_3(\mathbf{r}) = \Theta(\sigma/2-|\mathbf{r}|), \tag{35}$$

where $\Theta(\cdot)$ is the Heaviside step function. From (33), we hence obtain the explicit functional form

$$P_t^{\text{visc}}[\rho,\mathbf{J}] = \frac{C_{\text{visc}}}{2}\int \mathrm{d}\mathbf{r}\int \mathrm{d}\mathbf{r}'\int_0^t \mathrm{d}t' n_3(\mathbf{r},t)(\nabla\cdot\mathbf{v})(\nabla'\cdot\mathbf{v}')n_3(\mathbf{r}',t')K(\mathbf{r}-\mathbf{r}',t-t'). \tag{36}$$

The drag contribution in (32) was originally proposed by Krinninger et al. [83, 84] and subsequently used by Geigenfeind et al. [59], who studied a binary mixture of monodisperse

hard spheres that are driven against each other and hence display nonequilibrium lane formation [85]. They identified a drag force between the two species of the liquid. Here, we use their functional to approximate the drag force between the test particle and the distinct particles

$$P_t^{\text{drag}}[\rho_s,\rho_d,\mathbf{v}_\Delta]=\frac{C_{\text{drag}}}{2}\int \mathrm{d}\mathbf{r}\rho_s(\mathbf{r},t)\rho_d(\mathbf{r},t)\mathbf{v}_\Delta^2(\mathbf{r},t), \tag{37}$$

with prefactor C_{drag}. The drag functional (37) models the friction between the different particle species, when they move in opposite directions.

Geigenfeind et al. [59] also proposed two *structural* functionals. The respective resulting structural forces create inhomogeneity in the density profile of a nonequilibrium system [59, 76, 79]. We apply a structural force term similar to eqn. (51) in [59]:

$$\begin{aligned}P_t^{\text{struc}}[\rho,\mathbf{J}]=-C_{\text{struc}}\int \mathrm{d}\mathbf{r}\int \mathrm{d}\mathbf{r}'\int_0^t \mathrm{d}t'\nabla\cdot\mathbf{J}(\mathbf{r},t)\\ K(\mathbf{r}-\mathbf{r}',t-t')n_3^2(\mathbf{r}',t')\mathbf{v}^2(\mathbf{r}',t'),\end{aligned} \tag{38}$$

where C_{struc} is a prefactor, and $K(\mathbf{r},t)$ is a memory kernel of the form (34), but with different parameters D_M and τ_M as used in the viscoelastic functional (36).

The functionals (36) - (38) and the corresponding superadiabatic forces that result from functional differentiation according to (31) fall into two different categories, as characterised by the symmetry between the force fields acting on the self and distinct density components, respectively. In the category of *total forces*, the force fields $\mathbf{f}_s(\mathbf{r},t)$ and $\mathbf{f}_d(\mathbf{r},t)$ acting on the self and distinct density components, respectively, are identical: $\mathbf{f}_s(\mathbf{r},t)=\mathbf{f}_d(\mathbf{r},t)$. This means that the force field from these functionals does not depend on species-labelled information, but rather depends only on the total density and current in the test particle system.

On the other hand, in the category of *differential forces*, the force densities $\mathbf{F}_s(\mathbf{r},t)$ and $\mathbf{F}_d(\mathbf{r},t)$ acting on the two density components are equal in magnitude, but opposite in direction: $\mathbf{F}_s(\mathbf{r},t)=-\mathbf{F}_d(\mathbf{r},t)$. The two categories were developed by Geigenfeind et al. for a binary colloidal system [59], but they are general and hence apply in the context of the van Hove function as well.

For $P_t^{\text{drag}}[\rho,\mathbf{J}]$, the force density components satisfy the relation

$$\begin{aligned}\mathbf{F}_s^{\text{drag}}(\mathbf{r},t)&\equiv-\frac{\delta P_t^{\text{drag}}[\rho_s,\rho_d,\mathbf{v}_\Delta]}{\delta\mathbf{v}_s(\mathbf{r},t)}\\ &=-C_{\text{drag}}\rho_s(\mathbf{r},t)\rho_d(\mathbf{r},t)\mathbf{v}_\Delta(\mathbf{r},t)\\ &=-\mathbf{F}_d^{\text{drag}}(\mathbf{r},t).\end{aligned} \tag{39}$$

Thus, the drag functional falls into the *differential* category, and the total drag force density vanishes,

$$\mathbf{F}_{\text{sup}}^{\text{drag}}(\mathbf{r},t)=\mathbf{F}_s^{\text{drag}}(\mathbf{r},t)+\mathbf{F}_d^{\text{drag}}(\mathbf{r},t)=0. \tag{40}$$

This implies that there is no total drag force due to this functional. (See Refs. [82,86] for exact force sum rules that stem from Noether's Theorem.)

Geigenfeind et al. [59] defined the differential force density $\mathbf{G}(\mathbf{r},t)$ as a linear combination of species-resolved force densities

$$\mathbf{G}(\mathbf{r},t)\equiv\frac{\rho_d(\mathbf{r},t)}{\rho(\mathbf{r},t)}\mathbf{F}_s(\mathbf{r},t)-\frac{\rho_s(\mathbf{r},t)}{\rho(\mathbf{r},t)}\mathbf{F}_d(\mathbf{r},t). \tag{41}$$

(Note that $\mathbf{G}(\mathbf{r},t)$ is not to be confused with the van Hove function $G_\alpha(\mathbf{r},t)$, $\alpha = \mathrm{s},\mathrm{d}$.) In the case of the drag functional (37) we obtain (41) explicitly as

$$\mathbf{G}^{\mathrm{drag}}(\mathbf{r},t) = C_{\mathrm{drag}}\frac{\rho_{\mathrm{s}}(\mathbf{r},t)\rho_{\mathrm{d}}(\mathbf{r},t)}{\rho(\mathbf{r},t)}\mathbf{v}_\Delta(\mathbf{r},t)\rho_\Delta(\mathbf{r},t), \tag{42}$$

with differential density $\rho_\Delta(\mathbf{r},t) = \rho_{\mathrm{s}}(\mathbf{r},t) - \rho_{\mathrm{d}}(\mathbf{r},t)$.

In contrast, the force fields generated by the functionals $P_t^{\mathrm{visc}}[\rho,\mathbf{J}]$ and $P_t^{\mathrm{struc}}[\rho,\mathbf{J}]$ fall into the category of total forces. Therefore, the viscoelastic force density $\mathbf{F}_\alpha^{\mathrm{visc}}(\mathbf{r},t)$ for the component $\alpha = \mathrm{s},\mathrm{d}$ is

$$\mathbf{F}_\alpha^{\mathrm{visc}}(\mathbf{r},t) = -\rho_\alpha(\mathbf{r},t)\frac{\delta P_t^{\mathrm{visc}}[\rho,\mathbf{J}]}{\delta\mathbf{J}(\mathbf{r},t)} \equiv \rho_\alpha(\mathbf{r},t)\mathbf{f}^{\mathrm{visc}}(\mathbf{r},t), \tag{43}$$

where $\mathbf{f}^{\mathrm{visc}}(\mathbf{r},t)$ is species-independent. The differential force density due to the viscoelastic functional (36) vanishes,

$$\begin{aligned}\mathbf{G}^{\mathrm{visc}}(\mathbf{r},t) &= \frac{\rho_{\mathrm{d}}(\mathbf{r},t)}{\rho(\mathbf{r},t)}\mathbf{F}_{\mathrm{s}}^{\mathrm{visc}}(\mathbf{r},t) - \frac{\rho_{\mathrm{s}}(\mathbf{r},t)}{\rho(\mathbf{r},t)}\mathbf{F}_{\mathrm{d}}^{\mathrm{visc}}(\mathbf{r},t)\\ &= \frac{\rho_{\mathrm{s}}(\mathbf{r},t)\rho_{\mathrm{d}}(\mathbf{r},t)}{\rho(\mathbf{r},t)}\left(\mathbf{f}^{\mathrm{visc}}(\mathbf{r},t) - \mathbf{f}^{\mathrm{visc}}(\mathbf{r},t)\right) = 0,\end{aligned} \tag{44}$$

and the same holds true for the structural superadiabatic force density that is generated from the functional (38). Thus, splitting of superadiabatic forces into total force $\mathbf{f}_{\mathrm{sup}}(\mathbf{r},t)$ and differential force density $\mathbf{G}_{\mathrm{sup}}(\mathbf{r},t)$, instead of using the species-resolved force density $\mathbf{F}_{\mathrm{s}}(\mathbf{r},t)$ and $\mathbf{F}_{\mathrm{d}}(\mathbf{r},t)$, is helpful to identify the underlying physics of the different force terms. Summarising, we obtain within our approximation the total force

$$\mathbf{f}_{\mathrm{sup}}(\mathbf{r},t) = -\frac{\delta P_t^{\mathrm{visc}}[\rho,\mathbf{J}]}{\delta\mathbf{J}(\mathbf{r},t)} - \frac{\delta P_t^{\mathrm{struc}}[\rho,\mathbf{J}]}{\delta\mathbf{J}(\mathbf{r},t)} \tag{45}$$

$$= \frac{C_{\mathrm{visc}}}{2\rho(\mathbf{r},t)}\int \mathrm{d}\mathbf{r}'\int_0^t \mathrm{d}t' n_3'\left(\nabla'\cdot\mathbf{v}'\right)\nabla\left(n_3 K\right) - C_{\mathrm{struc}}\int \mathrm{d}\mathbf{r}'\int_0^t \mathrm{d}t' n_3'\mathbf{v}'^2\nabla K\,, \tag{46}$$

where $n_3' \equiv n_3(\mathbf{r}',t')$, $n_3 \equiv n_3(\mathbf{r},t)$ and $K \equiv K(\mathbf{r}-\mathbf{r}',t-t')$ is a shorthand notation, and the differential force density

$$\mathbf{G}_{\mathrm{sup}}(\mathbf{r},t) = -\frac{\delta P_t^{\mathrm{drag}}[\rho_{\mathrm{s}},\rho_{\mathrm{d}},\mathbf{v}_\Delta]}{\delta\mathbf{v}_\Delta(\mathbf{r},t)} = \mathbf{G}^{\mathrm{drag}}(\mathbf{r},t), \tag{47}$$

with $\mathbf{G}^{\mathrm{drag}}(\mathbf{r},t)$ as defined in (42).

2.6 Long-Time Self Diffusion

At long times $t \gg \tau$, much of the structure of the van Hove function disappears. To obtain a simplified approximation for the long-time decay of the van Hove function, we make the following assumptions, which shall be supported below by observations made in BD simulation (see Sec. 3.2 and 3.3). We take the self density profile to be a Gaussian that diffuses in time with the long-time diffusion constant D_{L},

$$\rho_{\mathrm{s}}(\mathbf{r},t) = (4\pi D_{\mathrm{L}}t)^{-3/2}\exp\left(-\frac{r^2}{4D_{\mathrm{L}}t}\right), \tag{48}$$

where the value of D_L is yet to be determined. The density profile that represents the total van Hove function is assumed to be uniform and constant,

$$\rho(\mathbf{r},t) \equiv \rho_\mathrm{s}(\mathbf{r},t) + \rho_\mathrm{d}(\mathbf{r},t) = \rho_\mathrm{B}, \tag{49}$$

hence any deviations from this infinite time behaviour are neglected. Under the assumption (49), the adiabatic force field vanishes everywhere. By inverting the spatial derivative in the continuity equation (14), we can identify the self velocity field that corresponds to (48) as

$$\mathbf{v}_\mathrm{s}(\mathbf{r},t) = \frac{r}{2t}\hat{\mathbf{e}}_r, \tag{50}$$

where $\hat{\mathbf{e}}_r$ is the radial unit vector. From (49) it follows further that the self and distinct current fields are equal in magnitude and opposite in direction, $\mathbf{J}_\mathrm{s}(\mathbf{r},t) = -\mathbf{J}_\mathrm{d}(\mathbf{r},t)$ and thus the total current vanishes,

$$\mathbf{J}(\mathbf{r},t) = 0. \tag{51}$$

Hence, the viscoelastic (36) and structural superadiabatic forces (38), which depend only on the total density and total current, vanish as well. The only remaining forces are the ideal force, which drives the long-time diffusion, and the superadiabatic drag force, which slows this process down.

The PFT Euler-Lagrange equation (30) hence simplifies under the above assumptions to

$$\frac{\delta P_t^\mathrm{id}[\mathbf{J}_\mathrm{s}]}{\delta \mathbf{J}_\mathrm{s}(\mathbf{r},t)} + \nabla \frac{\delta F_\mathrm{id}[\rho_\mathrm{s}]}{\delta \rho_\mathrm{s}(\mathbf{r},t)} + \frac{\delta P_t^\mathrm{drag}[\rho_\mathrm{s},\rho_\mathrm{d},\mathbf{v}_\Delta]}{\delta \mathbf{J}_\mathrm{s}(\mathbf{r},t)} = 0. \tag{52}$$

We show in the following that (52) can be solved analytically. After plugging in the above forms of the density field (48), the self velocity (50) and the current field (51), we obtain for the ideal dissipation functional given by (28)

$$\frac{\delta P_t^\mathrm{id}[\mathbf{J}_\mathrm{s}]}{\delta \mathbf{J}_\mathrm{s}(\mathbf{r},t)} \equiv \gamma \mathbf{v}_\mathrm{s}(\mathbf{r},t) = \gamma \frac{r}{2t}\hat{\mathbf{e}}_r, \tag{53}$$

then for the ideal diffusion functional

$$\nabla \frac{\delta F_\mathrm{id}[\rho_\mathrm{s}]}{\delta \rho_\mathrm{s}(\mathbf{r},t)} \equiv \mathrm{k_B}T \nabla \ln\left(\Lambda^3 \rho_\mathrm{s}(\mathbf{r},t)\right) = -\mathrm{k_B}T \frac{r}{2D_\mathrm{L}t}\hat{\mathbf{e}}_r, \tag{54}$$

and finally for the superadiabatic drag force

$$\begin{aligned}
\frac{\delta P_t^\mathrm{drag}[\rho_\mathrm{s},\rho_\mathrm{d},\mathbf{v}_\Delta]}{\delta \mathbf{J}_\mathrm{s}(\mathbf{r},t)} &= C_\mathrm{drag}\rho_\mathrm{d}(\mathbf{r},t)\left(\mathbf{v}_\mathrm{s}(\mathbf{r},t) - \mathbf{v}_\mathrm{d}(\mathbf{r},t)\right) \\
&= C_\mathrm{drag}\left(\mathbf{v}_\mathrm{s}(\mathbf{r},t)\rho_\mathrm{d}(\mathbf{r},t) - \mathbf{J}_\mathrm{d}(\mathbf{r},t)\right) \\
&= C_\mathrm{drag}\left(\mathbf{v}_\mathrm{s}(\mathbf{r},t)\rho_\mathrm{d}(\mathbf{r},t) + \mathbf{J}_\mathrm{s}(\mathbf{r},t)\right) \\
&= C_\mathrm{drag}\left(\mathbf{v}_\mathrm{s}(\mathbf{r},t)\rho_\mathrm{d}(\mathbf{r},t) + \mathbf{v}_\mathrm{s}(\mathbf{r},t)\rho_\mathrm{s}(\mathbf{r},t)\right) \\
&= C_\mathrm{drag}\mathbf{v}_\mathrm{s}(\mathbf{r},t)\left(\rho_\mathrm{d}(\mathbf{r},t) + \rho_\mathrm{s}(\mathbf{r},t)\right) \\
&= C_\mathrm{drag}\rho_\mathrm{B}\mathbf{v}_\mathrm{s}(\mathbf{r},t) \\
&= C_\mathrm{drag}\rho_\mathrm{B}\frac{r}{2t}\hat{\mathbf{e}}_r.
\end{aligned} \tag{55}$$

A comparison of coefficients in (52) leads to the relation

$$\gamma - \frac{\mathrm{k_B}T}{D_\mathrm{L}} + C_\mathrm{drag}\rho_\mathrm{B} = 0, \tag{56}$$

which results in a modified Einstein relation for the long-time self diffusion in an interacting system given by

$$D_{\mathrm{L}} = \frac{\mathrm{k_B}T}{\gamma + C_{\mathrm{drag}}\rho_{\mathrm{B}}}. \tag{57}$$

Below we test the approximation (57) by comparing the resulting behaviour of the diffusion coefficient D_{L} with simulation results.

The decrease of D_{L} that results from a finite value $C_{\mathrm{drag}} > 0$ according to equation (57) is an entirely superadiabatic effect. Going through the above derivation on the basis of the DDFT alone leads to the trivial results $D_{\mathrm{L}} = \mathrm{k_B}T/\gamma$, analogous to formally setting $C_{\mathrm{drag}} = 0$ in equation (57). Hence the power functional ansatz for P_t^{drag}, see equations (37) and (55), links drag (due to interflow of the self and distinct components) with the long time self diffusion coefficient.

2.7 Simulation Parameters

We simulate $N = 1090$ hard spheres in a box of size $10 \times 10 \times 15\ \sigma^3$ with periodic boundary conditions, resulting in a bulk density $\rho_{\mathrm{B}} \approx 0.73\sigma^{-3}$ and a packing fraction $\eta \approx 0.38$. The same parameters were used in [57]. We take 10^6 simulation snapshots over a simulation time of $10^3\tau$ to calculate observables.

Simulations of the Lennard-Jones liquid were carried out with $N = 500$ particles at mean number density $\rho = 0.84\sigma^{-3}$ and absolute temperature $\mathrm{k_B}T = 0.8\epsilon$ in a box with periodic boundary conditions, where ϵ sets the energy scale of the Lennard-Jones interparticle interaction potential

$$\Phi_{\mathrm{LJ}}(r) = 4\epsilon\left[\left(\frac{\sigma}{r}\right)^{12} - \left(\frac{\sigma}{r}\right)^{6}\right], \tag{58}$$

with particle distance r. The potential is truncated at $r_{\mathrm{c}} = 4\sigma$.

The DDFT calculations are carried out in a spherical box with radius 32σ and a radial discretisation step of $\Delta r = 2^{-7}\sigma = 7.8125{\cdot}10^{-3}\sigma$, beyond which both density components are continued as a constant. The integration time step is $10^{-6}\tau$. The code is available online [87].

3 Results

3.1 Radial Distribution Function

As a consistency check, we first calculate the equilibrium radial distribution function $g(r)$ from BD simulation data and compare the results with those obtained using DFT. The latter are used as an initial condition for our DDFT calculations. As described above, at $t = 0$ the distinct part of the van Hove function is equal to the radial distribution function $g(r) = G_d(r,0)/\rho_{\mathrm{B}}$. For hard spheres, $g(r)$ is zero for $r < \sigma$, which corresponds to the excluded volume around the test particle, see figure 1. Starting at $r = \sigma$ and going away from the origin, each subsequent local maximum of $g(r)$ corresponds to a correlation shell of particles around the test particle. The height of these maxima decays rapidly, with an exponential envelope, as the distance to the test particle increases. The asymptotic decay at large distances r follows an exponentially damped oscillating law

$$\frac{r}{\sigma}(g(r)-1) = \tilde{A}\mathrm{e}^{-\tilde{\alpha}_0 r}\cos(\tilde{\alpha}_1 r - \theta) \tag{59}$$

with amplitude $\tilde{A}$, inverse decay length $\tilde{\alpha}_0$, wave number $\tilde{\alpha}_1$ and phase shift θ [88]. When plotting $\ln(r\,|g(r)-1|/\sigma)$ against r (see figure 1 (b)), the exponential envelope is clearly identifiable in the diagram as a straight line along which a sequence of local maxima visibly

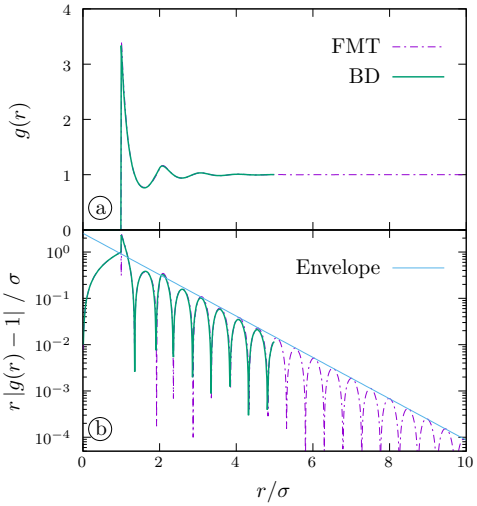

Figure 1: The radial distribution function $g(r)$ of a hard sphere liquid as a function of the distance r/σ at packing fraction $\eta \approx 0.38$. Results from FMT (dash-dotted purple line) are compared to BD simulation (full green line). Panel (a) shows the radial distribution function on a linear scale. Panel (b) shows the deviation $\ln(r\,|g(r)-1|/\sigma)$ from the bulk value on a logarithmic scale. Here, many correlation shells can be seen. The envelope (thin blue line) of the maxima of the shells follows an exponential law.

aligns. We obtain values of $\tilde{\alpha}_0 \approx 1.0\sigma^{-1}$ and $\tilde{\alpha}_1 \approx 6.4\sigma^{-1}$. The correlation shells are spaced apart by a distance $2\pi/\tilde{\alpha}_1 \approx 1.0\sigma$. These values coincide closely with literature values $\tilde{\alpha}_0 \approx 0.97\sigma^{-1}$ and $\tilde{\alpha}_1 \approx 6.45\sigma^{-1}$ [88], obtained at a density of $\rho = 0.75\sigma^{-3}$, similar to our bulk density $\rho = 0.73\sigma^{-3}$.

The agreement between $g(r)$ obtained with BD simulation and obtained with FMT in the present test particle setup is excellent, as expected for the White Bear Mk. 2 excess free energy functional [38].

3.2 Dynamic Structural Decay

3.2.1 Self Correlations

The self part $G_s(r,t)$ of the van Hove function at $t = 0$ is equal to a Dirac delta distribution localised at the origin of the coordinate system, cf. Eq. (8). Over time, the distribution widens and it attains the shape of a bell curve (see figure 2). In a freely diffusing system without interparticle interactions, the density distribution is given by a Gaussian,

$$f_G(r,t) = (2\pi\sigma^2(t))^{-\frac{3}{2}} \exp\left(-\frac{r^2}{2\sigma^2(t)}\right), \tag{60}$$

with time-dependent variance $\sigma^2(t)$, for which the relation

$$\sigma^2(t) = 2Dt, \tag{61}$$

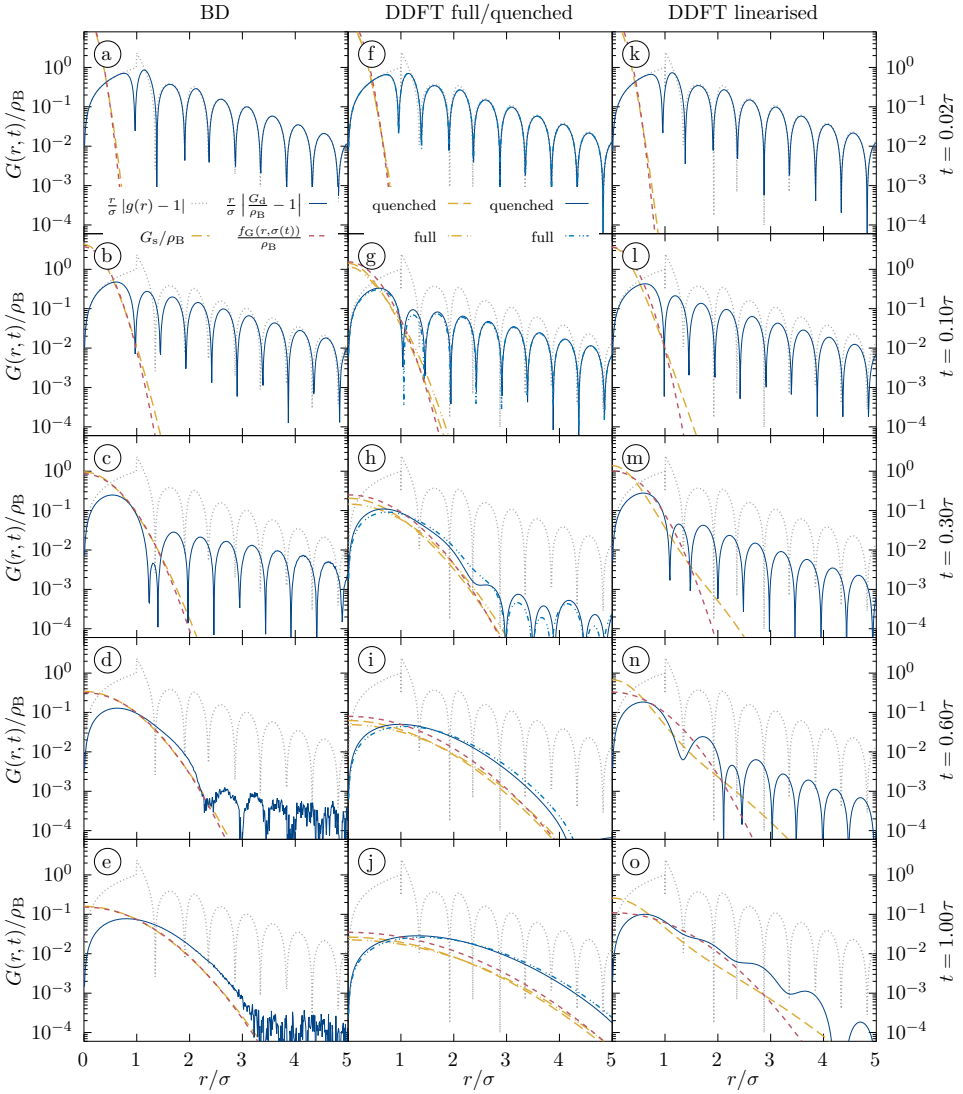

Figure 2: Self (yellow dashed lines) and distinct (solid blue lines) part of the van Hove correlation function $G(r,t)$ at different times t, with radial distribution function $g(r)$ (dotted grey lines) and Gaussian $f_G(r,\sigma(t))$ (dash-dotted red lines) with mean square displacement $\langle r^2 \rangle = 3\sigma^2$ fitted to match that of the self correlation. Results from BD (left column, panels (a) – (e)) are compared to DDFT with full and quenched excess free energy functional (middle column, panels (f) – (j)) and to DDFT with partially linearised excess free energy functional (right column, panels (k) – (o)). The maxima of the solid line correspond to the local extrema of the distinct van Hove function. The first maximum of $r\,|G_d(r,t)/\rho_B - 1|$ always corresponds to a minimum of $G_d(r,t)$.

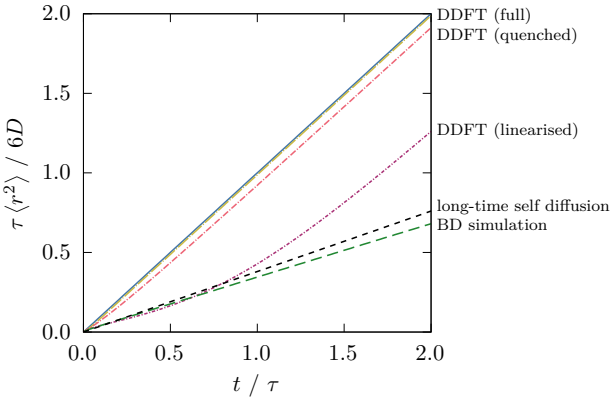

Figure 3: Mean square displacement $\langle r^2 \rangle \tau / 6D$ as a function of time t/τ of the self component of the van Hove function. Data is shown from BD simulation (green long dashes) and from DDFT with the full (yellow long dot-dashes), quenched (red medium dot-dashes) and partially linearised (purple short dot-dashes) excess free energy functional. Additionally, we show the long-time self diffusion (black short dashes) as calculated from our PFT approximation (57). As a reference, the linear law of ideal diffusion (blue solid line) is also plotted.

holds [3]. To relate the shape of $G_s(\mathbf{r}, t)$ in the interacting system to (60), we calculate the mean square displacement at time t via

$$\langle r^2(t) \rangle = \int \mathrm{d}\mathbf{r}\, r^2 G_s(r, t), \tag{62}$$

and compare to an equivalent Gaussian of the form (60) with variance chosen such that

$$\sigma^2(t) = \frac{1}{3} \langle r^2(t) \rangle . \tag{63}$$

We perform this analysis with data both from BD simulation and from DDFT calculations. For BD, the difference between $G_s(r, t)$ and the equivalent Gaussian is minimal, see figure 2 (a) – (e). In DDFT using either the full or the quenched functionals, although the shape of $G_s(r, t)$ is also Gaussian, see figure 2 (f) – (j), the resulting variance is significantly different from the BD results at the same time t. The full and the quenched functionals give very similar results, with no major improvement occurring upon using the quenched approach. When plotting the mean square displacement against time, we see that $G_s(r, t)$ as approximated by these functionals behaves much closer to ideal diffusion than to the BD simulation, see figure 3. We recall that this behaviour is consistent with the absence of superadiabatic effects in the DDFT.

The shape of the self van Hove function in DDFT using the partially linearised functional shows major deviations from a Gaussian, see figure 2 (k) – (o). The distribution is both more strongly localised at the origin and it has a significantly longer tail at large distances, compared to a Gaussian with identical mean square displacement. For $t \leq \tau$, the mean square displacement is much closer to BD simulation than with either the full or quenched functional, but it deviates strongly for $t > \tau$ with a slope approaching that of ideal diffusion, see figure 3. While the mean square displacement as a metric might suggest otherwise, the deviations in the shape of $G_s(r, t)$ make the linearised modification unfit as an improvement over an approach that does not correct at all for self interactions.

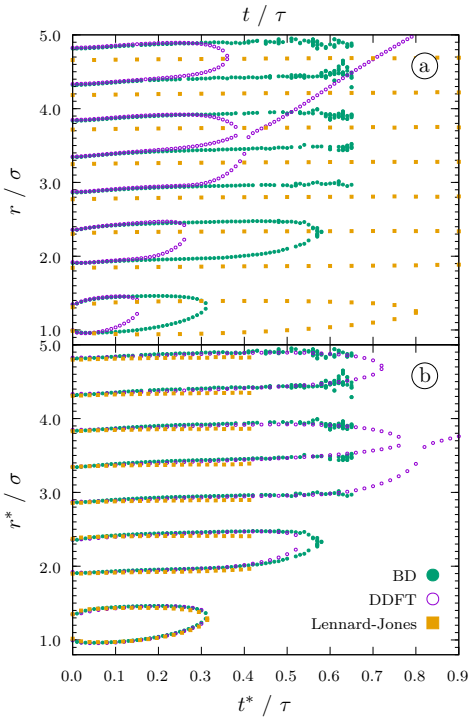

Figure 4: Zeros of $r\left(\frac{G_d(r,t)}{\rho_B}-1\right)$ as a function of time. Data from BD simulation (green, suppressed for $t > 0.65\tau$ due to noise), DDFT with the quenched functional (purple), and results for the Lennard-Jones liquid (yellow). Panel (a) shows the data unmodified, whereas in panel (b), time t and distance r have been rescaled to allow for a comparison of the qualitative behaviour. Here the rescaled quantities are marked by an asterisk and the rescaling is such that $t = t^*$, $r = r^*$ for hard sphere BD simulation, $2t = t^*$ and $r = r^*$ for hard sphere DDFT, and $t/2.55 = t^*$ and $1.03r = r^*$ for the Lennard-Jones liquid,

3.2.2 Distinct Correlations

Figure 2 shows also a comparison of BD and DDFT results for the dynamic decay of the distinct part of the van Hove function. The temporal decay consists of two stages, namely of an initial deconfinement and of a subsequent outward drift of correlation shells: First, particles diffuse out of the high density regions into the neighbouring minima. Thus, both maxima and minima become less pronounced. However, this process is not equally rapid everywhere. Inner shells, i.e. those that are close to the test particle, decay at earlier times than do outer shells. As the test particle, whose confinement at the origin caused the appearance of the shell structure in the first place, diffuses away from the origin, the particles of the first correlation shell start to drift closer to the origin, which in turn allows the second shell to expand inwards, and so on for further shells. Thus, inner shells decay in an expanding region around the origin, while outer shells remain stable for a longer time. This mechanism results in an additional lengthscale for the spatial decay of the inner shells, while the decay length of the outer shells remains equal to the static decay length of $g(r)$. This dynamic scenario has also been found for the Lennard-Jones liquid by Schindler and Schmidt [51], who reported that for the Lennard-Jones liquid the new, dynamic decay length increased, starting from the static decay length, up until

$t = 0.7\tau$, where it reached a plateau value. Here we find an increase of the dynamic decay length up until at least $t = 0.3\tau$, but cannot identify a plateau value, due to numerical noise and possibly a somewhat smaller system size.

The second stage of decay is caused by the test particle diffusing out of its initial position, thus creating space for distinct particles to come closer to the origin. The particles essentially flow into the initial cavity, which swallows correlation shells from the inside out. In this second regime, the distinct correlations decrease monotonically and faster than exponential with distance. This second stage of dynamic decay has not been explicitly mentioned in Ref. [51], but can be seen in figure 3 of that paper, where the first maximum of $G_\mathrm{d}(r,t)$ decreases in amplitude and then melts into the minimum at the origin.

Additionally to the above effects, we observe an outward drift of the correlation shells, which seems to be hitherto unreported. We analyse the locations of the zeros of $r\left(\frac{G_\mathrm{d}(r,t)}{\rho_\mathrm{B}}-1\right)$ as a function of time; results are shown in figure 4. We observe a slow, close to linear in time, drift of the inner zeros with a drift speed of $(0.24\pm0.01)\sigma/\tau$, up to the point where the corresponding shell is swallowed by the central cavity and the corresponding zeros disappear. By analysing $G_\mathrm{d}(r,t)$ for the Lennard-Jones liquid at temperature $T = 0.8\epsilon/\mathrm{k_B}$ and density $\rho = 0.84/\sigma_\mathrm{LJ}^3$, we observe a similar, but much slower drift of $(0.037\pm0.001)\sigma/\tau$ (see figure 4). A rescaling of time and distance, shown in panel (b) of figure 4, shows that the behaviour of the zeros of the van Hove function of the Lennard-Jones liquid is qualitatively very similar to the behaviour of the hard sphere liquid. These findings suggest that the mechanism of dynamic decay presented here and by Schindler and Schmidt is, at least qualitatively, universal for particles with repulsive interactions and overdamped dynamics.

The behaviour described above is qualitatively reproduced by DDFT, based on either the full or the quenched approach. Both functionals yield results that well represent the shape of $G_\mathrm{d}(\mathbf{r},t)$, but overestimate the rate of temporal decay by roughly a factor of two (compare e.g. figure 2-(d) and 2-(h) and recall the time rescaling in figure 4-(b)). The differences of results from the full and quenched approach are minor, though. In contrast, the shell deconfinement as predicted with the linearised functional is slower than in BD. This is despite the fact that the diffusion of the self correlation is faster than in BD. However, this may be due to the stable inner peak of the self correlation, which in turn could stabilise the shell structure. Additionally, the shape of $G_\mathrm{d}(\mathbf{r},t)$ shows intermittent behaviour which is not observed at all in the time evolution in BD, see e.g. figure 2-(o). These results substantiate the finding that the partial linearisation approach is not well suited to fix the self interaction problem.

It should be noted that all of the three excess free energy functionals studied produce identical adiabatic forces on the distinct density component, given the same input density. Yet, the time evolution of the distinct density component is significantly different between the three cases, which must therefore be caused by the difference in the time evolution of the self density component. Thus, the correct handling of self-interactions of the self density is not a minor detail, but rather a central requirement for test particle DFT.

Lastly, we observe that at time $t \approx 0.4\tau$, all but one zero of $r\left(\frac{G_\mathrm{d}(r,t)}{\rho_\mathrm{B}}-1\right)$ disappear in our DDFT results (see figure 4). This disappearance constitutes the crossover to the long time regime discussed in section 2.6. The negative deflection in ρ_d at small r is the hole occupied by the self particle. The positive value of $r(G_\mathrm{d}(r,t)/\rho_\mathrm{B}-1)$ at distances larger than the zero is caused by adhesion of distinct particles around the self particle in the initial condition. It depends on the static structure factor of the fluid in sign and magnitude. Diffusion of this excess part has been studied in a time-dependent setup [89, 90]. We neglect this effect in section 2.6 as it is smaller than the hole of the self particle by a factor of ~ 40.

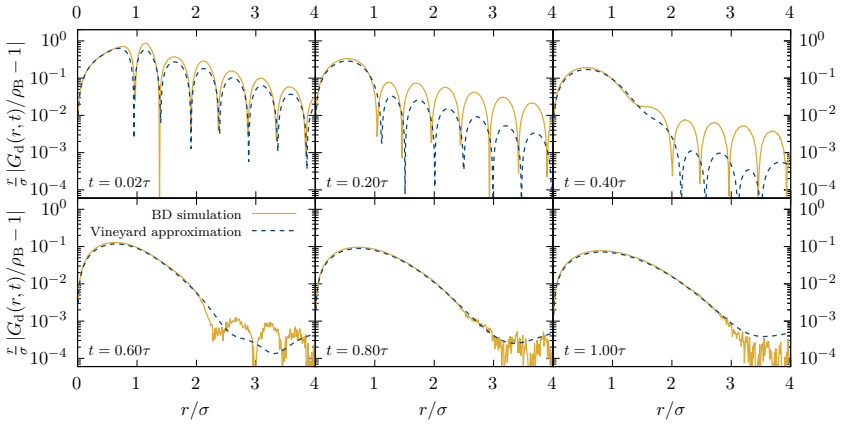

Figure 5: Comparison of the distinct van Hove function $G_d(\mathbf{r}, t)$, obtained directly using BD simulation (solid yellow lines) and obtained from simulation data using the Vineyard approximation (dashed blue lines).

3.2.3 Vineyard Approximation

One early attempt at a theoretical approximation for the van Hove function was presented by Vineyard [3, 91]. He proposed the relation

$$G_d(\mathbf{r}, t) \approx (g(\check{\mathbf{r}}) * G_s(\check{\mathbf{r}}, t))(\mathbf{r}), \tag{64}$$

where the operator $*$ indicates a convolution, between the self component and the distinct component of the van Hove function. Hopkins et al. found that the Vineyard approximation to be a 'fairly good approximation' of the van Hove function [47]. As a self-consistency check, we use our simulation data to calculate the convolution in equation (64) and compare the result to the simulation result for $G_d(\mathbf{r}, t)$ (see figure 5). We find that the Vineyard approximation significantly overestimates the rate of decay of the shell structure of the distinct van Hove function, in accordance with previous findings [47]. Only the minimum at small distances r is well reproduced. This indicates that, even if we had a perfect approximation of the behaviour of the self component of the van Hove function, we could not use the Vineyard approximation to obtain an equally accurate approximation of the distinct van Hove function.

3.3 Adiabatic Forces

We next analyse the forces that govern the time evolution of the van Hove function. The full internal force field for both the self and the distinct component can be calculated from BD simulation data from the species-resolved current profiles $\mathbf{J}_\alpha(\mathbf{r}, t)$ via (15). To split the internal force field into adiabatic and superadiabatic forces, we need to first calculate the adiabatic forces. In section 3.2, we have compared results from three different free energy functional approximations which produce adiabatic forces in the framework of DDFT. To test whether these functionals are accurate, we calculate the adiabatic potential

$$V_{\mathrm{ad},\alpha}(\mathbf{r}, t) = \mu - \frac{\delta F[\rho_s, \rho_d]}{\delta \rho_\alpha(\mathbf{r}, t)}, \tag{65}$$

using each of the three free energy functionals, with the density profiles sampled in BD simulation at times $t = 0.1\tau, 0.3\tau, 0.6\tau$ and 1.0τ. Then, we run equilibrium BD simulations with an

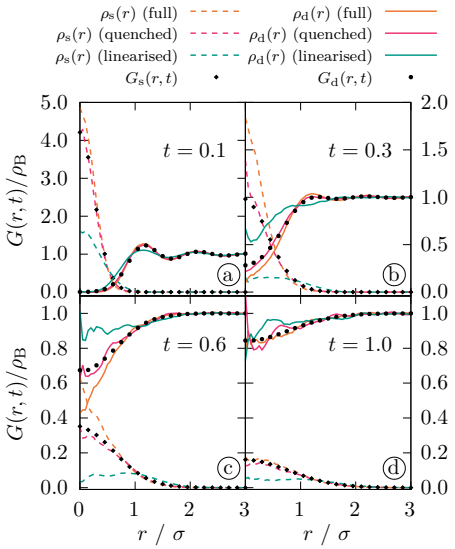

Figure 6: Self and distinct parts of the van Hove function $G_s(r,t)$ (black discs), $G_d(r,t)$ (black diamonds) as a function of distance r, from BD simulation, at times t as indicated. Density profiles $\rho_\alpha(r)$ from test particle equilibrium BD simulation (self part: dashed lines, distinct part: solid lines) with adiabatic forces from DFT with full (orange), quenched (magenta) and partially linearised (teal) excess free energy.

external force field $\mathbf{f}_{\text{ext},\alpha}(\mathbf{r},t) = -\nabla V_{\text{ad},\alpha}(\mathbf{r},t)$ designed to cancel out the predicted adiabatic internal force field [65, 67]. We sample equilibrium density profiles from these simulations and compare them to the initial $G_\alpha(\mathbf{r},t)$ profiles. If the given functional produces accurate adiabatic forces, then the resulting density profiles should be identical to the original input.

The results, shown in figure 6, indicate that both the full and the partially linearised excess free energy functional yield density profiles that significantly deviate from the target $G_\alpha(\mathbf{r},t)$. For the quenched functional, the agreement is markedly improved, but relevant deviations remain near the origin. As we will see below, the forces calculated in this region, via the quenched functional, are still not reliable enough to facilitate an accurate splitting of the internal forces into adiabatic and superadiabatic contributions (see figure 7, panel b). In order to circumvent this problem, we iteratively calculate the species-resolved adiabatic external potential for the chosen times, using equilibrium Monte Carlo simulations. To ensure consistency, we choose the same number of particles and system dimensions as the BD simulations. The gradient of the calculated external potentials gives us the adiabatic force fields via (19), and by extension the superadiabatic forces via (17).

We examine the ideal, adiabatic and superadiabatic force fields as a function of time (see figure 7). The largest force contribution arises from the ideal diffusion, which always acts to smooth out any density inhomogeneity. Both the adiabatic and superadiabatic force mainly oppose this relaxation process. Notably, at $t \geq \tau$ the adiabatic force field is small compared to both the ideal and the superadiabatic force field. Thus, DDFT, which by construction neglects superadiabatic contributions, must fail to describe the long-time behaviour of the van Hove function, even if adiabatic forces were included with perfect accuracy. This explains why the long-time diffusion of the self component tends to ideal diffusion for all studied DDFT approximations (see figure 3). Additionally, we can see in panel b of figure 7 that even the quenched approximation for the adiabatic force density shows some deviations in the distinct compon-

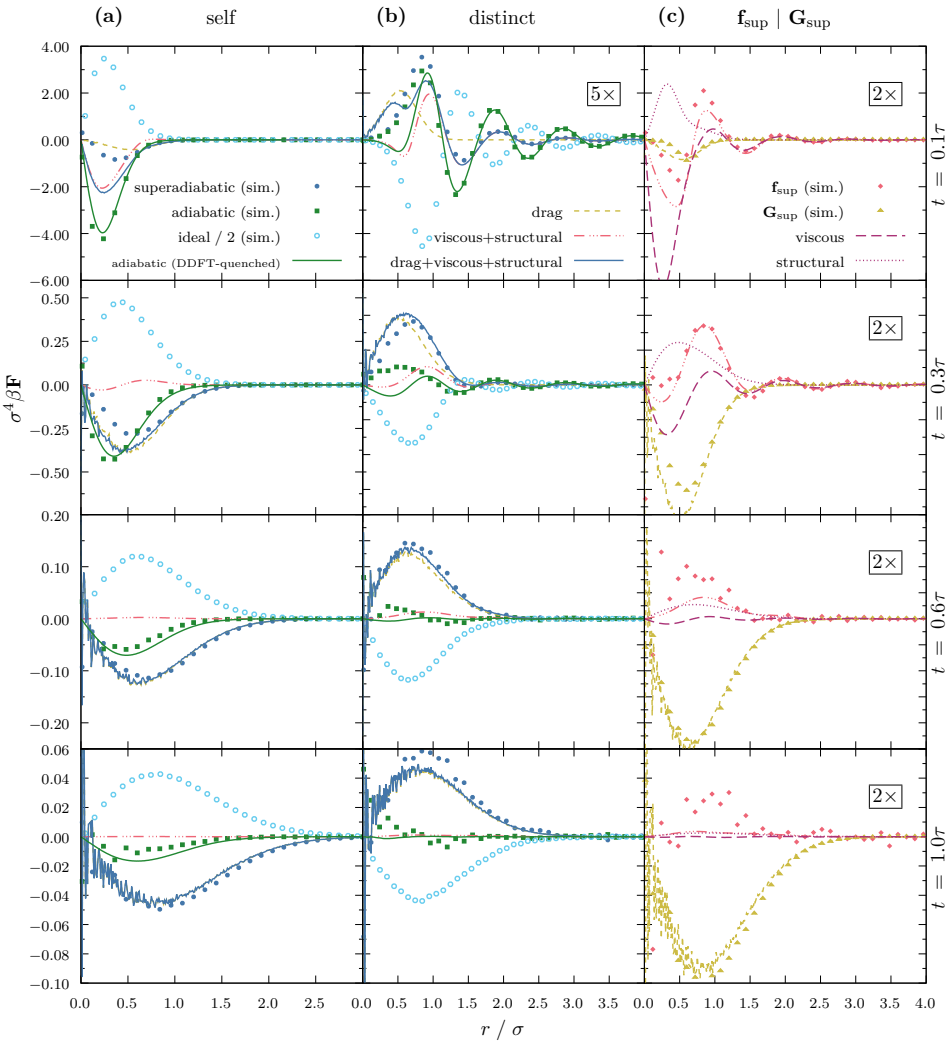

Figure 7: A comparison of forces and force densities from simulation (symbols) and DDFT/PFT approximation (lines). Lines and symbols coloured identically show the same measured quantity. **(a, b)**: Ideal (light blue, empty circles), adiabatic (green, squares) and superadiabatic (dark blue, solid circles) force density for the self (a) and distinct (b) component of the van Hove function as a function of distance r for different times t, as measured in BD simulation. The quenched functional approximation for the adiabatic force density is shown as a solid green line. Shown as a dark blue solid line is the PFT approximation for the superadiabatic force density, consisting of a drag component (dashed yellow line) and the viscous plus structural component (dash-dotted red line). **(c)**: Splitting of superadiabatic forces into total force $\mathbf{f}_{\text{sup}}$ (red diamonds) and differential force density $\mathbf{G}_{\text{sup}}$ (yellow triangles) as a function of distance r at different times t. We also show the different force components of our approximation, consisting of drag (dashed yellow line), viscosity (long-dashed purple line) and a structural force (dotted purple line). The drag component acts purely differentially, whereas viscosity and the structural component act purely as a total force

ent near the origin. These deviations are of similar magnitude as the force itself and may thus not be neglected when trying to split the internal force field into adiabatic and superadiabatic contributions. However, we see that the distinct force density component for $r > \sigma$, as well as the self component, are accurately reproduced.

3.4 Superadiabatic Forces

In Sec. 2.5 we have described a kinematic approximation for the superadiabatic forces, that include three distinct physical effects: a viscoelastic force, a structural force and a drag force. With the density and current profiles from BD simulation as input, we can use this theory to calculate both the total force field and the differential force density field via (46) and (47). Crucially, the drag force (42) is the sole contribution to the differential superadiabatic force density $\mathbf{G}_{\text{sup}}(\mathbf{r}, t)$, see (47). Recall that the drag force arises from the opposing motion of the two species.

In practice, we perform a least squares fit of the differential force density calculated using (47) against the corresponding measured BD simulation data. Thereby we identify the free parameter in Eq. (37) as $C_{\text{drag}} \approx 2.2 k_B T \tau \sigma$. The quantitative agreement with $\mathbf{G}_{\text{sup}}(\mathbf{r}, t)$ is excellent for $t \geq 0.6\tau$, but minor deviations are apparent at earlier times. The fact that both the shape of $\mathbf{G}_{\text{sup}}(\mathbf{r}, t)$ as well as the scaling with time are well represented by the drag functional constitutes strong evidence that drag is the relevant physical effect which governs the differential superadiabatic force density. The differential drag force density is quite simple in shape, making it almost a trivial contribution to the dynamics of the van Hove function, see figure 7. One could argue that the real complexity of the system therefore lies in the behaviour of the total van Hove function, and hence in the total force field.

We model the total force component based on the viscoelastic (36) and structural (38) functionals (see Eq. (46)). The parameters of the memory kernel in (36) were determined via an examination of a sheared system of hard spheres in [58], at identical bulk density, as $\tau_M^{\text{visc}} \approx 0.02\tau$ and $D_M^{\text{visc}} \approx 5.6\sigma^2/\tau$. We apply those same parameters here, see figure 7, and find that the viscoelastic functional produces a spatially oscillating force field, which represents the total force profile well for $r > 1.5\sigma$. This oscillation decays rather quickly compared to the other force components and it is lost in the statistical noise at $t > \tau$. We determine the prefactor of the viscoelastic functional via a least squares fit to BD simulation data and obtain $C_{\text{visc}} \approx 5.8 k_B T/(\tau\sigma^3)$. In addition to the oscillations of the viscoelastic force, the total force profile shows a larger peak at $r \approx \sigma$, which is produced in our approximation by the structural force. Since we have no prior information about this force, we determine its memory time $\tau_M^{\text{struc}} \approx 0.3\tau$ and the memory diffusion constant $D_M^{\text{struc}} \approx 0.35\sigma^2/\tau$, as well as the prefactor $C_{\text{struc}} \approx 0.42 k_B T \tau^2/\sigma$, via a least squares fit to BD results. The obtained memory time is larger than that for the viscoelastic force by more than an order of magnitude. Therefore, the structural force is much more long-lived than the viscoelastic force and persists, though with decreased amplitude, even at $t = \tau$.

Together, the sum of the structural and the viscoelastic force is in very good agreement with the total force profile from simulation for times $t > 0.3\tau$. For earlier times $t < 0.3\tau$, quantitative deviations occur, but the spatial shape is still qualitatively reproduced. The deviation between our power functional approximation and the forces in simulation for early times are most likely a result of both the extreme inhomogeneity of the density profile at early times, as well as of the large local velocities that occur in this regime.

We noted above that the adiabatic force field for $t > \tau$ is small compared to both the superadiabatic and the ideal force field, see also figure 7. The superadiabatic force field is dominated by the drag force at $t > \tau$. This situation allows us to predict the long-time diffusion constant of the self peak of the van Hove function via the modified Einstein relation (57), since the assumptions made in Sec. 2.6 hold to a large degree. For our system, we obtain

$D_L = \frac{k_B T}{\gamma + C_{drag}\rho_B} \approx 0.38\sigma^2/\tau$, using the value given above for $C_{drag} = 2.2 k_B T \tau\sigma$. We determine the long-time diffusion coefficient from the asymptotic slope of the mean square displacement of the self density profile in BD simulation and obtain $D_L \approx 0.32\sigma^2/\tau$, which corresponds to a value of $C_{drag} \approx 2.9 k_B T \tau\sigma$. These results are in reasonable agreement (see also figure 3), but indicate that our value for $C_{drag} \approx 2.2 k_B T \tau\sigma$ obtained above might be an underestimate. Fitting the drag amplitude only to the largest times results in $C_{drag} \approx 2.4 k_B T \tau\sigma$, from which we obtain $D_L \approx 0.36\sigma^2/\tau$, improving the match with the simulation result. This finding indicates that the differential force field contains contributions for early times $t < \tau$ which are not captured well by our approximation for the drag force.

Hence the results shown in figure 7 demonstrate explicitly the perhaps expected shortcoming of the DDFT that it does not capture the full dynamics of the system. Here the van Hove function plays a dual role in that it is both an equilibrium dynamical correlation function as well as a specific nonequilibrium temporal process. The latter is specified by the dynamical test particle limit and we recall our description of how this approach allows to identify two- with one-body correlation functions in section 2.3. As the DDFT does not provide the full nonequilibrium dynamics on the one-body level, by extension it also fails to describe all forces that govern the time evolution of the van Hove function. These findings are consistent with the nonequilibrium Ornstein-Zernike framework [41, 42], where both adiabatic and superadiabatic direct correlation functions occur, and only the former are generated from the free energy density functional. The superadiabatic time direct correlation functions are genuine dynamical objects. The present study sheds light on this issue in the test particle picture.

4 Conclusion and outlook

We have studied the van Hove correlation function of the Brownian hard sphere liquid using BD simulations. We have also calculated the van Hove function using test particle DDFT and analysed the interparticle force field using PFT. Our analysis of the dynamic decay of the distinct van Hove function shows a two-stage process. The initial deconfinement of correlation shells leads to an intermediate dynamic decay length, which is followed by a monotonic spatially super-exponential decay as the self component mixes with the distinct component. Additionally, correlation shells drift slowly outward from the origin. A comparison with results for the overdamped Lennard-Jones liquid shows that, qualitatively, the same effects occur in both systems. This, together with the fact that the behaviour of the hard sphere liquid is prototypical for a wide range of liquids, indicates that these results reflect fundamental effects in the dynamics of the liquid state.

We have discussed the accuracy of the Vineyard approximation on the basis of our simulation data. Whether the Vineyard approximation can form a useful ingredient in the study of superadiabatic effects in the van Hove function remains to be seen.

We have analysed adiabatic forces in the dynamic decay of the van Hove correlation function using Monte Carlo simulation and the adiabatic construction. This analysis showed that the quenched excess free energy functional presented by Stopper et al. [56] is the best currently available approximation for adiabatic forces in the test particle picture. The remaining deviations are however severe enough to warrant further development of the theory. One possible path for investigation is canonical decomposition as presented by de las Heras and Schmidt [92]. On the conceptual level, investigating the relationship of the theory of ref. [56] to the DFT for quenched-annealed mixtures [93, 94] would be interesting.

We have isolated superadiabatic forces, which showed that, even assuming very accurate approximation of adiabatic forces, DDFT is inadequate to quantitatively describe the dynamic decay of the van Hove function, since superadiabatic forces play a major role in the time

evolution of both the self and the distinct density components. The long-time behaviour of the DDFT approximation for $G_s(\mathbf{r}, t)$ approaches ideal diffusion, since adiabatic forces vanish at long times.

Using PFT, we have demonstrated the splitting of the superadiabatic force into a viscoelastic force, a drag force between the two different components of the van Hove function, and a structural force. These three force contributions dominate the superadiabatic force field for $t > 0.3\tau$. Approximations for these forces were previously developed for nonequilibrium dynamics. Their occurrence in the dynamics of the van Hove function shows a deep connection between nonequilibrium forces and equilibrium dynamics. The differential force density acting between the two components of the van Hove function is much simpler and easier to approximate than the forces governing the evolution of the total van Hove function. In the long-time tail of the van Hove function, adiabatic contributions to the interparticle force field vanish, as do the viscoelastic and structural superadiabatic force contributions. Thus, the drag force determines the slowing-down of the long-time self diffusion of the hard sphere liquid. The long-time self diffusion constant calculated using our approximation is consistent with our direct BD simulation results.

Overall, our approximation has seven free parameters. Out of these, two, namely the memory time and memory diffusion constant of the viscoelastic force, have been determined previously for a system of hard spheres under a shear force [58]. The remaining five parameters have been determined via a least-squares fit to simulation data. Conceptually, these parameters take the role of transport coefficients. A goal of future investigations would be to derive these coefficients from first principles. Furthermore, investigating the effects of external driving such as shear, see [95] for a mode-coupling study of glassy states, would be worthwhile, as would be to relate to the stress correlation function [96].

Describing the short-time behaviour of the van Hove function remains a significant challenge. Improvement of our approximation could potentially be achieved by augmenting the dependence on the weighted density $n_3(\mathbf{r}, t)$ by incorporating further fundamental measure weighted densities. Additionally, the functionals that we apply here can be viewed as a low-order series expansion in powers of the velocity field. Since the velocity field is very large at early times compared to later times, functionals with higher orders of $\mathbf{v}$ might be needed to achieve better agreement in this regime.

Conflicts of interest

There are no conflicts of interest to declare.

Acknowledgements

We thank Daniel de las Heras, Roland Roth and Daniel Stopper for useful comments. This work is supported by the German Research Foundation (DFG) via Project no. 317849184.

A DDFT integration scheme in spherical coordinates

We derive a discrete integration scheme in spherical coordinates as used in our implementation starting from the DDFT equation of motion (23). We set $f_{\text{ext},\alpha} = 0$ and divide by γ to obtain

$$\dot{\rho_\alpha}(\mathbf{r},t) = D\nabla^2\rho_\alpha(\mathbf{r},t) + \nabla\cdot\gamma^{-1}\rho_\alpha(\mathbf{r},t)\nabla\frac{\delta F_{\text{exc}}[\{\rho_\alpha\}]}{\delta\rho_\alpha(\mathbf{r},t)}. \tag{66}$$

For compactness of notation, we define the excess current profile

$$\mathbf{J}_{\text{exc},\alpha}(\mathbf{r},t) = -\gamma^{-1}\rho_\alpha(\mathbf{r},t)\nabla\frac{\delta F_{\text{exc}}[\{\rho_\alpha\}]}{\delta\rho_\alpha(\mathbf{r},t)}, \tag{67}$$

which is a functional of ρ_α. Using this, we can write equation (66) as

$$\dot{\rho_\alpha}(\mathbf{r},t) = D\nabla^2\rho_\alpha(\mathbf{r},t) - \nabla\cdot\mathbf{J}_{\text{exc},\alpha}(\mathbf{r},t). \tag{68}$$

In our system, where ρ_α is radially symmetric, the excess current profile can be written as

$$\mathbf{J}_{\text{exc},\alpha}(\mathbf{r},t) = J_{\text{exc},\alpha}(r,t)\hat{\mathbf{e}}_r. \tag{69}$$

Equation (68) then simplifies to

$$\dot{\rho}_\alpha(r,t) = D\frac{1}{r^2}\frac{\partial}{\partial r}\left(r^2\frac{\partial}{\partial r}\rho_\alpha(r,t)\right) - \frac{1}{r^2}\frac{\partial}{\partial r}\left(r^2 J_{\text{exc},\alpha}(r,t)\right). \tag{70}$$

In a numerical calculation, $\rho_\alpha(r,t)$ and $J_{\text{exc},\alpha}$ can be represented as arrays of numbers corresponding to equally spaced sampling points of the respective continuous function. We choose some discretisation step $\Delta r \ll \sigma$ in space and some discretisation time $\Delta t \ll \tau$. We can then approximate the density profile as

$$\rho_\alpha(r,t_k) \approx \tilde{\rho}_\alpha(r,t_k) \equiv \sum_{i=0}^{\infty}\rho_{i,k}^{\alpha}\, b\left(r - i\Delta r\right), \tag{71}$$

where i is a spatial index, k is a temporal index, and $b(r)$ is a triangle function defined as

$$b(r) = \begin{cases} 1 + r/\Delta r & \text{for } -\Delta r \le r \le 0 \\ 1 - r/\Delta r & \text{for } 0 \le r \le \Delta r \\ 0 & \text{elsewhere.} \end{cases} \tag{72}$$

The same discretisation procedure can be done for the current profile. The spatial and temporal derivatives in (70) can be evaluated using the well-known finite difference formulae to obtain an approximate solution to the partial differential equation (70) for a given initial value for $\rho_\alpha(\mathbf{r},t)$:

$$\begin{aligned}\rho_{i,k+1}^{\alpha} =& \rho_{i,k}^{\alpha} - \Delta t\left[\frac{2}{i\Delta r}J_{i,k}^{\text{exc},\alpha} + \frac{J_{i+1,k}^{\text{exc},\alpha} - J_{i-1,k}^{\text{exc},\alpha}}{2\Delta r}\right. \\ &\left. + D\left(\frac{\rho_{i+1,k}^{\alpha} - 2\rho_{i,k}^{\alpha} + \rho_{i-1,k}^{\alpha}}{\Delta r^2} + \frac{\rho_{i+1,k}^{\alpha} - \rho_{i-1,k}^{\alpha}}{i\Delta r^2}\right)\right].\end{aligned} \tag{73}$$

However, using this straightforward approach results in a subtle problem: particle conservation is violated. This can be seen by integrating the difference $\tilde{\rho}_\alpha(r,t_{k+1}) - \tilde{\rho}_\alpha(r,t_k)$ from $r = 0$ to some cutoff r_{max} and reordering the resulting sum by the spatial index i. The result

is nonzero and, more importantly, it is not equal to the total particle flux through the surface at $r = r_{\max}$.

This defect can be addressed by re-writing equation (70) with respect to the functions

$$R_\alpha(r,t) \equiv 4\pi r^2 \rho_\alpha(r,t) \text{ and} \tag{74}$$
$$J^R_\alpha(r,t) \equiv 4\pi r^2 J_{\text{exc},\alpha}(r,t), \tag{75}$$

which represent the radial density in and current through the whole spherical shell around the origin at r. Thereby, we obtain a new partial differential equation

$$\dot{R}_\alpha(r,t) = D\frac{\partial^2}{\partial r^2}R_\alpha(r,t) - D\frac{\partial}{\partial r}\left(\frac{2R_\alpha(r,t)}{r}\right) - \frac{\partial}{\partial r}J^R_\alpha(r,t), \tag{76}$$

which can be discretised using standard finite differences to obtain the iteration scheme

$$R^\alpha_{i,k+1} = R^\alpha_{i,k} + \frac{D\Delta t}{\Delta r}\left[\frac{R^\alpha_{i+1,k} - 2R^\alpha_{i,k} + R^\alpha_{i-1,k}}{\Delta r} - \frac{R^\alpha_{i+1,k}}{(i+1)\Delta r} + \frac{R^\alpha_{i-1,k}}{(i-1)\Delta r} - \frac{J^{R,\alpha}_{i+1,k} - J^{R,\alpha}_{i-1,k}}{2D}\right], \tag{77}$$

where $R^\alpha_{i,k}$ and $J^{R,\alpha}_{i,k}$ are defined as

$$R^\alpha_{i,k} \equiv 4\pi(i\Delta r)^2 \rho^\alpha_{i,k} \text{ and} \tag{78}$$
$$J^{R,\alpha}_{i,k} \equiv 4\pi(i\Delta r)^2 J^{\text{exc},\alpha}_{i,k}. \tag{79}$$

Using this scheme significantly reduces the deviations in the normalisation of the density profile which we observed in our simulations.

At each time step, the transformation from $\rho^\alpha_{i,k}$ to $R^\alpha_{i,k}$ needs to be inverted in order to calculate $\mathbf{J}_{\text{exc},\alpha}$. The same is necessary if the density profile should be saved to disk in a simulation run. This results in a division by zero for $\rho^\alpha_{0,k}$. To circumvent this issue, we define $\rho^\alpha(0,t)$ as the continuous continuation of $R_\alpha(r,t)/r^2$ to $r = 0$. In practice, we extrapolate from $\rho^\alpha_{1,k}$ and $\rho^\alpha_{2,k}$ logarithmically:

$$\rho^\alpha_{0,k} \approx \exp\left[\left(4\ln\rho^\alpha_{1,k} - \ln\rho^\alpha_{2,k}\right)/3\right]. \tag{80}$$

We note that after the inverted transformation, the density normalisation of $\rho^\alpha_{0,k}$ is not strictly conserved either. However, the shell normalisation of $R^\alpha_{0,k}$ is conserved which prevents the drift of the density normalisation, which occurs in the integration scheme equation (73). The full implementation of this integration scheme [97] is available as open source software. We encourage the interested readers to examine and extend it for their own research.

References

[1] L. van Hove, *Correlations in space and time and born approximation scattering in systems of interacting particles*, Phys. Rev. **95**, 249 (1954), doi:10.1103/PhysRev.95.249.

[2] W. K. Kegel and A. van Blaaderen, *Direct observation of dynamical heterogeneities in colloidal hard-sphere suspensions*, Science **287**, 290 (2000), doi:10.1126/science.287.5451.290.

[3] J.-P. Hansen and I. R. McDonald, *Theory of Simple Liquids*, Academic Press, Oxford, 4th ed. edn., ISBN 978-0-12-387032-2 (2013).

[4] D. Stopper, A. L. Thorneywork, R. P. A. Dullens and R. Roth, *Bulk dynamics of Brownian hard disks: Dynamical density functional theory versus experiments on two-dimensional colloidal hard spheres*, J. Chem. Phys. **148**, 104501 (2018), doi:10.1063/1.5019447.

[5] Y. Shinohara, W. Dmowski, T. Iwashita, D. Ishikawa, A. Q. R. Baron and T. Egami, *Local self-motion of water through the van Hove function*, Phys. Rev. E **102**, 032604 (2020), doi:10.1103/PhysRevE.102.032604.

[6] M. Bier, R. van Roij, M. Dijkstra and P. van der Schoot, *Self-diffusion of particles in complex fluids: Temporary cages and permanent barriers*, Phys. Rev. Lett. **101**, 215901 (2008), doi:10.1103/PhysRevLett.101.215901.

[7] B. Wu, T. Iwashita and T. Egami, *Atomic dynamics in simple liquid: de Gennes narrowing revisited*, Phys. Rev. Lett. **120**, 135502 (2018), doi:10.1103/PhysRevLett.120.135502.

[8] D. Stopper, R. Roth and H. Hansen-Goos, *Structural relaxation and diffusion in a model colloid-polymer mixture: dynamical density functional theory and simulation*, J. Phys.: Condens. Matter **28**, 455101 (2016), doi:10.1088/0953-8984/28/45/455101.

[9] L. Yeomans-Reyna and M. Medina-Noyola, *Overdamped van Hove function of colloidal suspensions*, Phys. Rev. E **62**, 3382 (2000), doi:10.1103/PhysRevE.62.3382.

[10] L. Yeomans-Reyna, H. Acuña-Campa, F. d. J. Guevara-Rodríguez and M. Medina-Noyola, *Self-consistent theory of collective Brownian dynamics: Theory versus simulation*, Phys. Rev. E **67**, 021108 (2003), doi:10.1103/PhysRevE.67.021108.

[11] M. A. Chávez-Rojo and M. Medina-Noyola, *Van Hove function of colloidal mixtures: Exact results*, Physica A **366**, 55 (2006), doi:https://doi.org/10.1016/j.physa.2005.10.048.

[12] L. Yeomans-Reyna, M. A. Chávez-Rojo, P. E. Ramírez-González, R. Juárez-Maldonado, M. Chávez-Páez and M. Medina-Noyola, *Dynamic arrest within the self-consistent generalized Langevin equation of colloid dynamics*, Phys. Rev. E **76**, 041504 (2007), doi:10.1103/PhysRevE.76.041504.

[13] R. Juárez-Maldonado, M. A. Chávez-Rojo, P. E. Ramírez-González, L. Yeomans-Reyna and M. Medina-Noyola, *Simplified self-consistent theory of colloid dynamics*, Phys. Rev. E **76**, 062502 (2007), doi:10.1103/PhysRevE.76.062502.

[14] M. Medina-Noyola and P. Ramírez-González, *Non-equilibrium relaxation and near-arrest dynamics in colloidal suspensions*, J. Phys.: Condens. Matter **21**, 504103 (2009), doi:10.1088/0953-8984/21/50/504103.

[15] P. Ramírez-González and M. Medina-Noyola, *Aging of a homogeneously quenched colloidal glass-forming liquid*, Phys. Rev. E **82**, 061504 (2010), doi:10.1103/PhysRevE.82.061504.

[16] L. López-Flores, L. L. Yeomans-Reyna, M. Chávez-Páez and M. Medina-Noyola, *The overdamped van Hove function of atomic liquids*, J. Phys.: Condens. Matter **24**, 375107 (2012), doi:10.1088/0953-8984/24/37/375107.

[17] L. López-Flores, H. Ruíz-Estrada, M. Chávez-Páez and M. Medina-Noyola, *Dynamic equivalences in the hard-sphere dynamic universality class*, Phys. Rev. E **88**, 042301 (2013), doi:10.1103/PhysRevE.88.042301.

[18] E. Lázaro-Lázaro, P. Mendoza-Méndez, L. F. Elizondo-Aguilera, J. A. Perera-Burgos, P. E. Ramírez-González, G. Pérez-Ángel, R. Castañeda-Priego and M. Medina-Noyola, *Self-consistent generalized Langevin equation theory of the dynamics of multicomponent atomic liquids*, J. Chem. Phys. **146**, 184506 (2017), doi:10.1063/1.4983217.

[19] F. Weysser, A. M. Puertas, M. Fuchs and T. Voigtmann, *Structural relaxation of polydisperse hard spheres: Comparison of the mode-coupling theory to a Langevin dynamics simulation*, Phys. Rev. E **82**, 011504 (2010), doi:10.1103/PhysRevE.82.011504.

[20] D. Lesnicki, R. Vuilleumier, A. Carof and B. Rotenberg, *Molecular hydrodynamics from memory kernels*, Phys. Rev. Lett. **116**, 147804 (2016), doi:10.1103/PhysRevLett.116.147804.

[21] G. Jung and F. Schmid, *Computing bulk and shear viscosities from simulations of fluids with dissipative and stochastic interactions*, J. Chem. Phys. **144**, 204104 (2016), doi:10.1063/1.4950760.

[22] G. Jung, M. Hanke and F. Schmid, *Iterative reconstruction of memory kernels*, J. Chem. Theory Comput. **13**, 2481 (2017), doi:10.1021/acs.jctc.7b00274.

[23] D. Lesnicki and R. Vuilleumier, *Microscopic flow around a diffusing particle*, J. Chem. Phys. **147**, 094502 (2017), doi:10.1063/1.4985909.

[24] G. Jung, M. Hanke and F. Schmid, *Generalized Langevin dynamics: construction and numerical integration of non-Markovian particle-based models*, Soft Matter **14**, 9368 (2018), doi:10.1039/C8SM01817K.

[25] M. E. Fisher and B. Widom, *Decay of correlations in linear systems*, J. Chem. Phys. **50**, 3756 (1969), doi:10.1063/1.1671624.

[26] R. Evans, J. Henderson, D. Hoyle, A. Parry and Z. Sabeur, *Asymptotic decay of liquid structure: oscillatory liquid-vapour density profiles and the Fisher-Widom line*, Mol. Phys. **80**, 755 (1993), doi:10.1080/00268979300102621.

[27] R. Evans, R. J. F. Leote de Carvalho, J. R. Henderson and D. C. Hoyle, *Asymptotic decay of correlations in liquids and their mixtures*, J. Chem. Phys. **100**, 591 (1994), doi:10.1063/1.466920.

[28] C. Grodon, M. Dijkstra, R. Evans and R. Roth, *Decay of correlation functions in hard-sphere mixtures: Structural crossover*, J. Chem. Phys. **121**, 7869 (2004), doi:10.1063/1.1798057.

[29] C. Grodon, M. Dijkstra, R. Evans and R. Roth, *Homogeneous and inhomogeneous hard-sphere mixtures: manifestations of structural crossover*, Mol. Phys. **103**, 3009 (2005), doi:10.1080/00268970500167532.

[30] S. H. L. Klapp, Y. Zeng, D. Qu and R. von Klitzing, *Surviving structure in colloidal suspensions squeezed from 3d to 2d*, Phys. Rev. Lett. **100**, 118303 (2008), doi:10.1103/PhysRevLett.100.118303.

[31] A. Statt, R. Pinchaipat, F. Turci, R. Evans and C. P. Royall, *Direct observation in 3d of structural crossover in binary hard sphere mixtures*, J. Chem. Phys. **144**, 144506 (2016), doi:10.1063/1.4945808.

[32] P. Cats, R. Evans, A. Härtel and R. van Roij, *Primitive model electrolytes in the near and far field: Decay lengths from DFT and simulations*, J. Chem. Phys. **154**, 124504 (2021), doi:10.1063/5.0039619.

[33] N. D. Mermin, *Thermal properties of the inhomogeneous electron gas*, Phys. Rev. **137**, A1441 (1965), doi:10.1103/PhysRev.137.A1441.

[34] R. Evans, *The nature of the liquid-vapour interface and other topics in the statistical mechanics of non-uniform, classical fluids*, Adv. Phys. **28**, 143 (1979), doi:10.1080/00018737900101365.

[35] J. F. Lutsko, *Recent developments in classical density functional theory*, Adv. Chem. Phys. **144**, 1 (2010), doi:10.1002/9780470564318.ch1.

[36] Y. Rosenfeld, *Free-energy model for the inhomogeneous hard-sphere fluid mixture and density-functional theory of freezing*, Phys. Rev. Lett. **63**, 980 (1989), doi:10.1103/PhysRevLett.63.980.

[37] P. Tarazona, J. A. Cuesta and Y. Martínez-Ratón, *Density functional theories of hard particle systems*, In *Theory and Simulation of Hard-Sphere Fluids and Related Systems*, p. 247. Springer, doi:10.1007/978-3-540-78767-9_7 (2008).

[38] R. Roth, *Fundamental measure theory for hard-sphere mixtures: a review*, J. Phys.: Condens. Matter **22**, 063102 (2010), doi:10.1088/0953-8984/22/6/063102.

[39] S. M. Tschopp, H. D. Vuijk, A. Sharma and J. M. Brader, *Mean-field theory of inhomogeneous fluids*, Phys. Rev. E **102**, 042140 (2020), doi:10.1103/PhysRevE.102.042140.

[40] S. M. Tschopp and J. M. Brader, *Fundamental measure theory of inhomogeneous two-body correlation functions*, Phys. Rev. E **103**, 042103 (2021), doi:10.1103/PhysRevE.103.042103.

[41] J. M. Brader and M. Schmidt, *Nonequilibrium Ornstein-Zernike relation for Brownian many-body dynamics*, J. Chem. Phys. **139**, 104108 (2013), doi:10.1063/1.4820399.

[42] J. M. Brader and M. Schmidt, *Dynamic correlations in Brownian many-body systems*, J. Chem. Phys. **140**, 034104 (2014), doi:10.1063/1.4861041.

[43] J. K. Percus, *Approximation methods in classical statistical mechanics*, Phys. Rev. Lett. **8**, 462 (1962), doi:10.1103/PhysRevLett.8.462.

[44] J. Baumgartl, R. P. A. Dullens, M. Dijkstra, R. Roth and C. Bechinger, *Experimental observation of structural crossover in binary mixtures of colloidal hard spheres*, Phys. Rev. Lett. **98**, 198303 (2007), doi:10.1103/PhysRevLett.98.198303.

[45] A. J. Archer, B. Chacko and R. Evans, *The standard mean-field treatment of inter-particle attraction in classical DFT is better than one might expect*, J. Chem. Phys. **147**, 034501 (2017), doi:10.1063/1.4993175.

[46] A. J. Archer, P. Hopkins and M. Schmidt, *Dynamics in inhomogeneous liquids and glasses via the test particle limit*, Phys. Rev. E **75**, 040501 (2007), doi:10.1103/PhysRevE.75.040501.

[47] P. Hopkins, A. Fortini, A. J. Archer and M. Schmidt, *The van Hove distribution function for Brownian hard spheres: Dynamical test particle theory and computer simulations for bulk dynamics*, J. Chem. Phys. **133**, 224505 (2010), doi:10.1063/1.3511719.

[48] U. M. B. Marconi and P. Tarazona, *Dynamic density functional theory of fluids*, J. Chem. Phys. **110**, 8032 (1999), doi:10.1063/1.478705.

[49] A. J. Archer and R. Evans, *Dynamical density functional theory and its application to spinodal decomposition*, J. Chem. Phys. **121**, 4246 (2004), doi:10.1063/1.1778374.

[50] A. Fortini, D. de las Heras, J. M. Brader and M. Schmidt, *Superadiabatic forces in Brownian many-body dynamics*, Phys. Rev. Lett. **113**, 167801 (2014), doi:10.1103/PhysRevLett.113.167801.

[51] T. Schindler and M. Schmidt, *Dynamic pair correlations and superadiabatic forces in a dense Brownian liquid*, J. Chem. Phys. **145**, 064506 (2016), doi:10.1063/1.4960031.

[52] M. Schmidt and J. M. Brader, *Power functional theory for Brownian dynamics*, J. Chem. Phys. **138**, 214101 (2013), doi:10.1063/1.4807586.

[53] J. M. Brader and M. Schmidt, *Power functional theory for the dynamic test particle limit*, J. Phys.: Condens. Matter **27**, 194106 (2015), doi:10.1088/0953-8984/27/19/194106.

[54] J. Reinhardt and J. M. Brader, *Dynamics of localized particles from density functional theory*, Phys. Rev. E **85**, 011404 (2012), doi:10.1103/PhysRevE.85.011404.

[55] D. Stopper, K. Marolt, R. Roth and H. Hansen-Goos, *Modeling diffusion in colloidal suspensions by dynamical density functional theory using fundamental measure theory of hard spheres*, Phys. Rev. E **92**, 022151 (2015), doi:10.1103/PhysRevE.92.022151.

[56] D. Stopper, R. Roth and H. Hansen-Goos, *Communication: Dynamical density functional theory for dense suspensions of colloidal hard spheres*, J. Chem. Phys. **143**, 181105 (2015), doi:10.1063/1.4935967.

[57] L. L. Treffenstädt and M. Schmidt, *Universality in driven and equilibrium hard sphere liquid dynamics*, Phys. Rev. Lett. **126**, 058003 (2021), doi:10.1103/PhysRevLett.126.058002.

[58] L. L. Treffenstädt and M. Schmidt, *Memory-induced motion reversal in Brownian liquids*, Soft Matter **16**, 1518 (2020), doi:10.1039/C9SM02005E.

[59] T. Geigenfeind, D. de las Heras and M. Schmidt, *Superadiabatic demixing in nonequilibrium colloids*, Comm. Phys. **3**, 23 (2020), doi:10.1038/s42005-020-0287-5.

[60] J. C. Dyre, *Simple liquids' quasiuniversality and the hard-sphere paradigm*, J. Phys.: Condens. Matter **28**, 323001 (2016), doi:10.1088/0953-8984/28/32/323001.

[61] A. Scala, T. Voigtmann and C. De Michele, *Event-driven Brownian dynamics for hard spheres*, J. Chem. Phys. **126**, 134109 (2007), doi:10.1063/1.2719190.

[62] N. Metropolis, A. W. Rosenbluth, M. N. Rosenbluth, A. H. Teller and E. Teller, *Equation of state calculations by fast computing machines*, J. Chem. Phys. **21**, 1087 (1953), doi:10.1063/1.1699114.

[63] W. K. Hastings, *Monte Carlo sampling methods using Markov chains and their applications*, Biometrika **57**, 97 (1970), doi:10.1093/biomet/57.1.97.

[64] F. Sammüller and M. Schmidt, *Adaptive Brownian dynamics*, J. Chem. Phys. **155**, 134107 (2021), doi:10.1063/5.0062396.

[65] D. de las Heras, J. Renner and M. Schmidt, *Custom flow in overdamped Brownian dynamics*, Phys. Rev. E **99**, 023306 (2019), doi:10.1103/physreve.99.023306.

[66] M. Schmidt, *Power functional theory for many-body dynamics*, Rev. Mod. Phys. (accepted) (2021), doi:10.48550/arXiv.2111.00432, https://arxiv.org/abs/2111.00432.

[67] J. Renner, M. Schmidt and D. de las Heras, *Custom flow in molecular dynamics*, Phys. Rev. Research **3**, 013281 (2021), doi:10.1103/PhysRevResearch.3.013281.

[68] E. Bernreuther and M. Schmidt, *Superadiabatic forces in the dynamics of the one-dimensional Gaussian core model*, Phys. Rev. E **94**, 022105 (2016), doi:10.1103/PhysRevE.94.022105.

[69] J. K. Percus, *Equilibrium state of a classical fluid of hard rods in an external field*, J. Stat. Phys. **15**, 505 (1976), doi:10.1007/BF01020803.

[70] A. Robledo and C. Varea, *On the relationship between the density functional formalism and the potential distribution theory for nonuniform fluids*, J. Stat. Phys. **26**, 513 (1981), doi:10.1007/BF01011432.

[71] D. de las Heras, J. M. Brader, A. Fortini and M. Schmidt, *Particle conservation in dynamical density functional theory*, J. Phys.: Condens. Matter **28**, 244024 (2016), doi:10.1088/0953-8984/28/24/244024.

[72] H. Hansen-Goos and R. Roth, *Density functional theory for hard-sphere mixtures: the White Bear version mark II*, J. Phys.: Condens. Matter **18**, 8413 (2006), doi:10.1088/0953-8984/18/37/002.

[73] P. Tarazona, *Density functional for hard sphere crystals: A fundamental measure approach*, Phys. Rev. Lett. **84**, 694 (2000), doi:10.1103/PhysRevLett.84.694.

[74] Davidchack, Laird and Roth, *Hard spheres at a planar hard wall: Simulations and density functional theory*, Condens. Matter Phys. **19**, 23001 (2016), doi:10.5488/CMP.19.23001.

[75] D. de las Heras and M. Schmidt, *Velocity gradient power functional for Brownian dynamics*, Phys. Rev. Lett. **120**, 028001 (2018), doi:10.1103/PhysRevLett.120.028001.

[76] N. C. X. Stuhlmüller, T. Eckert, D. de las Heras and M. Schmidt, *Structural nonequilibrium forces in driven colloidal systems*, Phys. Rev. Lett. **121**, 098002 (2018), doi:10.1103/PhysRevLett.121.098002.

[77] S. Hermann, P. Krinninger, D. de las Heras and M. Schmidt, *Phase coexistence of active Brownian particles*, Phys. Rev. E **100**, 052604 (2019), doi:10.1103/PhysRevE.100.052604.

[78] S. Hermann, D. de las Heras and M. Schmidt, *Non-negative interfacial tension in phase-separated active Brownian particles*, Phys. Rev. Lett. **123**, 268002 (2019), doi:10.1103/PhysRevLett.123.268002.

[79] D. de las Heras and M. Schmidt, *Flow and structure in nonequilibrium brownian many-body systems*, Phys. Rev. Lett. **125**, 018001 (2020), doi:10.1103/PhysRevLett.125.018001.

[80] S. Hermann and M. Schmidt, *Active interface polarization as a state function*, Phys. Rev. Research **2**, 022003 (2020), doi:10.1103/PhysRevResearch.2.022003.

[81] S. Hermann, D. de las Heras and M. Schmidt, *Phase separation of active Brownian particles in two dimensions: anything for a quiet life*, Mol. Phys. **119**, e1902585 (2021), doi:10.1080/00268976.2021.1902585.

[82] S. Hermann and M. Schmidt, *Noether's theorem in statistical mechanics*, Commun. Phys. **4**, 176 (2021), doi:10.1038/s42005-021-00669-2.

[83] P. Krinninger, M. Schmidt and J. M. Brader, *Nonequilibrium phase behavior from minimization of free power dissipation*, Phys. Rev. Lett. **117**, 208003 (2016), doi:10.1103/PhysRevLett.117.208003.

[84] P. Krinninger and M. Schmidt, *Power functional theory for active Brownian particles: General formulation and power sum rules*, J. Chem. Phys. **150**, 074112 (2019), doi:10.1063/1.5061764.

[85] J. Dzubiella, G. P. Hoffmann and H. Löwen, *Lane formation in colloidal mixtures driven by an external field*, Phys. Rev. E **65**, 021402 (2002), doi:10.1103/PhysRevE.65.021402.

[86] S. Hermann and M. Schmidt, *Why Noether's theorem applies to statistical mechanics*, J. Phys.: Condens. Matter (2022), doi:10.1088/1361-648x/ac5b47, Accepted.

[87] *The implementation in python can be found at https://github.com/mithodin/ddft-spherical*.

[88] M. Dijkstra and R. Evans, *A simulation study of the decay of the pair correlation function in simple fluids*, J. Chem. Phys. **112**, 1449 (2000), doi:10.1063/1.480598.

[89] C. M. Rohwer, M. Kardar and M. Krüger, *Transient Casimir forces from quenches in thermal and active matter*, Phys. Rev. Lett. **118**, 015702 (2017), doi:10.1103/PhysRevLett.118.015702.

[90] C. M. Rohwer, A. Solon, M. Kardar and M. Krüger, *Nonequilibrium forces following quenches in active and thermal matter*, Phys. Rev. E **97**, 032125 (2018), doi:10.1103/PhysRevE.97.032125.

[91] G. H. Vineyard, *Scattering of slow neutrons by a liquid*, Phys. Rev. **110**, 999 (1958), doi:10.1103/PhysRev.110.999.

[92] D. de las Heras and M. Schmidt, *Full canonical information from grand-potential density-functional theory*, Phys. Rev. Lett. **113**, 238304 (2014), doi:10.1103/PhysRevLett.113.238304.

[93] M. Schmidt, *Density-functional theory for fluids in porous media*, Phys. Rev. E **66**, 041108 (2002), doi:10.1103/PhysRevE.66.041108.

[94] L. Lafuente and J. A. Cuesta, *First-principles derivation of density-functional formalism for quenched-annealed systems*, Phys. Rev. E **74**, 041502 (2006), doi:10.1103/PhysRevE.74.041502.

[95] M. Krüger, F. Weysser and M. Fuchs, *Tagged-particle motion in glassy systems under shear: Comparison of mode coupling theory and brownian dynamics simulations*, Eur. Phys. J. E **34**, 88 (2011), doi:10.1140/epje/i2011-11088-5.

[96] F. Vogel and M. Fuchs, *Stress correlation function and linear response of Brownian particles*, Eur. Phys. J. E **43**, 70 (2020), doi:10.1140/epje/i2020-11993-4.

[97] *The integration scheme is implemented in the file https://github.com/mithodin/ddft-spherical/blob/master/ddft_shell.py*.

6. Eidesstattliche Versicherung

Hiermit versichere ich an Eides statt, dass ich die vorliegende Arbeit selbstständig verfasst und keine anderen als die von mir angegebenen Quellen und Hilfsmittel verwendet habe.

Weiterhin erkläre ich, dass ich die Hilfe von gewerblichen Promotionsberatern bzw. –vermittlern oder ähnlichen Dienstleistern weder bisher in Anspruch genommen habe, noch künftig in Anspruch nehmen werde.

Zusätzlich erkläre ich hiermit, dass ich keinerlei frühere Promotionsversuche unternommen habe.

Bayreuth, den 17. Juli 2022

Lucas Treffenstädt

Appendix

A. Functional optimisation with spherical symmetry

When solving the Euler-Lagrange equation in either PFT or DFT, analytical solutions do not usually exist. Numerical methods are therefore needed to obtain the desired solution, be it the density $\xi(\mathbf{r})$ or the current $\mathbf{J}(\mathbf{r}, t)$.

In the considered frameworks, the Euler-Lagrange equations are generated from a generating functional $\mathscr{F}$ (not to be confused with the free energy functional) by functional differentiation with respect to a test function $g(\mathbf{r})$:

$$\left.\frac{\delta \mathscr{F}[g]}{\delta g(\mathbf{r})}\right|_{g=g_0(\mathbf{r})} = 0, \tag{A.1}$$

where $\mathscr{F}$ is minimal for the solution $g_0(\mathbf{r})$. In the considered frameworks, this can be rewritten as

$$g_0(\mathbf{r}) = \phi[g_0], \tag{A.2}$$

where $\phi[\cdot]$ can be a function or functional, such that (A.2) is usually an implicit equation for g_0. This can be solved iteratively, e.g. by Picard iteration, but then convergence can be slow. A better approach is to take advantage of the fact that g_0 minimises $\mathscr{F}$. In a planar geometry, where g varies only along the x direction, g can be approximated by a piecewise step function

$$\gamma(x) = \sum_{k=0}^{N} \gamma_k b(x - x_k) \approx g(x), \tag{A.3}$$

where $x_k = k\Delta x$ with step width Δx, and $b(\cdot)$ is a box function

$$b(x) = \begin{cases} 1 & \text{for } 0 \leq x < \Delta x \\ 0 & \text{elsewhere.} \end{cases} \tag{A.4}$$

We can reinterpret the coefficients γ_k as the entries of a vector in an $(N+1)$-dimensional vector space. Then, if $\mathscr{F}$ is minimal at $\gamma(x)$,

$$\nabla_\gamma \mathscr{F}[\gamma] = \sum_{k=0}^{N} \frac{\partial}{\partial \gamma_k} \mathscr{F}[\gamma] \hat{\mathbf{e}}_k = 0, \tag{A.5}$$

where $\hat{\mathbf{e}}_k$ is the unit vector in direction k in our vector space. The problem can now be solved with any of a wide range of gradient-based optimisation methods, like conjugated gradients or the limited memory Broyden–Fletcher–Goldfarb–Shanno algorithm (LBFGS) [106, 107]. High quality implementations exist for many of these methods, which can be used without much trouble [108]. The speed of the minimisation is then mostly dependent on the efficient and fast evaluation of $\mathscr{F}[\gamma]$ and $\nabla\mathscr{F}[\gamma]$. If the evaluation of these functions is computationally intensive, it can be worthwhile to find a minimisation method which uses only a small number of evaluations, perhaps at the cost of increased memory overhead.

It should be noted that the numerical gradient in (A.5) is closely related to the functional derivative of $\mathscr{F}$ with respect to g. If, in the case of a planar geometry, the specific form of the functional is an integral according to

$$\mathscr{F}[g] = \int_V f(g(\mathbf{r}))\,\mathrm{d}^3 r = \int \mathrm{d}z \int \mathrm{d}y \int \mathrm{d}x\, f(g(x)) = A \int \mathrm{d}x\, f(g(x)), \tag{A.6}$$

with constant A, it holds that

$$\begin{aligned}
\nabla_\gamma \mathscr{F}[\gamma] &= \sum_{k=0}^{N} \frac{\partial}{\partial \gamma_k} A \int f(\gamma(x))\,\mathrm{d}x \hat{\mathbf{e}}_k \\
&= A \sum_{k=0}^{N} \int \frac{\partial f}{\partial \gamma} b(x - x_k)\mathrm{d}x \hat{\mathbf{e}}_k = A \sum_{k=0}^{N} \left.\frac{\partial f}{\partial \gamma}\right|_{x=x_k} \int b(x - x_k)\mathrm{d}x \hat{\mathbf{e}}_k \\
&= A \sum_{k=0}^{N} \left.\frac{\partial f}{\partial \gamma}\right|_{x=x_k} \Delta x \hat{\mathbf{e}}_k = A \Delta x \sum_{k=0}^{N} \left.\frac{\delta \mathscr{F}[g]}{\delta g(\mathbf{r})}\right|_{g=\gamma_k} \hat{\mathbf{e}}_k.
\end{aligned} \tag{A.7}$$

We can therefore calculate the functional derivative analytically, and only then substitute g with γ, to obtain the numerical gradient, keeping in mind the factor of $A\Delta x$ in the final expression (A.7). The calculation works along similar lines if $\mathscr{F}$ is more complicated than (A.6).

In the case of radial symmetry, the equivalence between the numerical gradient and the functional derivative is not quite so straightforward. We start again with an

approximation for g, which we now assume to be radially symmetric, $g(\mathbf{r}) = g(|\mathbf{r}|) = g(r)$, where r is the modulus of $\mathbf{r}$. We can then choose the approximation

$$g(r) \approx \xi(r) = \sum_{k=0}^{N} \xi_k b(r - r_k), \tag{A.8}$$

where $r_k = k\Delta r$, and the coefficients ξ_k can again be interpreted as entries of a vector in a vector space with basis $\{\hat{\mathbf{e}}_k\}$.

Then, if our system is a spherical cavity with radius R, like in the case of our calculations for the van Hove function,

$$\begin{aligned}
\mathscr{F}[\xi] &= \int_V f(\xi(r)) \mathrm{d}^3 r = \int_0^{2\pi} \mathrm{d}\varphi \int_0^{\pi} \mathrm{d}\theta \int_0^{R} \mathrm{d}r\, r^2 \sin\theta f(\xi(r)) \\
&= 4\pi \int_0^{R} r^2 f(\xi(r)) = 4\pi \sum_{k=0}^{N} \int_0^{R} \mathrm{d}r\, r^2 f(\xi_k b(r - r_k)) \\
&= 4\pi \sum_{k=0}^{N} \int_{r_k}^{r_{k+1}} \mathrm{d}r\, r^2 f(\xi_k) = \frac{4}{3}\pi\Delta r^3 \sum_{k=0}^{N} f(\xi_k)\left((k+1)^3 - k^3\right),
\end{aligned} \tag{A.9}$$

and therefore

$$\begin{aligned}
\nabla_\xi \mathscr{F}[\xi] &= \frac{4}{3}\pi\Delta r^3 \sum_{k=0}^{N} \left.\frac{\partial f}{\partial \xi}\right|_{r=r_k} \left((k+1)^3 - k^3\right)\hat{\mathbf{e}}_k \\
&= \frac{4}{3}\pi\Delta r^3 \sum_{k=0}^{N} \left.\frac{\delta \mathscr{F}[g]}{\delta g(\mathbf{r})}\right|_{g=\xi_k} \left((k+1)^3 - k^3\right)\hat{\mathbf{e}}_k.
\end{aligned} \tag{A.10}$$

We can therefore also calculate the numerical gradient via an analytic functional derivative of $\mathscr{F}$. However, the scaling factor is no longer independent of k, which presents an issue with standard minimisation techniques. The root cause is that the discrete points ξ_k no longer contribute equally to the numerical value of the total integral, but are weighted by a spherical shell, which grows with the radius. Therefore, convergence is much slower for inner points (at small r) than for outer points.

There are two ways to address this. The first one is preconditioning, where we modify the numerical approximation $\xi(r)$:

$$\tilde{\xi}(r) = \sum_{k=0}^{N} \frac{\xi_k}{(k+1)^3 - k^3} b(r - r_k), \tag{A.11}$$

such that all ξ_k have equal weight in the integral. However, we found that this option can result in much increased numerical noise in the solution due to division by small numbers (see the denominator in (A.11)).

The second option is going back to (A.2) and solving it with Picard iteration. This option is – as discussed above – slow, but in our experience more reliable than preconditioned numerical minimisation. An option that is potentially better yet could be to find a (noisy) first approximation by numerical minimisation, followed by a few Picard iteration steps to eliminate the noise. We have not tested this last idea.

B. Rosenfeld functional in quasi-1d-geometries

As outlined in section 1.7, we write the excess free energy functional as a functional of weighted densities n_α:

$$F_{\text{exc}}[\rho] = \int \mathrm{d}^3 r \Phi(\{n_\alpha\}), \tag{B.1}$$

which are in turn calculated as a convolution of the local density profile with weight functions ω_α (see eq. (1.22)). This means the functional derivative of F_{exc} with respect to the density can be expanded as follows

$$\frac{\delta F_{\text{exc}}[\rho]}{\delta \rho(\mathbf{r})} = \int \mathrm{d}^3 r' \sum_\alpha \frac{\partial \Phi(\{n_\alpha\})}{\partial n_\alpha(\mathbf{r}')} \frac{\delta n_\alpha[\rho]}{\delta \rho(\mathbf{r})} = \sum_\alpha \Psi_\alpha(\mathbf{r}). \tag{B.2}$$

Here we want to show briefly how we evaluate this functional derivative in the case of a planar geometry and a radially symmetric geometry. These results are outlined by Roth in his review of FMT [19] and can be found in detail in Daniel Stopper's Bachelor thesis [109].

B.1. Planar geometry

First, we consider the case of a planar geometry, where the density varies only in x and is constant in the perpendicular plane:

$$\rho(\mathbf{r}) = \rho(x). \tag{B.3}$$

We then get the weight functions

$$\omega_3(x) = \pi(R^2 - x^2)\Theta(R - |x|), \tag{B.4}$$
$$\omega_2(x) = 2\pi R \Theta(R - |x|), \tag{B.5}$$
$$\boldsymbol{\omega}_2(x) = 2\pi x \Theta(R - |x|)\hat{\mathbf{e}}_x, \tag{B.6}$$

and the functional derivatives

$$\frac{\delta n_3(x')}{\delta \rho(x)} = \omega_3(x'-x), \tag{B.7}$$

$$\frac{\delta n_2(x')}{\delta \rho(x)} = \omega_2(x'-x), \tag{B.8}$$

$$\frac{\delta \mathbf{n}_2(x')}{\delta \rho(x)} = \boldsymbol{\omega}_2(x'-x) = -\boldsymbol{\omega}_2(x-x'), \tag{B.9}$$

as shown in [19]. For the vector weighted densities, it is important to ensure the correct order of the arguments, as changing them changes the sign of the weight function. The other weight functions are even in x and thus are not sensitive to that distinction [19].

B.2. Radial geometry

Next, we consider systems where the density is radially symmetric:

$$\rho(\mathbf{r}) = \rho(r), \tag{B.10}$$

where $r = |\mathbf{r}|$ is the modulus of $\mathbf{r}$. The resulting effective weights after integrating out the rotational degrees of freedom are [19, 109]:

$$n_3(r) = \begin{cases} 4\pi \int_0^R \mathrm{d}r' r'^2 \rho(r') & \text{for } r = 0 \\ 4\pi \int_0^{R-r} \mathrm{d}r' r'^2 \rho(r') + \frac{\pi}{r} \int_{R-r}^{R+r} \mathrm{d}r' r' \rho(r') \left(R^2 - (r-r')^2\right) & \text{for } 0 < r < R \\ \frac{\pi}{r} \int_{r-R}^{R+r} \mathrm{d}r' r' \rho(r') \left(R^2 - (r-r')^2\right) & \text{for } r \geq R \end{cases} \tag{B.11}$$

$$n_2(r) = \begin{cases} 4\pi R^2 \rho(R) & \text{for } r = 0 \\ \frac{2\pi R}{r} \int_{|r-R|}^{r+R} \mathrm{d}r' r' \rho(r') & \text{for } r > 0 \end{cases} \tag{B.12}$$

$$\mathbf{n}_2(r) = \begin{cases} 0 & \text{for } r = 0 \\ \frac{\pi}{r} \hat{\mathbf{e}}_r \int_{|r-R|}^{r+R} \mathrm{d}r' r' \rho(r') \left[2(r-r') + \frac{R^2 - (r-r')^2}{r} \right] & \text{for } r > 0, \end{cases} \tag{B.13}$$

where $\hat{\mathbf{e}}_r = \mathbf{r}/r$ is the unit vector in radial direction. Calculations for the functional derivative are, again, similar to those of the weighted densities. We get for

$$\Psi_\alpha(r) = \int_0^\infty \mathrm{d}r' \frac{\partial \Phi(r')}{\partial n_\alpha(r')} \frac{\delta n_\alpha(r')}{\delta \rho(r)} \tag{B.14}$$

the following integrals [19, 109]:

$$\begin{aligned} 4\pi R^2 \Psi_0(r) &\mathrel{\widehat{=}} 4\pi R \Psi_1(r) \\ &\mathrel{\widehat{=}} \Psi_2(r) = \begin{cases} 4\pi R^2 \dfrac{\partial \Phi(R)}{\partial n_{0|1|2}} & \text{for } r = 0 \\ \dfrac{2\pi R}{r} \displaystyle\int_{|r-R|}^{r+R} \mathrm{d}r' r' \frac{\partial \Phi(r')}{\partial n_{0|1|2}} & \text{for } r > 0 \end{cases} \end{aligned} \tag{B.15}$$

$$\Psi_3(r) = \begin{cases} 4\pi \displaystyle\int_0^R \mathrm{d}r' r'^2 \frac{\partial \Phi(r')}{\partial n_3} & \text{for } r = 0 \\ 4\pi \displaystyle\int_0^{R-r} \mathrm{d}r' r'^2 \frac{\partial \Phi(r')}{\partial n_3} + \frac{\pi}{r} \int_{R-r}^{R+r} \mathrm{d}r' r' \frac{\partial \Phi(r')}{\partial n_3} \left(R^2 - (r-r')^2\right) & \text{for } 0 < r < R \\ \dfrac{\pi}{r} \displaystyle\int_{r-R}^{r+R} \mathrm{d}r' r' \frac{\partial \Phi(r')}{\partial n_3} \left(R^2 - (r-r')^2\right) & \text{for } r \geq R \end{cases} \tag{B.16}$$

$$\begin{aligned} 4\pi R \boldsymbol{\Psi}_1(r) &\mathrel{\widehat{=}} \\ &\boldsymbol{\Psi}_2(r) = \begin{cases} 4\pi R^2 \dfrac{\partial \Phi(R)}{\partial \mathbf{n}_{1|2}} & \text{for } r = 0 \\ \dfrac{\pi}{r} \displaystyle\int_{|r-R|}^{r+R} \mathrm{d}r' \frac{\partial \Phi(r')}{\partial \mathbf{n}_{1|2}} \left[\left(R^2 - (r-r')^2\right) - 2r'(r-r')\right] & \text{for } r > 0, \end{cases} \end{aligned} \tag{B.17}$$

where the equivalence sign $\mathrel{\widehat{=}}$ is used to indicate that the integral takes the same form, but has a different integrand $\dfrac{\partial \Phi(r)}{\partial n_\alpha(r)}$. These integrals, as well as the ones for

the weighted densities, require careful numerical evaluation. We sketch our approach below in appendix E.

C. GPGPU computation with Nvidia CUDA

Graphics processing units (GPUs) are computational devices originally designed to accelerate the rendering of 3D graphics, often for the purpose of computer games. The strength of GPUs lies in the availability of many parallel processing units, way beyond the number of processors available even in high-end central processing units (CPUs). This, coupled with high memory bandwidths for internal storage, has made GPUs interesting for applications beyond their original purpose [110]. Current applications include artificial intelligence, processing of very large datasets, and, increasingly, computational physics. The usage of GPUs for computation other than 3D graphics is termed general purpose computation on graphics processing units, or GPGPU in short.

One possible avenue for the usage of GPGPU is the Nvidia CUDA programming library [111], which allows the execution of code written in C, or other compatible languages, on Nvidia GPUs. This has the advantage of being provided directly by the manufacturer Nvidia with the promise of maximal performance. However, it is tied to Nvidia hardware and cannot be used on other highly parallel computation devices.

C.1. General overview and concepts

The CUDA framework provides a compiler, nvcc, to compile C into code which is executable on a GPU. The standard C syntax is extended with a few keywords and a special function call syntax for executing code on the GPU. Functions are discriminated into *host* functions, which execute on the CPU, *device* functions, which execute on the GPU, and *kernels*, which execute on the GPU and are called from host code, as show in a short example (Listing 1).

In this example, a 512-element array of doubles is initialised with numbers ranging from 0 to 16, and the function $f(x) = \sin(x)\cos(x)$ is applied to each element. Since

```
#include <cuda.h>

//A host function, executed on the CPU
__host__ int main(void){
    double *data;
    cudaMallocManaged(&data, 512 * sizeof(double));
    for(int i = 0; i < 512; ++i){
        data[i] = i / 32.0;
    }
    do_something<<<2,265>>>(data);
    cudaDeviceSynchronize();
    for(int i = 0; i < 512; ++i){
        printf("%f\n", data[i]);
    }
    return 0;
}

//A kernel, executed on the GPU
__global__ void do_something(double data[]){
    int i = blockDim.x * blockIdx.x + threadIdx.x;
    data[i] = process(data[i]);
}

//A device function, executed on the GPU
__device__ double process(double datum){
    return sin(datum) * cos(datum);
}
```

Listing 1: A short demonstration of the three types of functions in a CUDA program.

the computation is done on the GPU, which has its own memory, memory must be allocated both in system memory (or host memory), where the CPU can access it, and in GPU memory (or device memory). This example shows one option of achieving this, using the `cudaMallocManaged` call, which allocates memory in both locations at once. Data is then automatically transferred between the physical memory locations by the CUDA runtime environment. Instead, pure device memory can also be allocated using the `cudaMalloc` call and data can be transferred explicitly between host memory and device memory using the `cudaMemcpy` call. It should be noted that memory allocation on the GPU takes a very long time compared to the execution speed of the GPU. Thus, memory allocation in inner loops should be avoided where possible. If feasible, it is preferable

to allocate memory once at the beginning of a program, possibly reusing memory in different parts of the application if the overall memory requirement becomes too high.

Line 10 in the example shows the syntax for a call to a kernel from host code. This call is different from a normal function call in a number of ways. Most obvious is the fact that the kernel call is *configured* with two numbers in triple angle brackets `<<<2,265>>>`, which defines the number of parallel executions of the kernel code. The first number defines the number of *blocks* of threads, and the second number defines the number of threads in each block, where each thread executes the same code in parallel. Thus, in our example, we are running 512 threads, divided into two blocks of 256 threads each. In general, the number of blocks as well as the number of threads can be a tuple of up to three numbers, which defines a grid of blocks/threads with the given number of blocks/threads in each dimension. The total number of blocks and threads per block is constrained by the GPU hardware. As an example, the GPU available to us that the time of this thesis is an Nvidia Quadro K2200, which allows for a maximum of 1024 threads in a block. Each thread has access to a data structure which defines its position in the grid of threads as well as the position of its parent block in the grid of blocks, which allows one to define the distribution of work between threads (Listing 1, line 20).

The second major difference between a normal function call and a kernel call is that the kernel call is asynchronous, meaning that execution of the host code continues immediately after the kernel call has been started on the GPU. If multiple kernels are started in sequence, CUDA guarantees that the kernels executed in the order they were launched in, one starting immediately after the previous one has finished execution. Parallel execution of multiple kernels is also possible, using CUDA streams, which we shall not go into here. To wait for the execution of a kernel to finish, we can call the function `cudaDeviceSynchronize`, which blocks execution of the host code until all previous kernel calls have terminated. Only then can the result of the computation be copied back to host memory, either implicitly like in our example, or explicitly using `cudaMemcpy`.

Lastly, all kernel functions must have the `void` return type. Data can only be transferred from the GPU to the host via memory copies.

C.2. Brownian dynamics simulation using CUDA: a sketch

We give a sketch of our implementation of Brownian dynamics simulation (BD), which makes use of the CUDA framework. An introduction to the principles of BD simulation is given in section 1.2. In short, the core loop of the simulation consists of

- calculating velocities for all particles,
- detecting collisions and handling them according to the event-driven Brownian dynamics algorithm,
- propagating all particle positions in time until the next time step has been reached.

In each of the following subsections, we take examples from these steps to demonstrate the challenges, solutions and advantages of GPU programming.

C.2.1. Parallel vector addition

In listing 2, we see an example of the parallel addition of many vectors. The kernel `move` calculates the new positions `p_next` of `NUM_PARTICLES` particles in `DIM` dimensions, starting from the current positions `p_now`. We make use of a `rows` × `cols` block of threads, where the number of rows corresponds to the number of particles, and the number of columns (cols) corresponds to the number of dimensions. Since we might have more particles than the number of threads (defined in the macro `THREADS`) allows in this setup, we need to create multiple blocks, each of which handles up to `THREADS / DIM` particles.

Additionally, we provide each block with a chunk of shared memory, given as the third kernel configuration parameter on line 11 of listing 2, and declared inside the kernel at line 15. Nvidia GPUs provide different sections of memory with different access properties and read/write speeds. Shared memory is block-local, meaning only threads within the same block can read each other's shared memory. However, shared memory is faster than global memory, which is accessible by all threads on the device. Since we only need to store the force intermediately, we can leverage the speed of shared memory in this case.

```
1  typedef struct vector {
2          double r[DIM];
3  } Vector;
4
5  // in some other function
6      int rows = THREADS / DIM;
7      int cols = DIM;
8      int blocks = (NUM_PARTICLES + rows - 1) / rows;
9      dim3 threads(rows, cols, 1);
10
11     move<<<blocks, threads, rows * sizeof(Vector)>>>(p_now, rand, p_next);
12 // ...
13
14 __global__ void move(Vector p_now[], Vector rand[], Vector p_next[]){
15     extern __shared__ Vector force_i[];
16     int i = blockDim.x * blockIdx.x + threadIdx.x;
17     int component = threadIdx.y;
18     if( i >= NUM_PARTICLES || component >= DIM ){
19         return;
20     }
21     if( component == 0 ){
22         force(&p_now[i], &force_i[threadIdx.x], i);
23     }
24     __syncthreads();
25     p_next[i].r[component] = p_now[i].r[component]
26                              + force_i[threadIdx.x].r[component]
27                              + rand[i].r[component];
28 }
```

Listing 2: A section of our BD simulation code. A number `NUM_PARTICLES` of particles in `DIM` dimensions is displaced with a random displacement and a systematic displacement due to an external force.

Inside the `move` kernel, we first identify which particle (index `i`) and which component of the position vector (index `component`) each thread handles. The layout is chosen such that each block of threads handles a consecutive slice of the input array `p_now[]` of length `blockDim.x`, which corresponds to the number of threads in the first dimension of the thread grid. Thus, threads sharing the same `threadIdx.x` within a block act on the same vector. The index `threadIdx.y` defines which component of the vector is handled. Since the number of particles might not be evenly divisible by `blockDim.x`, threads with indices `i` above and including `NUM_PARTICLES` need to exit early (see lines 18 – 19) to avoid out of

bounds reads/writes on the input and output arrays.

On lines 21 – 23 (listing 2), the force on each particle is calculated using a call to an external device function. Notice that we calculate the force vector acting on each particle once instead of making one calculation for each vector component of the force on each particle. We assign that work only to the threads with component 0 using the `if` condition in line 21. Since the subsequent addition of vectors is again distributed across all threads, a synchronisation barrier is needed to ensure that the force vector has been calculated before the addition takes place. This is because threads, even within the same block, are not guaranteed to execute synchronously. In the CUDA execution model, threads are grouped into warps, which are groups of a smaller number of threads (32 in the case of our hardware). Only threads within the same warp are guaranteed to execute synchronously, meaning they execute the same instruction at the same time. Threads within one block can be explicitly synchronised via a call to `__syncthreads`, which blocks further execution until all threads within the block have reached this barrier. There is no way of synchronising execution between blocks, except to split the code in question into two subsequent kernel calls.

After the synchronisation barrier is passed, the vector addition takes place. The array `rand[]` is assumed to contain random vectors with a Gaussian distribution in each component. The CUDA framework provides the cuRAND library [112] to generate random numbers efficiently. Numbers following a Gaussian distribution can be generated using the function call `curandGenerateNormalDouble(generator, array, num, mean, std)`, which generates `num` doubles with mean `mean` and standard deviation `std` and places them into `array`, which must be allocated in device memory.

C.2.2. Parallel collision detection

A central step of BD simulation of hard spheres is collision detection, which is executed many times during each time step. With GPGPU, we can detect collisions in parallel, which promises a major speedup. Our implementation is shown in listing 3. As in our previous example, we distribute this work between multiple blocks of threads, as the total number of potential pair collisions ($n(n-1)/2$ for n particles) is likely larger than the maximum number of threads. We pass into the kernel `detect_collisions` an array of vectors `p_now[]`, which gives the positions of all particles at time t_0, and

an array `p_next[]`, which gives the positions at time t_1. Additionally, we pass an array of `Collision` pointers, where each block of threads may store a linked list of detected collisions. A linked list is a data structure which represents a list of items, where each item contains a pointer to the next item in the list (see type definition on lines 3 – 8, listing 3). With this technique, we can have lists of arbitrary dynamic length at the cost of some computational time needed to traverse the list, whereas with an array, we have instant access to any element. To pass a linked list to some other function, we need only a pointer to the first element in the list.

In the first section of the kernel, we distribute particle pairs over the threads. From the linear index of threads `index`, we calculate a particle pair `i,j` (line 20). The collision check is done in the function `pair_collision`, which calculates the collision time (if a collision would occur between t_0 and t_1) and returns a `Collision` pointer. The `Collision` struct contains the particle indices `i` and `j`, as well as the time of collision and a pointer to the next collision, which is, for now, unknown and thus `NULL`. If no collision is detected, `pair_collision` returns a null pointer.

Out of the results of all threads, we now need to build a list, which shall be sorted by the collision time. A straightforward way to achieve this would be to return the collisions in an array and then iterate over that array to build the list. However, that would not make good use of the many available threads. Instead, we make use of the parallel reduction technique. The implementation is closely based on a tutorial provided by Nvidia [113].

First, a synchronisation barrier is used to make sure all threads have finished collision detection. Then, we select the lower `s` threads, where `s` is the number of threads, rounded down to the next lowest power of two. Each of the selected threads (with index `threadIdx.x`) merges its own list of collisions (which is, for now, either one or no collisions) with the list of collisions of thread `threadIdx.x + s`. The function `merge` merges two linked lists of collisions. The resulting list is sorted by collision time, given that both input lists are sorted, which is trivially the case for lists of one or zero elements. The resulting list is stored in the first argument to `merge`. We again block further execution, until all threads have finished the merge operation.

The number `s` is then halved and the process is repeated until `s` is equal to 32. We then continue the process, but no longer need to include the synchronisation barrier, as 32 threads constitute a warp, which is guaranteed to execute synchronously (see [113]).

Therefore, the overhead of the synchronisation be be avoided. Finally, only the thread with index 0 remains, which stores its list of collisions in the `collisions` array at index `blockIdx.x`. Thus, after the kernel has finished, we have an array of lists of collisions, which can then be merged one final time to obtain a list of all collisions.

The parallel reduction technique can be used whenever the reduction operation is associative. Thus, we also apply this technique for e.g. sums of arrays of numbers. Here, the merging of two lists is associative, since the ordering of elements is determined by the collision time, such that it does not matter in which order which lists are merged together.

```
#define INTERACTIONS ( ( NUM_PARTICLES * ( NUM_PARTICLES - 1 ) ) / 2 )

typedef struct collision {
    double time;
    int i;
    int j;
    struct collision *next;
} Collision;

__global__ void detect_collisions( Vector p_now[],
                                   Vector p_next[],
                                   Collision *collisions[] ){
    extern __shared__ Collision *my_collision[];
    int index = blockDim.x * blockIdx.x + threadIdx.x;
    my_collision[threadIdx.x] = NULL;
    if( index >= INTERACTIONS ){
        return;
    }
    int i,j;
    pair_from_index(index, &i, &j);
    my_collision[threadIdx.x] = pair_collision( p_now, p_next, i, j );
    __syncthreads();

    int s = floor_pow2(blockDim.x); //next lowest power of two
    for(;s > 32;s /= 2){
        if( threadIdx.x < s && threadIdx.x + s < blockDim.x ){
            merge(&my_collision[threadIdx.x], &my_collision[threadIdx.x + s]);
        }
        __syncthreads();
    }

    //now we no longer need to synchronise because we are in the same warp
    for(;s > 0;s /= 2){
        if( threadIdx.x < s ){
            merge(&my_collision[threadIdx.x],&my_collision[threadIdx.x+s]);
        }
    }

    if( threadIdx.x == 0 ){
        collisions[blockIdx.x] = my_collision[0];
    }
}
```

Listing 3: A section of our BD simulation code. Pair collisions between particles are detected in parallel. A sorted list of collisions is built using a parallel reduction scheme.

D. Radial and planar diffusion kernel

In section 2.1.1, we defined the diffusive memory kernel (2.9), which we split here into its temporal part and its spatial part as

$$K_{\mathrm{D}}(\mathbf{r},\Delta t) = K(\mathbf{r},\Delta t)\exp(-\Delta t/\tau_{\mathrm{M}})/\tau_{\mathrm{M}}, \tag{D.1}$$

such that the spatial part is

$$K(\mathbf{r}-\mathbf{r}',\Delta t) = (4\pi D_{\mathrm{M}}\Delta t)^{-3/2}\exp\left[-\frac{(\mathbf{r}-\mathbf{r}')^2}{4D_{\mathrm{M}}\Delta t}\right], \tag{D.2}$$

with radii r and r', time difference Δt, and memory diffusion constant D_{M}. The temporal part is not relevant for the discussion in this chapter. We apply this kernel in two different geometries with respective symmetries.

D.1. Planar geometry

In the planar geometry, we investigate the case of translational symmetry in two dimensions, with only one remaining spatial dimension. In this case, two degrees of freedom of $\mathbf{r}-\mathbf{r}'$ can be straightforwardly integrated out. Thus, we get the planar memory kernel

$$K_{\mathrm{P}}(x-x',\Delta t) = (4\pi D_{\mathrm{M}}\Delta t)^{-1/2}\exp\left[-\frac{(x-x')^2}{4D_{\mathrm{M}}\Delta t}\right]. \tag{D.3}$$

The integral is downright trivial, but hopefully helps to understand what we are doing here.

D.2. Radial geometry

In this case, we assume radial symmetry. We want to use $K(\mathbf{r},t)$ in integrals of the form

$$I(t)=\int_V \mathrm{d}^3 r \int_V \mathrm{d}^3 r' \int \mathrm{d}t' f(r,t) K(\mathbf{r}-\mathbf{r}',\Delta t) g(r',t'), \tag{D.4}$$

with moduli $r=|\mathbf{r}|$ and $r'=|\mathbf{r}'|$, which applies e.g. in the case of the viscoelastic contribution (2.2) to the superadiabatic functional. Since f and g depend only on the moduli, part of the integral can be evaluated without knowledge of the exact form of those functions. With a change from Cartesian to spherical coordinates, we obtain

$$I(t)= \int \mathrm{d}t' \int \mathrm{d}r \int \mathrm{d}r' \int \mathrm{d}\theta \int \mathrm{d}\varphi \int \mathrm{d}\theta' \int \mathrm{d}\varphi' r^2 \sin\theta r'^2 \sin\theta' f g K(\mathbf{r}(r,\theta,\varphi)-\mathbf{r}'(r',\theta',\varphi'),\Delta t). \tag{D.5}$$

The part that we want to evaluate is

$$I_{\mathrm{ang}}=(4\pi D_{\mathrm{M}}\Delta t)^{-3/2} \int \mathrm{d}\theta \int \mathrm{d}\varphi \int \mathrm{d}\theta' \int \mathrm{d}\varphi' \sin\theta \sin\theta' \exp\left[-\frac{(\mathbf{r}-\mathbf{r}')^2}{4D_{\mathrm{M}}\Delta t}\right]. \tag{D.6}$$

While evaluation of this integral by just using the definition of $\mathbf{r}(r,\theta,\varphi)$ is certainly possible, it is by no means straightforward. However, for every θ,φ of the outer double integral, we can choose the coordinate system for the inner double integral such that

$$(\mathbf{r}-\mathbf{r}')^2=\mathbf{r}^2+\mathbf{r}'^2-2\mathbf{r}\cdot\mathbf{r}'=r^2+r'^2-2rr'\cos\theta', \tag{D.7}$$

without changing the value of the integral. This gives us without much difficulty

$$I_{\mathrm{ang}}=8\pi^2(4\pi D_{\mathrm{M}}\Delta t)^{-3/2} \exp\left[-\frac{r^2+r'^2}{4D_{\mathrm{M}}\Delta t}\right] \int \mathrm{d}\theta' \sin\theta' \exp\left[\frac{2rr'\cos\theta'}{4D_{\mathrm{M}}\Delta t}\right], \tag{D.8}$$

since the integrand no longer depends on θ, φ or φ'. The remaining integral in (D.8) is easily evaluated by substituting $y=\cos\theta'$ and using the identity

$$\int_0^{\pi} \mathrm{d}\theta' \sin\theta' \exp(a\cos\theta') = \int_{-1}^{1} \mathrm{d}y \exp(ay) = \frac{1}{a}[\exp(a)-\exp(-a)]. \tag{D.9}$$

This gives us, by substitution back into (D.5), the integral

$$I(t) = 4\pi \int \mathrm{d}t' \int \mathrm{d}r \int \mathrm{d}r' r^2 r'^2 f\, g\, (4\pi D_\mathrm{M} \Delta t)^{-1/2} \cdot \left(r\, r'\right)^{-1} \left[\exp\left(-\frac{(r-r')^2}{4 D_\mathrm{M} \Delta t} \right) - \exp\left(-\frac{(r+r')^2}{4 D_\mathrm{M} \Delta t} \right) \right], \quad \text{(D.10)}$$

and thus the radial memory kernel

$$K_\mathrm{R}(r, r', \Delta t) = (4\pi D_\mathrm{M} \Delta t)^{-1/2} \left(r\, r'\right)^{-1} \left[\exp\left(-\frac{(r-r')^2}{4 D_\mathrm{M} \Delta t} \right) - \exp\left(-\frac{(r+r')^2}{4 D_\mathrm{M} \Delta t} \right) \right]. \quad \text{(D.11)}$$

Note that, in a numerical implementation, the limits $r \to 0$ and $r' \to 0$ must be calculated analytically to avoid division by zero. We obtain

$$K_\mathrm{R}(r, 0, \Delta t) = K_\mathrm{R}(0, r, \Delta t) = \\ = \lim_{r' \to 0} K_\mathrm{R}(r, r', \Delta t) = (4\pi D_\mathrm{M} \Delta t)^{-3/2} \exp\left(-\frac{r^2}{4 D_\mathrm{M} \Delta t} \right), \quad \text{(D.12)}$$

and thus

$$K_\mathrm{R}(0, 0, \Delta t) = (4\pi D_\mathrm{M} \Delta t)^{-3/2}, \quad \text{(D.13)}$$

except, of course, when $\Delta t = 0$, where the diffusive memory kernel is a delta distribution.

E. Integration of radially symmetric functions

E.1. Numerical radial integration

The numerical implementation of the DFT functionals in section B.2 requires the calculation of multiple integrals of the form

$$\int_{R_0}^{R_1} \mathrm{d}r\, r^n f(r) \tag{E.1}$$

with integer exponent $n = 1,2,3$, where R_0 and R_1 are, respectively, the inner and outer radius of a spherical shell. For planar integrals of the form

$$\int_{X_0}^{X_1} \mathrm{d}x\, g(x) \tag{E.2}$$

numerical integration is usually done using the trapezoidal rule, whereby a discrete approximation of $g(x)$, consisting of $N+1$ values $g_i = g(x_i)$ with $x_i = X_0 + i\Delta x$, $\Delta x = (X_1 - X_0)/N$ and positive Integer N, can be used to evaluate the integral as

$$\int_{X_0}^{X_1} \mathrm{d}x\, g(x) \approx \sum_{i=0}^{N} w_i g_i \Delta x \tag{E.3}$$

with weights

$$w_i = \begin{cases} 1/2 & i = 0 \vee i = N \\ 1 & \text{else.} \end{cases} \tag{E.4}$$

Evaluation of (E.1) using (E.3) with $g(x) = x^n f(x)$ is possible, but has defects such as the fact that the discrete value $f_0 = f(0)$ never contributes to the integral.

To find a better approximation, we should remind ourselves that the trapezoidal rule is equivalent to the integral of a linear interpolation of our discrete values g_i:

$$g(x) \approx g_i(1-(x-x_i)/\Delta x) + g_{i+1}(x-x_i)/\Delta x \text{ for } x \in [x_i, x_{i+1}]. \tag{E.5}$$

Therefore, we will use a linear interpolation of $f(r)$ to obtain weights for the numerical evaluation of (E.1). To obtain the weights $w_k^{(n)}$ for the integral

$$\int_{R_0}^{R_1} \mathrm{d}r\, r^n f(r) \approx \sum_{k=0}^{N} w_k^{(n)} f_k \Delta r = \sum_{j=0}^{N-1} F_j, \tag{E.6}$$

where the distance from R_0 to R_1 is again split into equal steps Δr (see definition of Δx above), we calculate analytically the integral

$$F_j = \int_{r_j}^{r_{j+1}} r^n \left[f_j(1-(r-r_j)/\Delta r) + f_{j+1}(r-r_j)/\Delta r \right] \mathrm{d}r. \tag{E.7}$$

Note here that the second sum in (E.6) goes only to $N-1$, since $N+1$ points r_k divide the interval $[r_0, r_N]$ into N subintervals and summation starts at $j=0$. Note also that the integral F_j depends both on f_j and f_{j+1}, which means conversely that, to calculate the weight $w_k^{(n)}$, we need to take both F_{k-1} and F_k into account. Comparing coefficients of f_k, we find that

$$\Delta r\, w_k^{(n)} = \frac{\partial}{\partial f_k}(F_{k-1}+F_k) = \int_{r_{k-1}}^{r_k} r^n (r-r_{k-1})/\Delta r \mathrm{d}r + \int_{r_k}^{r_{k+1}} r^n [1-(r-r_k)/\Delta r] \mathrm{d}r, \tag{E.8}$$

for $0 < k < N$. For $k=0$, only F_0 contributes, whereas for $k=N$, only F_{N-1} contributes. This results in the weights as listed in table E.1.

E.2. Convolution of two radially symmetric functions

A particlular challenge is the (numerical) convolution of two radially symmetric functions. The convolution of two functions $f(\mathbf{r})$ and $g(\mathbf{r})$ is defined as

$$(f * g)(\mathbf{r}) = \int_V \mathrm{d}^3 r' f(\mathbf{r}-\mathbf{r}') g(\mathbf{r}'). \tag{E.9}$$

Table E.1.: Weights for radial numerical integrals $\int_{R_0}^{R_1} \mathrm{d}r\, r^n f(r)$.

n	$w_0^{(n)}$	$w_k^{(n)}$	$w_N^{(n)}$
0	$\frac{1}{2}$	1	$\frac{1}{2}$
1	$\frac{1}{6}(\Delta r + 3R_0)$	$k\Delta r + R_0$	$\frac{1}{6}(\Delta r(3N-1)+3R_0)$
2	$\frac{1}{12}\left(\Delta r^2 + 4\Delta r R_0 + 6R_0^2\right)$	$\frac{1}{6}\left(\Delta r^2(6k^2+1)+12\Delta r R_0 k + 6R_0^2\right)$	$\frac{1}{12}\left(\Delta r^2(6N^2-4N+1)\right.$ $\left.+\Delta r R_0(12N-4)+6R_0^2\right)$
3	$\frac{1}{20}\left(\Delta r^3 + 5\Delta r^2 R_0\right.$ $\left.+10\Delta r R_0^2 + 10R_0^3\right)$	$\frac{1}{2}\left(\Delta r^3(2k^3+k)+\Delta r^2 R_0(6k^2+1)\right.$ $\left.+6\Delta r R_0^2 k + 2R_0^3\right)$	$\frac{1}{20}\left(\Delta r^3(10N^3-10N^2+5N-1)\right.$ $+\Delta r^2 R_0(30N^2-20N+5)$ $\left.+\Delta r R_0^2(30N-10)+10R_0^3\right)$

When $f(\mathbf{r})$ and $g(\mathbf{r})$ are radially symmetric, we can write this as

$$(f * g)(\mathbf{r}) = (f * g)(r) = \int_V \mathrm{d}^3 r' f(|\mathbf{r}-\mathbf{r}'|) g(r'). \tag{E.10}$$

One would be tempted to evaluate this integral by expressing $\mathbf{r}'$ in spherical coordinates. However, this leads to a rather nasty expression in the argument of $f(r)$, which is hard to evaluate numerically, since $f(r)$ is then only known at fixed points r_i.

Instead, it helps to think of the geometric situation. For each fixed vector $\mathbf{r}$, the convolution is the integral of the product of two functions over three-dimensional space, where in our case each of the functions is radially symmetric around a different point. For $\mathbf{r} = 0$, we can choose spherical coordinates and obtain

$$(f * g)(0) = 4\pi \int_0^R \mathrm{d}^3 r\, r^2 f(r) g(r), \tag{E.11}$$

where R is some cutoff determined in practise by the available range of g and f. This integral can be evaluated numerically using the method shown above. For $\mathbf{r} \neq 0$, due to the symmetry of the problem, we can choose to place $g(r)$ such that it is radially symmetric around the origin ($\mathbf{p}_1 \equiv (0,0,0)$), while $f(r)$ is placed such that it is symmetric around the point $\mathbf{p}_2 \equiv (0,0,|\mathbf{r}|)$, without changing the value of the integral.

If we now draw a sphere of radius r_1 around $\mathbf{p}_1$, and another sphere of radius r_2 around $\mathbf{p}_2$, these spheres intersect either not at all, or in a point, or on a ring. We can use

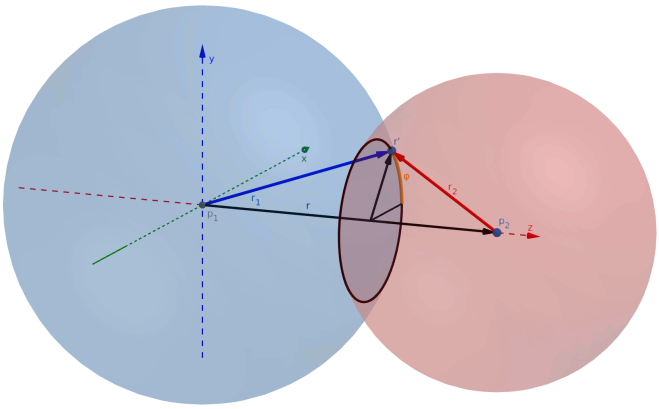

Figure E.1.: Coordinate system for calculating the convolution of two radially symmetric functions. For a fixed vector $\mathbf{r}$, the coordinates r_1, r_2 and φ can be used to reach any point in $\mathbb{R}^3$.

an angle φ to specify the location on said ring and thus specify an arbitrary point in three-dimensional space (see figure E.1 for an illustration). Some elementary geometry tells us that the cartesian coordinates x, y, and z are parametrised by r_1, r_2 and φ as follows:

$$a = \frac{1}{2}\sqrt{2({r_1}^2 + {r_2}^2) - r^2 - \frac{({r_1}^2 - {r_2}^2)^2}{r^2}} \tag{E.12}$$

$$\begin{pmatrix} x \\ y \\ z \end{pmatrix} = \begin{pmatrix} a\cos\varphi \\ a\sin\varphi \\ \dfrac{{r_1}^2 - {r_2}^2 + r^2}{2r} \end{pmatrix}. \tag{E.13}$$

This is admittedly not the prettiest transformation, but its Jacobian determinant is surprisingly simple:

$$\left|\frac{\partial(x,y,z)}{\partial(r_1,r_2,\varphi)}\right| = \frac{r_1 r_2}{r}. \tag{E.14}$$

We can thus rewrite the convolution integral for all $r \neq 0$ as

$$(f * g)(r) = \int_0^{2\pi} \mathrm{d}\varphi \int_0^R \mathrm{d}r_1 \int_{|r_1 - r|}^{r_1 + r} \mathrm{d}r_2 \frac{r_1 r_2}{r} g(r_1) f(r_2) = \frac{2\pi}{r} \int_0^R \mathrm{d}r_1 \int_{|r_1 - r|}^{r_1 + r} \mathrm{d}r_2 r_1 r_2 g(r_1) f(r_2), \tag{E.15}$$

where the limits for the integration in r_2 can be easily seen when considering for which

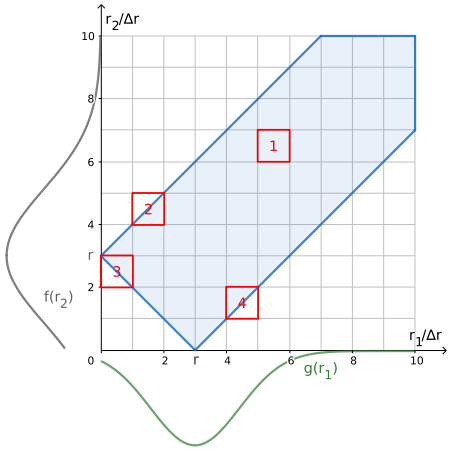

Figure E.2.: The integration area for $r = 3$, $r_1 \in [0, 10]$, $r_2 \in [|r_1 - r|, \min(r_1 + r, 10)]$. There are four distinct integration areas which can occur if f and g are only know in steps of size Δr. These situations are marked with red squares.

values of r, r_1 and r_2 there is overlap or contact between the two spheres shown in figure E.1.

Now remains the task of discretising this integral. We assume to have representations of the functions f and g which consist of equally spaced values f_i and g_j, as shown above in equation (E.5). Figure E.2 shows the integration area for one fixed r. It is a diagonal rectangle of width r, which is truncated at the radius R, beyond which we assume to have no information about f or g. This area can be separated into squares with side length Δr, where each square lies either completely within the integration area, or half within it. There are four distinct options:

1. the square is completely within the integration area,
2. the square's bottom right half lies within the integration area,
3. the square's top right half lies within the integration area,
4. the square's top left half lies within the integration area.

The value of the integral is the sum of the integrals over each of the relevant squares. The value of the integral within the square whose lower left corner is located at coordinates $i\Delta r, j\Delta r$ depends on the products $f_j g_i$, $f_{j+1} g_i$, $f_j g_{i+1}$, and $f_{j+1} g_{i+1}$. The weights for each of these four products can be pre-computed and the sum that makes

up the integral can be represented as a matrix product

$$\mathbf{f} \cdot \mathbf{C}_k \cdot \mathbf{g}, \tag{E.16}$$

where the entries of the vectors $\mathbf{f}$ and $\mathbf{g}$ are the values f_j and g_i, respectively. The convolution matrix $\mathbf{C}_k$ depends on the radius $r = r_k = k\Delta r$.

The expressions for the coefficients of $\mathbf{C}_k$ are somewhat unwieldy, therefore instead of reproducing them here, we have published a reference implementation at [114].

F. DDFT in spherical coordinates

F.1. Numerical violation of particle conservation

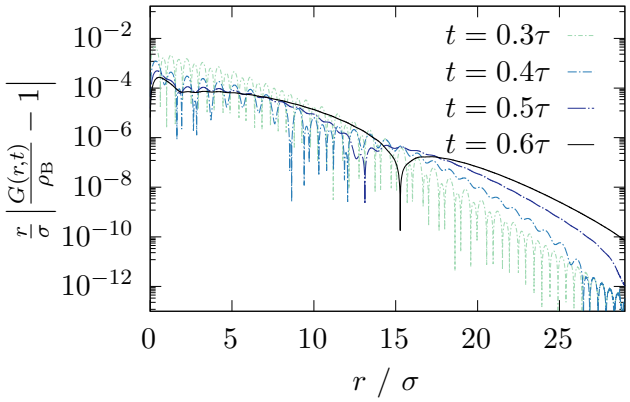

Figure F.1.: Shifted van Hove function $\frac{r}{\sigma}\left|\frac{G(r,t)}{\rho_B}-1\right|$ from DDFT with the quenched functional at large distances r. Data is shown for different times t (as indicated) which are representative for the different stages of the time evolution of the van Hove function at long range.

In our DDFT calculations, the shell structure of the van Hove function disappeared after $t \gtrsim 0.5\tau$, leaving only a large-scale oscillation. Figure F.1 shows this phenomenon in more detail. We see in this figure that for $t = 0.3\tau$, the amplitude of the minima of $G(\mathbf{r}, t)$ shrinks compared to the amplitude of the maxima in the region $r \lesssim 10\sigma$. In the region $r \gtrsim 10\sigma$, the amplitude of the maxima decreases compared to that of the minima. For $t = 0.4\tau$, the zeros of $G(\mathbf{r}, t) - 1$ have disappeared between $r \approx 2\sigma$ and $r \approx 8\sigma$ as well as between $r \approx 13\sigma$ and $r \approx 26\sigma$. At $t = 0.5\tau$, only a single zero at $r \approx 13\sigma$ remains, which moves outwards from the origin, reaching $r \approx 15\sigma$ by $t = 0.6\tau$. There is no more oscillatory behaviour discernible at this stage of the time evolution. Therefore it seems to be the case that the density is systematically increasing in the region close to the origin, and decreasing in the outer region.

We consider this effect to be numerical, rather than physical, in nature. The first point of evidence for this is that we do not observe the same effect in BD simulation. However, this could be due to the somewhat limited system size in our simulations. An analysis of our numerical integration method, presented in the following, reveals a violation of particle conservation which could explain the deviations in density.

We consider the DDFT equation of motion (1.38) for the total density profile in the system. In our implementation, we calculate the change in the density profile from two contributions as follows:

$$\frac{\partial}{\partial t}\rho(\mathbf{r},t) = D\Delta\rho(\mathbf{r},t) - \nabla\cdot\mathbf{J}_{\text{exc}}(\mathbf{r},t), \tag{F.1}$$

where the adiabatic excess current $\mathbf{J}_{\text{exc}}(\mathbf{r},t)$ is defined as

$$\mathbf{J}_{\text{exc}}(\mathbf{r},t) = -\frac{\rho(\mathbf{r},t)}{\gamma}\nabla\frac{\delta F_{\text{exc}}[\rho]}{\delta\rho(\mathbf{r},t)}. \tag{F.2}$$

For a system in spherical coordinates, with all quantities assumed to be radially symmetric, we can write $\rho(\mathbf{r},t) = \rho(r,t)$ and $\mathbf{J}_{\text{exc}}(\mathbf{r},t) = J_{\text{exc}}(r,t)\hat{\mathbf{e}}_{\text{r}}$, where $\hat{\mathbf{e}}_{\text{r}}$ is the unit vector in radial direction). (F.1) then takes the form

$$\dot{\rho}(\mathbf{r},t) = D\frac{1}{r^2}\frac{\partial}{\partial r}\left(r^2\frac{\partial}{\partial r}\rho(r,t)\right) - \frac{1}{r^2}\frac{\partial}{\partial r}\left(r^2 J_{\text{exc}}(r,t)\right) \tag{F.3}$$

$$= D\left(\frac{\partial^2}{\partial r^2} + \frac{2}{r}\frac{\partial}{\partial r}\right)\rho(r,t) - \left(\frac{2}{r} + \frac{\partial}{\partial r}\right)J_{\text{exc}}(r,t). \tag{F.4}$$

In a numerical calculation, both $\rho(r,t)$ and $J_{\text{exc}}(r,t)$ are represented as sequences of samples $\rho_{i,k}$ and $J_{i,k}$ respectively, where the corresponding continuous function is approximated e.g. with a linear interpolation

$$\rho(r,t_k) \approx \sum_{i=0}^{\infty}\rho_{i,k}\,b(r - k\Delta r), \tag{F.5}$$

where Δr is a step size in space, $t_k \equiv k\Delta t$ is a point in time out of a sequence of time steps of duration Δt, and $b(r)$ is a triangle function, given by

$$b(r) = \begin{cases} 1 + \frac{r}{\Delta r} & \text{for } -\Delta r \le r \le 0 \\ 1 - \frac{r}{\Delta r} & \text{for } 0 < r \le \Delta r \\ 0 & \text{elsewhere.} \end{cases} \tag{F.6}$$

The total number of particles in the region $r < r_I$ at time t_k is then

$$N(t_k) = 4\pi \int_0^{r_I} \mathrm{d}r\, \rho(r, t_k) \approx \sum_{i=0}^{I} w_i \rho_{i,k} \,, \tag{F.7}$$

where w_i is a set of weights with

$$w_i = 4\pi \Delta r^3 \begin{cases} \frac{1}{12} & \text{for } i = 0 \\ \frac{1}{6}\left(6i^2 + 1\right) & \text{for } 0 < i < I \\ \frac{1}{12}\left(6I^2 - 4I + 1\right) & \text{for } i = I. \end{cases} \tag{F.8}$$

The derivatives in (F.4) can be approximated using well-known finite difference formulae, where for the time derivative of $\rho(r,t)$ we choose a forward difference

$$\frac{\partial}{\partial t}\rho(r_i, t_k) \approx \frac{\rho_{i,k+1} - \rho_{i,k}}{\Delta t}, \tag{F.9}$$

where $r_i \equiv i\Delta r$, for the first spatial derivative of $\rho(r,t)$ and of $J(r,t)$ we choose a central difference

$$\frac{\partial}{\partial r}J(r_i, t_k) \approx \frac{J_{i+1,k} - J_{i-1,k}}{2\Delta r}, \tag{F.10}$$

and for the second spatial derivative of $\rho(r,t)$, we choose the central difference

$$\frac{\partial^2}{\partial r^2}\rho(r_i, t_k) \approx \frac{\rho_{i+1,k} - 2\rho_{i,k} + \rho_{i-1,k}}{\Delta r^2}. \tag{F.11}$$

We disregard here the origin and the outer edge of the box as these special cases do not impact the discussion in this section. Taking these together, we obtain the iterative scheme

$$\rho_{i,k+1} = \rho_{i,k} - \Delta t \left[\frac{2}{r_i} J_{i,k} + \frac{J_{i+1,k} - J_{i-1,k}}{2\Delta r} + D\left(\frac{\rho_{i+1,k} - 2\rho_{i,k} + \rho_{i-1,k}}{\Delta r^2} + \frac{\rho_{i+1,k} - \rho_{i-1,k}}{i\Delta r^2} \right) \right]. \tag{F.12}$$

We have now unwittingly created a source (or drain) for particles. We can convince ourselves of that by considering the total change in particle number resulting from this iterative step, given by inserting (F.12) into (F.7) to calculate $N(t_{k+1})$ and subtracting

$N(t_k)$. The resulting sum can be reordered by the spatial indices of $J_{i,k}$ and $\rho_{i,k}$. We obtain for the particle difference due to the current sample $J_{i,k}$

$$\Delta N_{J,i} = J_{i,k}\left(-\frac{2\Delta t}{r_i}w_i + \frac{\Delta t}{2\Delta r}w_{i+1} - \frac{\Delta t}{2\Delta r}w_{i-1}\right), \tag{F.13}$$

and due to the density sample $\rho_{i,k}$ we get

$$\Delta N_{\rho,i} = -\frac{\Delta t}{\Delta r^2}Di\rho_i\left(\frac{w_{i+1}}{i+1} - 2\frac{w_i}{i} + \frac{w_{i-1}}{i-1}\right) \tag{F.14}$$

Together, the change in particle number corresponding to each point r_i is

$$\begin{aligned}
\Delta N_i &= \Delta N_{J,i} + \Delta N_{\rho,i} && \text{(F.15)}\\
&= \frac{\Delta t}{\Delta r}\left[J_{i,k}\left(\frac{w_{i+1}-w_{i-1}}{2} - \frac{2w_i}{i}\right) - \rho_{i,k}\frac{D}{\Delta r}i\left(\frac{w_{i+1}}{i+1} - 2\frac{w_i}{i} + \frac{w_{i-1}}{i-1}\right)\right] && \text{(F.16)}\\
&= -\frac{4}{3}\pi\Delta r^2\Delta t\left[\frac{J_{i,k}}{i} + \frac{\rho_{i,k}D}{\Delta r(i^2-1)}\right]. && \text{(F.17)}
\end{aligned}$$

In Cartesian coordinates, this systematic drift in particle number does not occur, as there are no asymmetries in the spatial derivatives, and all points $\rho_{i,k}$ contribute equally to the integral (F.7). Hence, the drift of the particle number is a defect of this numerical method, and we present an improvement in the following.

F.2. A norm-preserving integration scheme

Thomas Schindler has developed a norm-preserving integration scheme, which we present in the appendix of [3]. Instead of writing the numerical iteration scheme in terms of $\rho_{i,k}$ and $J_{i,k}$, we discretise the quantities

$$R(\mathbf{r},t) \equiv 4\pi r^2\rho(\mathbf{r},t) \text{ and} \tag{F.18}$$

$$\mathbf{J}^{\mathrm{R}}(\mathbf{r},t) \equiv 4\pi r^2\mathbf{J}(\mathbf{r},t), \tag{F.19}$$

which include a weighting by the surface of the sphere with radius r. This transformation equalises the contribution of each point $R_{i,k} \equiv R(r_i,t_k)$ to the volume integral of the density profile. Therefore, the drift of the particle number is significantly reduced, at the price of some more numerical noise at large radii due to division by large numbers.